ANUL XLIV **1999**

S T U D I A
UNIVERSITATIS BABEŞ-BOLYAI

PHYSICA
1

Editorial Office: 3400 CLUJ-NAPOCA, Gh. Bilaşcu no. 4 ♦ Phone:405300; ext.: 167

C O N T E N T S

SOLID STATE PHYSICS

SPECTROSCOPY

LIQUID PHYSICS

TECHNICAL PHYSICS

THEORETICAL PHYSICS

STUDIA UNIVERSITATIS BABEŞ-BOLYAI, PHYSICA, XLIV, 1, 1999

THE INFLUENCE OF THE PARTIALLY SUBSTITUTIONS OF CU BY AS AND O BY F, CL AND S IN Y-BA-CU-O COMPOUNDS

I. ARDELEAN*, V. POP, I. STANCA, I. GR. DEAC, GH. BORODI***, A. TISAN**

ABSTRACT. The influence of partial substitution of Cu by As in the $YBa_2(Cu_{1-x}As_x)_3O_{7-\delta}$ superconducting compounds ($0 \leq x \leq 0.1$) and partial substitution of O by F, Cl and S in the Y-123-(F), Y-123-(Cl) and respectively Y-123-(S) were studied by using X-ray diffraction, electrical resistivity, d. c. and a. c. susceptibility measurements.

The samples, $YBa_2(Cu_{1-x}As_x)_3O_{7-\delta}$ and Y-123-(F), Y-123-(Cl) and Y-123-(S) were prepared by a standard ceramic method.

The structure has been analyzed by X-ray diffraction. Arsenic doped samples have orthorhombic-type structure. No unreacted phases were observed. Partial substitution of copper by arsenic ions does not suppress the transition from normal to superconducting states for this range of doping. The T_C determined from d. c. electrical conductivity and d. c. and a. c magnetic susceptibility measurements decrease with As concentration, but it still has large value of 85 K, when x=0.1.

The reciprocal susceptibility values, χ^{-1}, of the Y-123-(F), Y-123-(Cl) and Y-123-(S) samples present a linear dependence in a large range of temperature, suggesting the presence of Cu^{2+} ions. The ratio Cu^{2+}/Cu^{+} was evaluated.

Introduction

Since the discovery of high-T_c superconductor $YBa_2Cu_3O_y$ [1] the effect of the substitution of copper by other elements on physical properties has been studied by many authors in order to investigate the origin of the superconductivity. The reasons for the introduction of additional components to the standard superconducting composition arise from the possibility of solving different physical and technological problems,

* Faculty of Physics, Babeş-Bolyai University, 3400, Cluj-Napoca
** Department of Physics, University of Oradea, 3700, Oradea
*** Institute of Molecular and Isotopic Technologies, 3400, Cluj-Napoca

bearing on the mechanism of high-temperature superconductivity, electric and magnetic parameters, technological conditions for synthesis, better sintering, densification and orientation of the crystals, mechanical strength and chemical stability.

Generally, upon any substitution for Cu in $YBa_2(Cu_{1-x}M_x)_3O_y$, a decrease in T_c is observed. Phenomenological, the substitute of copper may be divided into three groups according to their effect on T_c:

i). Substitute causing an initially rapid decrease of T_c as Zn and Mg [2÷5].

ii). Substitute causing a moderate decrease of T_c,. Fe and Co exemplify this case [6].

iii). Substitute with an almost linear decrease of T_c, Ni for example [7, 8].

A possible way to modify the HTS properties is the anionic substitution. It was reported that modification involving fluorination of a superconducting oxide $YBa_2(Cu_{1-x}M_x)_3O_y$, gave new materials having a noticeably high temperature of 155 [9], 148. 5 [10], and 240 K [11]. Many groups have been attempting to reproduce the superconducting phase with T_c > 100 K by different techniques, but no group has found evidence of a higher transition temperature than 90K.

As an on going work in analyzing the influence of Cu substitution by As [12], in the present work we analyze the effect of partial substitution of copper by arsenic in the $YBa_2(Cu_{1-x}As_x)_3O_{7-\delta}$ compounds ($0 \leq x \leq 0.1$) and of oxygen partial substitutions by F, Cl and S in the Y-123-(F), Y-123-(Cl) and Y-123-(S) samples on the structural, electrical and magnetic properties.

Experimental Technique

The $YBa_2(Cu_{1-x}As_x)_3O_{7-\delta}$ samples, with $0 \leq x \leq 0.1$, were obtained by a standard ceramic method by solid state reaction, under same conditions. Fine and high-purity powder reagents of Y_2O_3, $BaCO_3$, CuO and As_2O_3 in appropriate proportions were thoroughly mixed. The well mixed powder materials were heated for 10 h in air and 10 h in oxygen in alumina crucible at 940°C. The calcinated powder was reground, cold-pressed into pellets under pressure of 3.5 t/cm^2 which were sintered in air for 10 h and in oxygen for 14 h. at 950°C. To obtain highly oxygenated samples, these pellets were annealed under oxygen flow at 400°C for 10 h followed by slow cooling (3°C/min) until room temperature was reached.

The samples with F, Cl and S were obtained starting from: Y_2O_3, BaF_2, CuO for Y-123-(F); Y_2O_3, $BaCl_2$, CuO for Y-123-(Cl) and Y_2O_3, $BaCO_3$, $CuSO_4$ for Y-123-(S) in the required proportions. The heat treatments were made in the same conditions as for $YBa_2(Cu_{1-x}As_x)_3O_{7-\delta}$ compounds.

X-ray diffraction patterns were obtained by powder diffraction using Cr-Kα radiation.

The temperature dependence of the electrical resistance R(T) was determined by the usual d. c. four- point probe technique using electrical contacts, obtained of silver paste.

The d. c. and a. c. magnetic susceptibility measurements were performed with a Weiss equipment with $10^{-8}cm^{-1}g^{-1}$ sensitivity between 77 and 300 K in a magnetic field of 0. 9 T and respectively with Maglab 2000 system (Oxford Instruments).

Results and discussions

Figure 1. shows the X-ray diffraction patterns and table 1 contains the values of the lattice parameters of the samples $YBa_2(Cu_{1-x}As_x)_3O_{7-\delta}$ with x=0, 0. 05 and 0. 1 at room temperature. The orthorhombic splitting indicated by (020) and (200) peaks are quit similar in both pure and As doped samples, showing an orthorhombique structure in $YBa_2(Cu_{1-x}As_x)_3O_{7-\delta}$ samples in the whole composition range. All of the samples are single phase. There are not noticeable structural changes in a, b and c parameters. X-ray diffraction studies show that the partial oxygen substitution in Y-123 by F, Cl and S does not modify its structure.

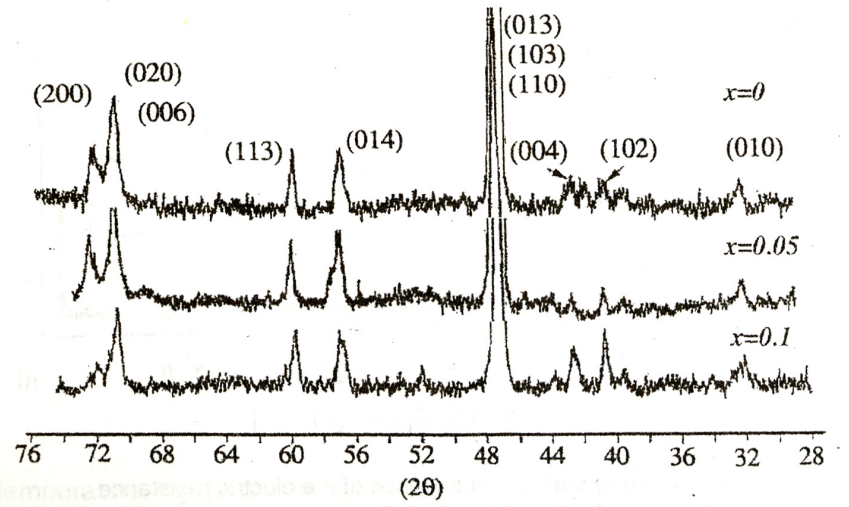

Fig. 1. X-ray diffraction patterns of some $YBa_2(Cu_{1-x}As_x)_3O_{7-\delta}$ compounds

Table 1

The values of the lattice parameters for $YBa_2(Cu_{1-x}As_x)_3O_{7-\delta}$ compounds with x=0, 0. 05 and 0. 1

x	a [A]	b [A]	c [A]	(b-a)/(a+b)
0	3. 826	3. 879	11. 638	0. 00687
0. 05	3. 825	3. 881	11. 640	0. 00726
0. 1	3. 825	3. 882	11. 645	0. 00739

Figure 2 shows the temperature dependence of the electric resistance for various x in the temperature range from 77 to 300 K. In the normal state, $T > T_c$, the electric resistance of all the samples gradually decrease with decreasing temperature.

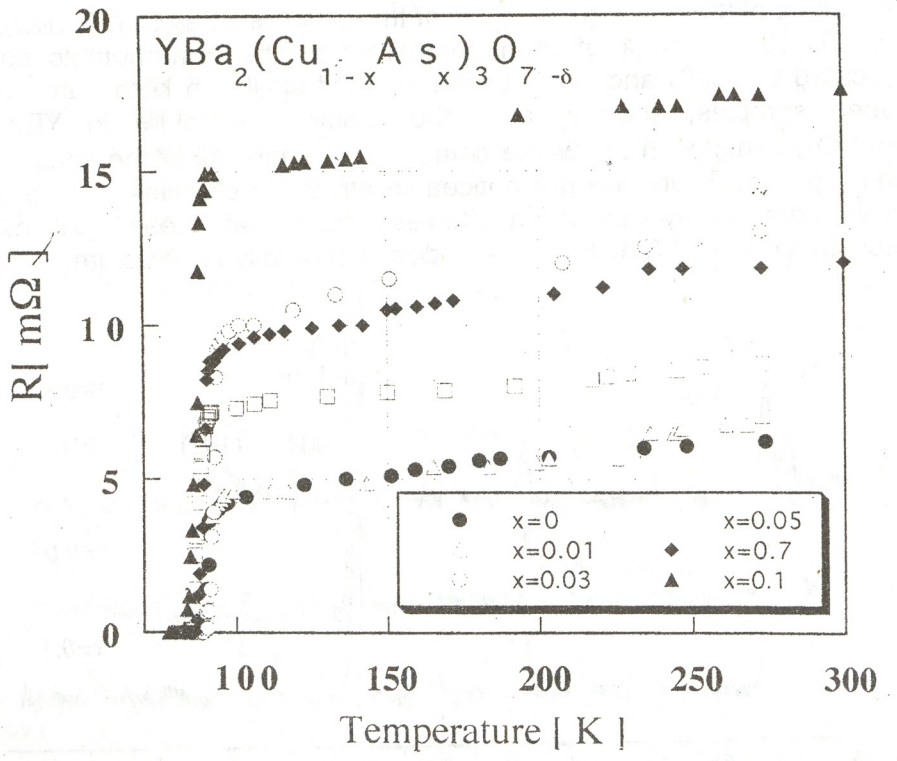

Fig. 2. Temperature dependence of the electric resistance for $YBa_2(Cu_{1-x}As_x)_3O_{7-\delta}$ compounds

The temperature dependence of the electric resistance in the normal state is nearly linear, indicating a good oxygenation of the samples (δ was estimated to be 0. 03 for the undoped samples). Figure 3 display the variation of T_c as function of the As concentration. T_c is defined as the midpoint of the superconducting transition (determined from 10 % and 90% of the extrapolated high temperature value) obtained from electric measurements. Our results clearly indicated that As influence on the superconducting properties of $YBa_2(Cu_{1-x}As_x)_3O_{7-\delta}$. The T_c decreases slowly with increasing the dopant content. At 10 at. % of As, T_c still has a large value of 84. 3 K.

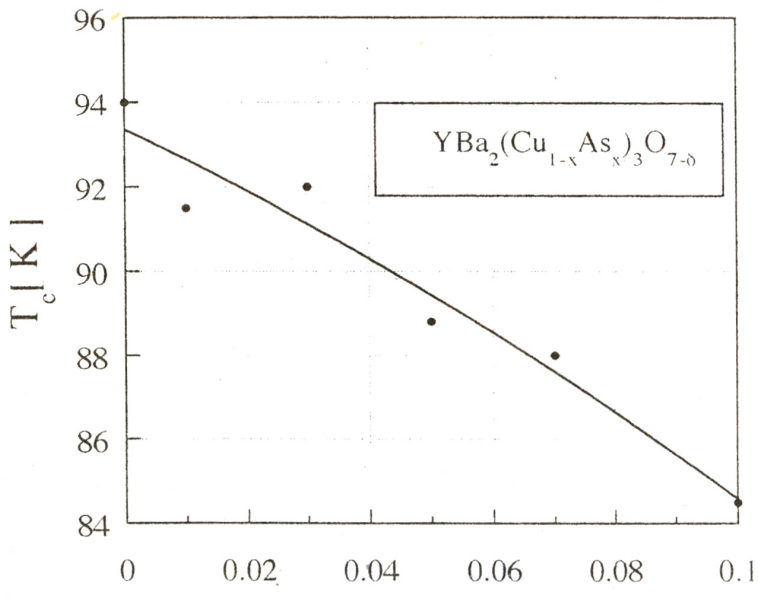

Fig. 3. The composition dependence of T_c values in $YBa_2(Cu_{1-x}As_x)_3O_{7-\delta}$ compounds

The Y-123-(F), Y-123-(Cl) and Y-123-(S) samples in the 77-300 K temperature range are insulators. It results that F, Cl or S, that partially replace the oxygen, occupies such sites within the lattice that lead to the suppression of the Y-123 genuine superconducting transition.

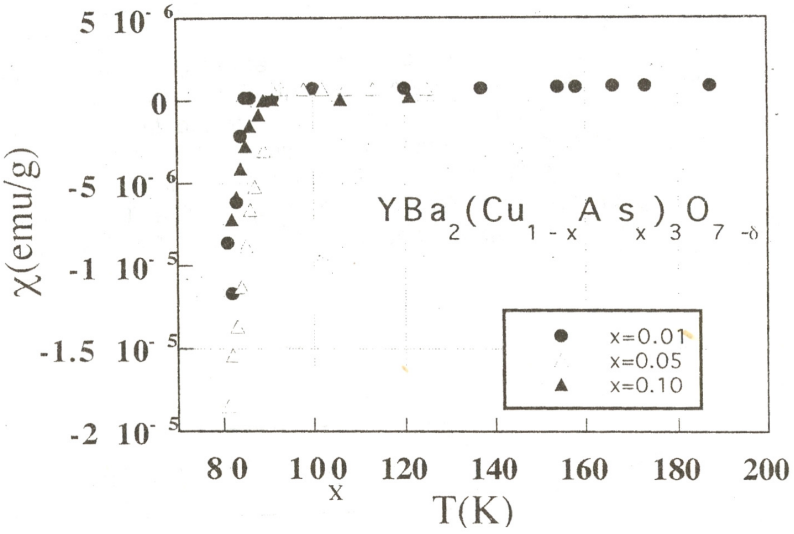

Fig. 4. Temperature dependence of the dc magnetic susceptibility of $YBa_2(Cu_{1-x}As_x)_3O_{7-\delta}$ compounds

The magnetic susceptibility of $YBa_2(Cu_{1-x}As_x)_3O_{7-\delta}$ was measured with dc and ac methods. Figure 4 shows the temperature dependence of the dc magnetic susceptibility of $YBa_2(Cu_{1-x}As_x)_3O_{7-\delta}$ samples for various x in the temperature range 77-300 K. For $YBa_2(Cu_{1-x}As_x)_3O_{7-\delta}$ samples the d. c. magnetic susceptibility show negative values due to the Meissner effect in the temperature range up to 77 K and highly increased with increasing of temperature in the transition temperature range.

From a. c. magnetic susceptibility data of $YBa_2(Cu_{1-x}As_x)_3O_{7-\delta}$ samples (figure 5) was identified the intragranular critical temperature (T_c), the intergranular critical temperature (T_1) and the width of the transition temperature (ΔT). The values of these temperature were obtained from χ' and χ'' behaviours and they are show in the table 2. The onset of negative values in χ' represent the diamagnetic effect of the samples and this condition correspond to intrinsic critical temperature (T_c). The χ'' values describes the loss mechanism and the intergranular critical temperature (T_1) at the moment when a. c. field penetrate through the intergranular space to center of the sample. T_1 temperature given by the values of the temperatures that corresponds to the maximum of the peak, which appear

in the curve of χ"(T). The width of the transition is given by temperature interval (ΔT) which correspond to width of the χ" peak at the half of its height.

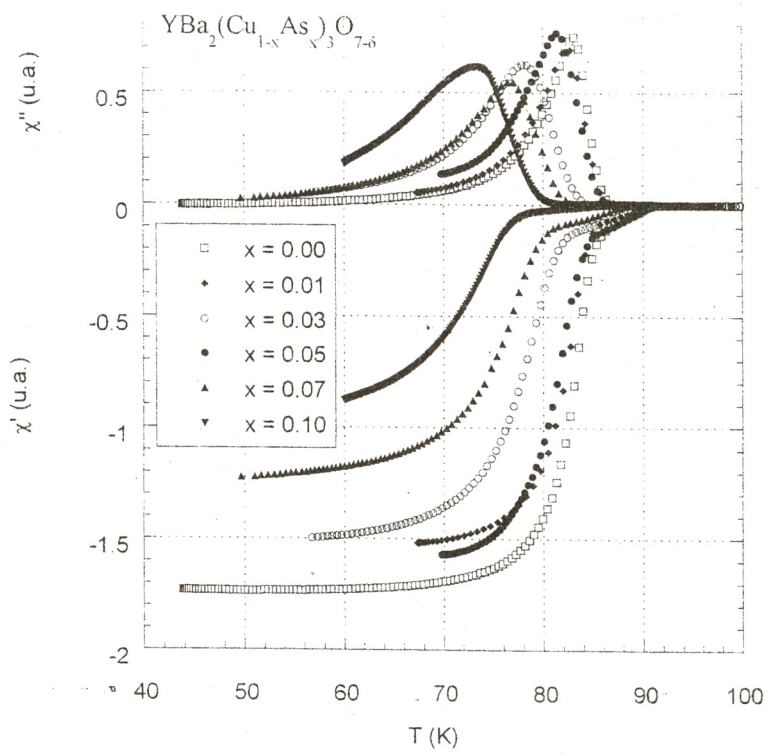

Fig. 5. Temperature dependence of the a. c. magnetic susceptibility of $YBa_2(Cu_{1-x}As_x)_3O_{7-\delta}$ samples.

Table 2

The values of intragranular critical temperature (T_c), intergranular critical temperature (T_1) and width of transition temperature (ΔT) for $YBa_2(Cu_{1-x}As_x)_3O_{7-\delta}$ compounds (0. 0≤x≤0. 1)

$YBa_2(Cu_{1-x}As_x)_3O_{7-\delta}$	x=0	x=0. 01	x=0. 03	x=0. 05	x=0. 07	x=0. 1
T_c	94	92	91. 8	89	88	84. 3
T_1	90	86	82	83	84	78
ΔT	5. 5	6. 25	6. 65	7. 5	8. 3	8. 7

For the samples doped with F, Cl and S there was observed a temperature dependence of the d. c. magnetic susceptibility, in contrast with the pure Y-123 sample which present an independent temperature paramagnetism in the normal state (T > 100 K) (figure 6). This behaviour indicates the presence of some atomic paramagnetic moments, which we suppose to be due to copper, which could be in the system with a valence, which is different of +1. The χ^{-1} values presented in figure 7 a and b shows a linear dependence in large ranges of temperature. From this data we calculated the effective magnetic moment (μ_{eff}) responsible for this behaviour. Supposing that the μ_{eff} values are given by Cu^{2+} we have calculated the atomic fraction of the Cu^{2+} in the system. This fraction is 49% in Y-123-(Cl), 25% in Y-123-(F) and 10% in Y-123-(S) samples.

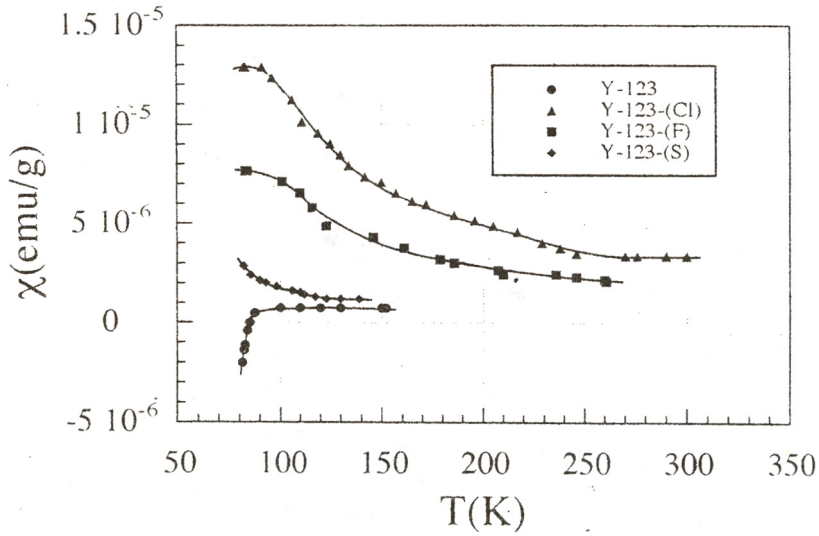

Fig. 6. Temperature dependence of the magnetic susceptibility of the pure Y-123 and Y-123-(F), Y-123-(S) and Y-123-(Cl) compounds

Conclusions

The high temperature superconducting compounds $YBa_2(Cu_{1-x}As_x)_3O_{7-\delta}$ were studied for x values between 0. 0 and 0. 1. In this composition range arsenic has a small effect on the superconductivity of $YBa_2Cu_3O_{7-\delta}$ when it substitute copper. There are no drastic structural changes in the lattice parameters and in the Meissner effect of the system with As doping. The T_c values decrease slowly with increasing the As content and T_c has a minimum value of 84. 3 K for x=0. 1.

The samples Y-123-(F), Y-123-(Cl) and Y-123-(S), in the temperature range 77-300 K are insulators.

The χ^{-1} values of the Y-123-(F), Y-123-(Cl) and Y-123-(S) compounds present a linear dependence in a large range of temperature, suggesting the presence of Cu^{2+} ions in this samples. Future studies were necessaries to elucidate the physical properties of these compounds.

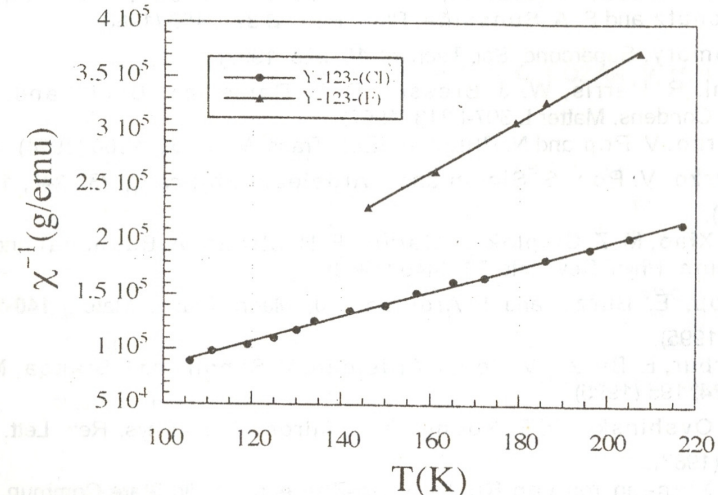

Fig. 7. a. Temperature dependence of the χ^{-1} values of Y-123-(F) and Y-(123)-(Cl) compounds

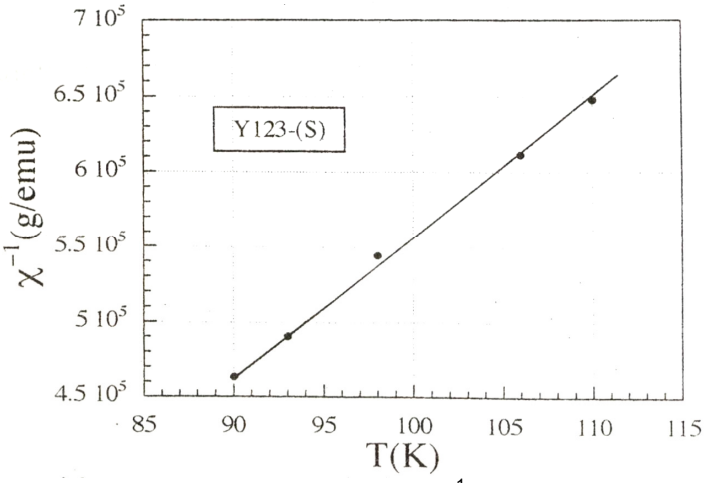

Fig. 7. b Temperature dependence of the χ^{-1} values of Y-123-(S) compound

REFERENCES

1. J. M. Tarascon, P. Barboux, P. F. Miceli, L. H. Greene, G. W. Hull, M. Eibschutz and S. A. Sunshine, Phys. Rev., **B 37**, 7458 (1988).
2. F. Gomory, Supercond. Sci. Technol. **10**, 523 (1997).
3. F. Shi, R. Harris, W. J. Bresser, D. McDaniel and Boolchand, J. Phys. Condens. Matter L 307-L313 (1997).
4. E. Burzo, V. Pop and N. Plugaru, IEEE Trans. Magn. **30**, 1160 (1994).
5. E. Burzo, V. Pop, S. Simon and I. Ardelean, Physica C, **235-240,** 1589 (1994).
6. Gang Xiao, M. Z. Cieplak, A. Garvin, F. H. Streitz, A. Bakhshai and C. L. Chien, Phys. Rev. Lett. **50**, 1446 (1988).
7. V. Pop, E. Burzo and I. Ardelean, J. Magn. Magn. Mater. **140-144,** 1307(1995).
8. I. Barbur, E. Burzo, V. Pop, I. Ardelean, V. Simon and I. Stanca, Mat. Lett. **24**, 195 (1995).
9. S. R. Ovshinsky, R. T. Young, D. D. Allred et all., Phys. Rev. Lett. **58,** 2579 (1987).
10. Meng Xian-ren, ren Yan-Ru, Lin Ming-Zhu et all., Solid State Commun. **64,** 325 (1987).
11. R. N. Bragava, S. P. Herko, W. N. Osborne, Phys. Rev. Lett. **59,** 1468 (1987).
12. I. Ardelean, I. Gr. Deac, V. Pop, I. Stanca, A. Tisan, Gh. Borodi, Suplement of the BPL, vo lume **5,** 631-634 (1997).

STUDIA UNIVERSITATIS BABEŞ-BOLYAI, PHYSICA, XLIV, 1, 1999

MAGNETIC PROPERTIES OF GLASSES FROM V_2O_5-P_2O_5-PbO SYSTEM

I. ARDELEAN, GH. ILONCA, V. SIMON, O. COZAR, V. MIH*

ABSTRACT. The temperature dependence of the magnetic susceptibility of $xV_2O_5\cdot(100-x)$. $[2P_2O_5.PbO]$ glasses with $0 < x \leq 50$ mol % have been investigated. The valence states and the distribution of vanadium ions in this glass matrix depend on the V_2O_5 concentration. The proportion of the V^{4+} ions which are favored to exist in this glass matrix, is around 27 % in all concentration range studied. For $x > 3$ mol % the V^{4+} ions participate to the superexchange interactions which can be of mictomagnetic-type.

Introduction

The V^{4+} ions incorporated in glasses as a spectroscopic probe have been studied by several reserchers [1-9] in order to characterize the glass structure. Because of their semiconducting behaviour, the electrical properties of these glasses were also investigated [10-14].

The magnetic properties of oxide glasses with V^{4+} ions were less studied. In earlier works we reported the magnetic properties of $xV_2O_5\cdot(100-x)$. $[2B_2O_3.PbO]$ [8] and $xV_2O_5\cdot(100.x)$. $[2B_2O_3.Li_2O]$ [15] glasses with $0 \leq x \leq 55$ mol % and $0 \leq x \leq 50$ mol %, respectively.

In the present work, the interactions between vanadium ions and their influence on the magnetic properties of $xV_2O_5\cdot(100.x)$. $[2P_2O_5.PbO]$ glasses in function of vanadium ions concentration are studied using magnetic susceptibility measurements.

* Faculty of Physics, Babeş-Bolyai University, 3400 Cluj-Napoca, Romania

Experimental

Glasses of the system $xV_2O_5 \cdot (100-x)$. $[2P_2O_5.PbO]$ have been prepared by using reagent grade purity V_2O_5, PbO and $(NH_4)2HPO_4$. The mixtures, in suitable proportions corresponding to the designed concentration of V_2O_5, were mechanically homogenized and melted in sintered corundum crucibles in an electrical furnace at 1250°C. The molten material was kept at this temperature for 5 minutes, then quenched at room temperature by pouring onto a stainless steel plate. Typical glasses were obtained up to 50 mol % V_2O_5. The samples were analyzed by means of X-ray diffraction and did not show any crystalline phase.

The magnetic data were obtained using a Faraday type balance in the temperature range 80 – 300 K. The magnetic susceptibility values were determined taking into account the correction of the measured data due to the diamagnetism of the glass matrix and the V_2O_5 core electrons.

Results and discussion

The temperature dependence of the reciprocal magnetic susceptibility of some glasses from the investigated system are presented in Fig. 1. For the samples with $x \leq 3$ mol % these dependences show a Curie-type behaviour. The result suggest that in this concentration range the vanadium ions are predominantly isolated in the glass matrix but they may be involved in dipole-dipole type interactions according to the EPR data [16]. For $x > 3$ mol % the reciprocal susceptibilities indicate a Curie-Weiss behaviour with negative paramagnetic Curie temperature, θ_p, that denotes the vanadium ions are predominantly antiferromagnetically coupled. The magnetic order takes place only at short range, suggesting the presence of a mictomagnetic type behaviour [17]. Therefore, in the $2P_2O_5 \cdot PbO$ glass matrix the vanadium ions behave magnetically different than in lithium [15] and lead [8] borate oxide glasses. In the $xV_2O_5 \cdot (100-x)$. $[2B_2O_3.Li_2O]$ and $xV_2O_5 \cdot (100.x)$. $[2B_2O_3.PbO]$ glasses the vanadium ions are isolated in all concentration range studied ($x_{max.}$ = 50 mol % and 55 mol %, respectively). .

The absolute magnitude of θ_p values increases for $x > 3$ mol % V_2O_5 (Fig. 2). This fact indicates that the exchange interactions increase with the concentration of the vanadium ions. The nonlinear dependence of the θ_p values on V_2O_5 content indicate that the number of vanadium ions implicated in these interactions is not proportional with V_2O_5 concentration.

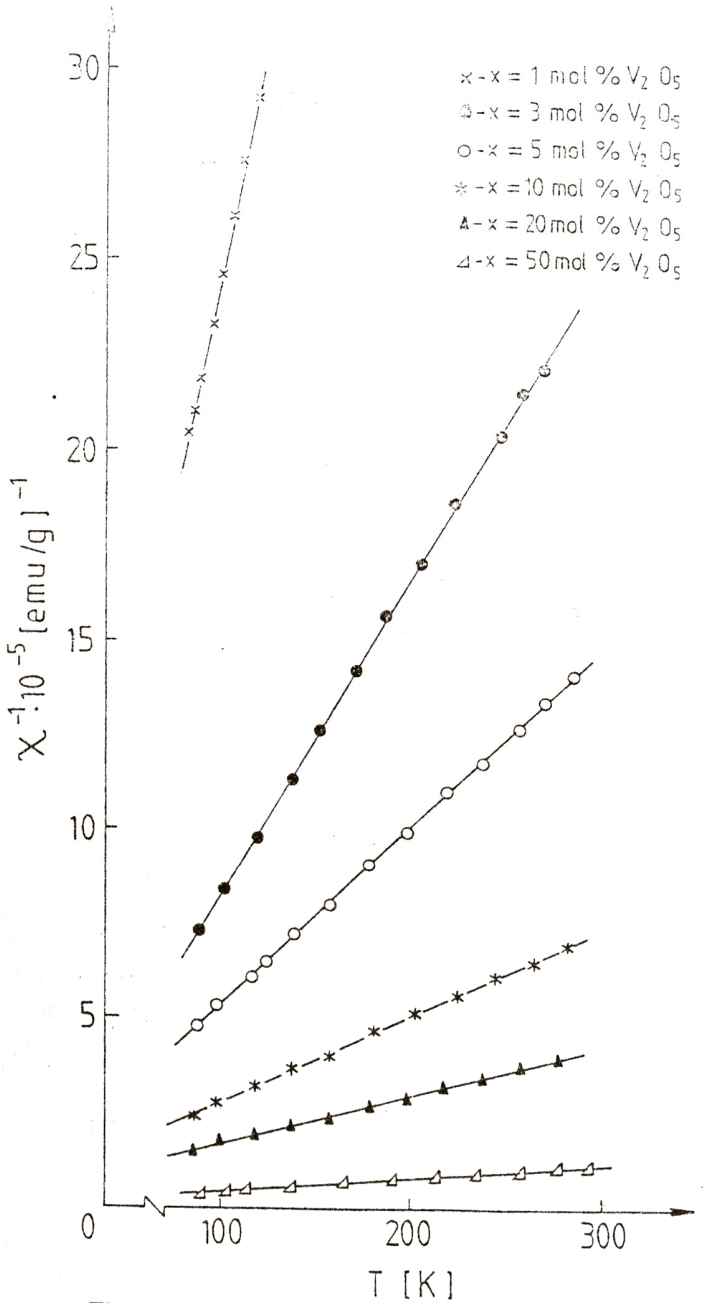

Fig. 1. The temperature dependence of the reciprocal magnetic susceptibility of V_2O_5-P_2O_5-PbO glasses.

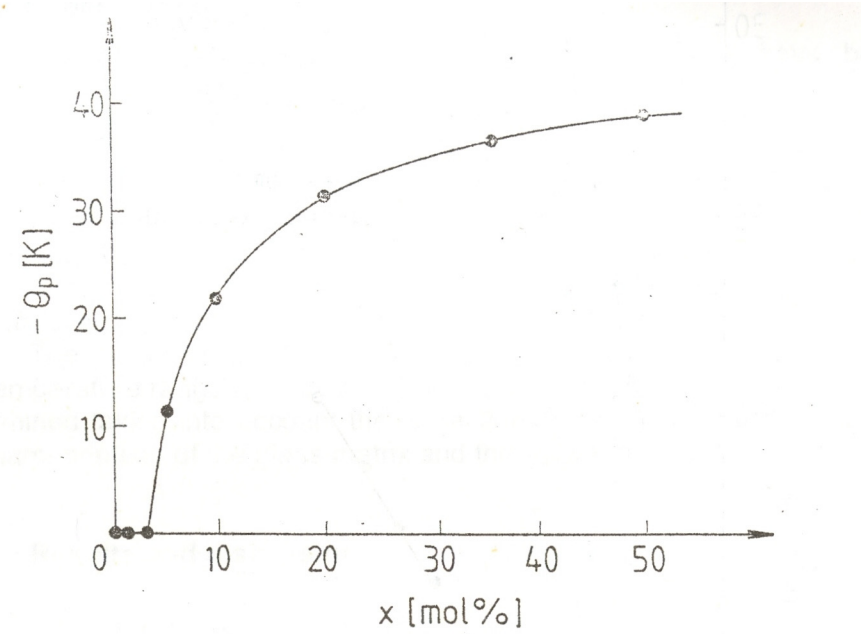

Fig. 2.. The composition dependence of the paramagnetic Curie temperature.

The composition dependence of the molar Curie constant is presented in Fig. 3. The experimental C_M values are lower than the expected ones, assuming that all vanadium ions are in V^{4+} valence state. In this way we suppose both V^{4+} and V^{5+} ions to be present. The occurence of V^{4+} ions was evidenced in all investigated samples by EPR studies [16]. In this case, considering that the V^{5+} ions are diamagnetic and having in view that the atomic magnetic moment of V^{4+} ions is $\mu_{V^{4+}} = 1.73\ \mu_B$, which was generally observed in paramagnetic salts [18], we can estimate in a first approximation [8] the molar fraction of V^{4+} ions, y, using the relation:

$$y = 2.827^2 C_M / 2\mu^2_{V^{4+}} .$$

The obtained results are presented in Table 1. One can observe from these data that in the investigated glass system the molar fraction of V^{4+} ions increases with the V_2O_5 content. These datare in agreement with those obtained for the experimental dependence of C_M = f(x) (Fig. 3). It results that only a small fraction of vanadium ions are in V^{4+} valence states.

Table 1. The molar Curie constant, molar fraction of V4+ ions and y/x ratio for V_2O_5-P_2O_5-PbO glasses.

x [mol % V_2O_5]	C_M [emu/mol]	y [mol % $V_2^{4+}O_5$]	y/x
1	0. 00204	0. 3	0. 27
3	0. 00603	0. 9	0. 28
5	0. 0103	1. 4	0. 28
10	0. 0206	2. 8	0. 28
20	0. 0380	5. 1	0. 29
50	0. 0984	13. 1	0. 26

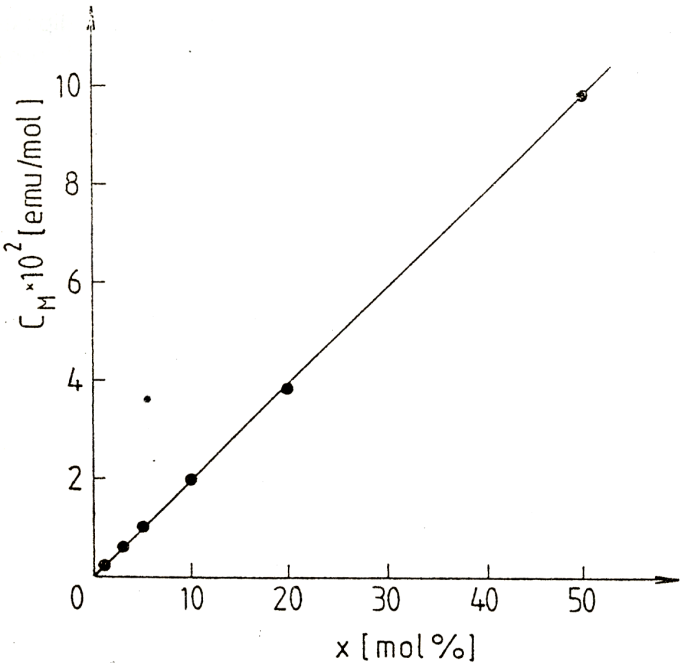

Fig. 3. The composition dependence of the molar Curie constant.

We also estimated the $N_{V^{4+}} / N_{V^{4+}+V^{5+}} = y / x$ ratios for the investigated glasses. The values of 0. 27±0. 1 (Table 1). indicate that only around 27 % of vanadium ions are favoured to exist in V^{4+} valence state in this glass matrix. In the case of $2B_2O_3$-PbO glass matrix [8] these rations are around 0. 12±1 (12 %). for all studied glasses, being smaller

comparatively with those corresponding to $2P_2O_5$.PbO matrix. The same ratio for $2B_2O_3$.Li_2O glass matrix [15] decreases from 0. 58 (58 %). for 3 mol % V_2O_5 to 0. 074 (7. 4 %). for 50 mol % V_2O_5. These data show that the nature of glass matrix former and modifier play an important rol in the distribution of vanadium ions in V^{4+} and V^{5+} valence states, which is reflected in the magnetic behaviour of the different oxide glasses.

Conclusions

From magnetic susceptibility data we have established that in $2P_2O_5$.PbO glass matrix both V^{5+} and V^{4+} ions are present, the last ones representing about 27 % from the total vanadium content for all studied samples. The V^{4+} ions are isolated or participate to dipole-dipole interactions for $x \leq 3$ mol %, but at higher content of V_2O_5 a mictomagnetic type behaviour is evidenced.

REFERENCES

1. G. Hochstrasser, Phys. Chem. Glasses 7, 178 (1996).
2. H. G. Hecht, T. S. Johnston, J. Chem. Phys. 46, 23 (1967).
3. H. Toyuki, S. Akagi, Phys. Chem. Glasses 13, 15 (1972).
4. L. D. Bogomolova, T. F. Dolgolenko, V. N. Jachkin, V. N. Lazukin, J. Mag. Res. 15, 283 (1974).
5. A. Paul, F. Assabghy, J. Mat. Sci. 10, 613 (1975).
6. H. Hosono, H. Kawazoe, T. Kanazawa, J. Non-Cryst. Solids 37, 427 (1980).
7. J. M. Dance, J. P. Darnaudery, H. Baudry, M. Monneraye, Solid State Commun. 39, 199 (1981).
8. O. Cozar, I. Ardelean, Gh. Ilonca, Mat. Chem. 7, 775 (1982).
9. O. Cozar, I. Ardelean, V. Simon, V. Mih, N. Vedean, J. Magn. Magn. Mat. 196-197, 269 (1999).
10. T. Allersma, J. D. Mackenzie, J. Chem. Phys. 47, 1406 (1967).
11. L. Stanescu, I. Ardelean, D. Stanescu, I. Hosciuc, Studia Univ. "Babes-Bolyai" Physica 1, 24 (1975).
12. M. Sayer, A. Mansingh, Phys. Rev. B 6, 4629 (1972).
13. B. D. Jordan, C. Calvo, Can. J. Phys. 55, 436 (1977).

14. R. Singh, J. S. Chakravarthi, Phys. Rev. B 55, 5550 (1997).
15. O. Cozar, I. Ardelean, I. Bratu, Gh. Ilonca, S. Simon, Studia Univ. "Babes-Bolyai" Physica XXXIV, 1, 94 (1989).
16. I. Ardelean, O. Cozar, Gh. Ilonca, V. Simon, V. Mih (to be published).
17. P. A. Beck, Metall. Trans. 2, 2015 (1971).
18. L. M. Mulay, Magnetic Susceptibility, Interscience, New York, 1973, p. 1773.

STUDIA UNIVERSITATIS BABEŞ-BOLYAI, PHYSICA, XLIV, 1, 1999

EFFECTS OF SUBSTITUTIONAL STUDIES AT Ca SITE BY Er ION ON THE INTERGRANULAR PROPERTIES OF (Bi, Pb):2223 AND (Bi, Pb)(Sr, Ba):2223 SUPERCONDUCTORS

A. V. POP*, I. GR. DEAC*, GH. ILONCA*, A. JURJIU*, V. POP**

ABSTRACT. The effect of partial substitution of Ca by Er in two series of (Bi, Pb):2223 superconductor samples was investigated by ac susceptibility measurements. In the $(Bi_{1.6}Pb_{0.4})$ $(Sr_{1.8}Ba_{0.2})$ $(Ca_{1-x}Er_x)_2$ Cu_3O_y(x=0;0.02) samples a linear dependence of intergranular temperature T_p as a function of AC field amplitude (H_{ac}) was obtained. This result agrees with Muller critical state model. In $(Bi_{1.8}Pb_{0.46})Sr_{1.88}(Ca_{1-x}Er_x)_2Cu_3O_y(x=0.02)$ the intergranular critical temperature T_p show a nonlinear dependence as a function of H_{ac}.

Introduction

Insulating phases in the Bi:2212 have been identified by systematic substitutional studies at the Ca site by Y and rare earth (RE) ion [1-4]. Resistivity and AC susceptibility studies have shown that superconductivity persist up to x=0.4 and a metal –semiconductor transition occurs for x>0.4. The most interesting observation is that the rate of T_c suppression for the superconducting phases is found to be identical for all RE ion [4]. For x>0. 5Y superconductivity disappears and the change in T_c with Y content has been attributed to a different distribution of holes the mixed valence Bi_2O_3 and Cu_2O planes[5].

Substitutions studies at the Ca site by Y^{3+} and RE^{3+} in Bi:2212 superconductor causes a repulsion between the CuO_2 layers thereby increasing the CuO_2-CuO_2 plane separation. The increase in rare–earth concentration, induce the increase of excess oxygen incorporated in between the Bi_2O_2 double layers [3, 4]. Moreover, the mechanism that governs the T_c suppression as well the mechanism of conduction at higher doping levels have not reported, hitherto.

* Faculty of Physics, Babes-Bolyai University, , 3400 Cluj-Napoca, Romania

** Department of Physics,Technical University, 3400 Cluj-Napoca, Romania

Substitutions studies by rare earth at the Ca site in (Bi, Pb):2223 superconductor are very few in the literature[6, 7]. With increasing Y concentration, the volume fraction of the high T_c(2223) phase decreased the (2212) phase increased and also T_c have decreased [6-8]. The substitution of a 4f element(such as Er) for Ca in (Bi, Pb):2223 can indirectly affect the processes from CuO_2 layers due to the influence it has on the charge transfer from BiO layers to the CuO_2 layers.

The effect of Er substitution for Ca on the intergranular properties of (Bi, Pb):2223 superconductor is discussed in this paper.

Experimental

Two series of $(Bi_{1.6}Pb_{0.4})(Sr_{1.8}Ba_{0.2})(Ca_{1-x}Er_x)_2\ Cu_3O_y$(x=0; 0.02-samples A) and $(Bi_{1.8}Pb_{0.46})(Sr_{1.88})(Ca_{1-x}Er_x)_2\ Cu_3O_y$(x=0; 0.02-samples B) polycrystalline samples were synthesized by conventional solid–state reaction [8]. The X-ray diffraction analysis confirmed the presence of a single "2223"phase in x=0.00 sample A and 75%vol. of "2223" phase in sample B. The amount of volume fraction of high T_c"2223" phase decrease to 55% and 35% for x=0.02Er in sample A and sample B, respectively[8]. A gradually changed of "2223" phase in to "2212" was evidenced with increasing Y concentration, also obtained by other authors [7].

Cylindrical specimens were cut from the sintered samples and used for AC susceptibility measurements. AC susceptibility measurements were performed by using an Oxford Instruments MagLab System 2000 equipment. The complex susceptibility for cylindrical samples was measured at 1kHz as a function of temperature and field amplitude.

Results and discussion

Fig. 1 and Fig. 2 show the real part $\chi'(T)$ and the imaginary part $\chi''(T)$ of the complex susceptibility behavior for different a. c. field for samples A and B with x=0.02 Er. For our samples, $\chi'(T)$ decreases below T_c and saturates at low temperatures. The temperature and field dependence of $\chi'(T)$ and $\chi''(T)$ shows a two–stage behavior which is found to be typical for sintered HTSC. For x=0.02 samples A and B, $\chi''(T)$ exhibits a single peak centred at T_p. The intergranular peak centred at T_p shift considerably to lower temperature in sample B than in sample A. This result suggest that the value of the intergranular pinning force in sample B is lower than in sample A. For x=0.00 sample, immaginary part of AC susceptibility, $\chi''(T)$, exhibit two peaks at T_p for intergranular transition and T_g for intragranular transition respectively. Our x=0.02 Er samples exhibit a single peak at T_p. The absence of intragrain peak in $\chi''(T)$ suggest the presence of smaller decoupled grains in x=0.02 Er samples [9].

The loss peaks shift to lower temperature by increasing H_{ac}. In our samples the critical transition temperature T_{cG} (the end of the superconductor diamagnetism for $\chi'(T)$) are very close to the inflection point temperatures T_c in the resistivity measurements, and T_p temperatures are nearly the same as the zero resistivity temperatures $T_c(\rho=0)$, [10].

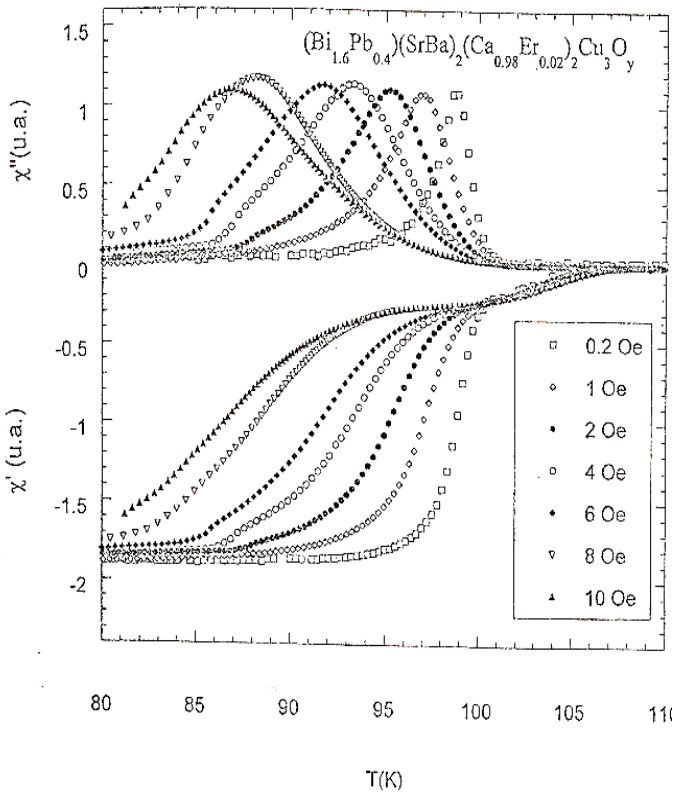

Fig. 1. Temperature dependence of the real part of χ' of the AC susceptibility and the immaginary part χ'' for x=0.02 Er in sample A at different AC field amplitudes H_{ac} ranging from 0.2 Oe to 10 Oe.

In order to investigate the effect for partial substitution of Ca with Er^{3+} on the intergranular pinning force, we studied the T_p dependence as a function of $H_{ac.}$ As can be see from Fig. 3, in the a. c. amplitude range 0-10AOe we obtain a linear dependence of T_p as a function of H_{ac} for samples A with x=0.00 and x=0.02 Er, described by :

$$T_p = T_0 - A\, H_{ac}.$$

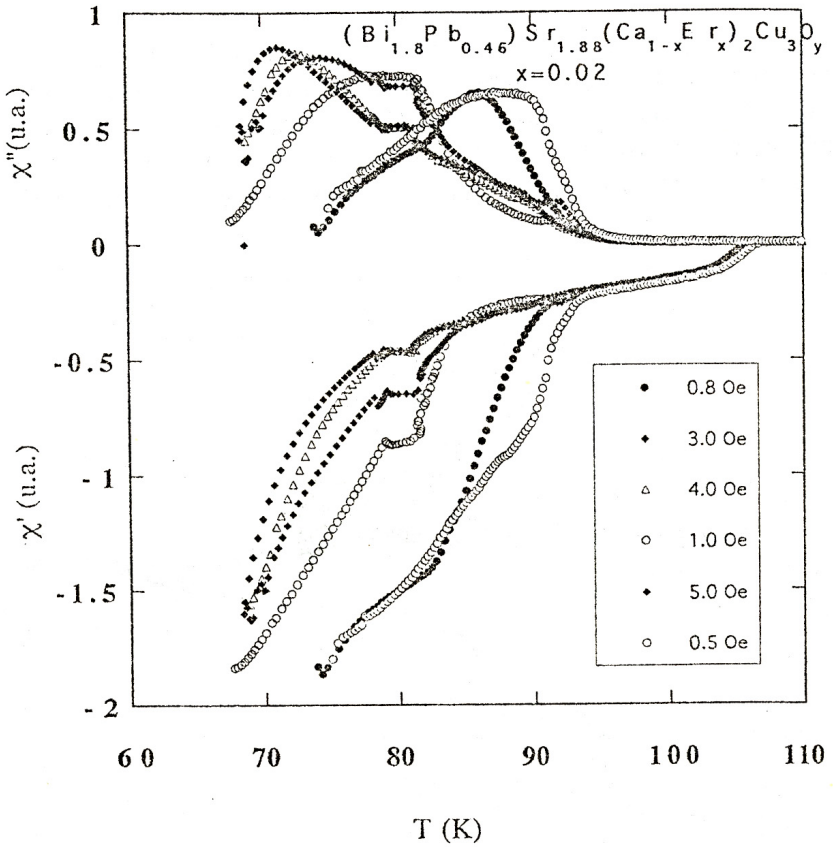

Fig. 2. Temperature dependence of the real part of χ' of the AC susceptibility and the immaginary part χ'' for x=0.02Er in sample B at different AC field amplitudes H_{ac} ranging from 0. 2 Oe to 10 Oe.

The experimental slopes A and T_{p0} are shown in Table 1.

Table 1

Sample	T_c [K]	$\rho(0)$ [$\mu\Omega$. cm]	T_0 [K]	A [K/Oe]	α_{JR}/α_0
x=0.00	109.0	87	106	2.97	1.0
x=0.02Er	104.0	578	98.4	1.19	9.9

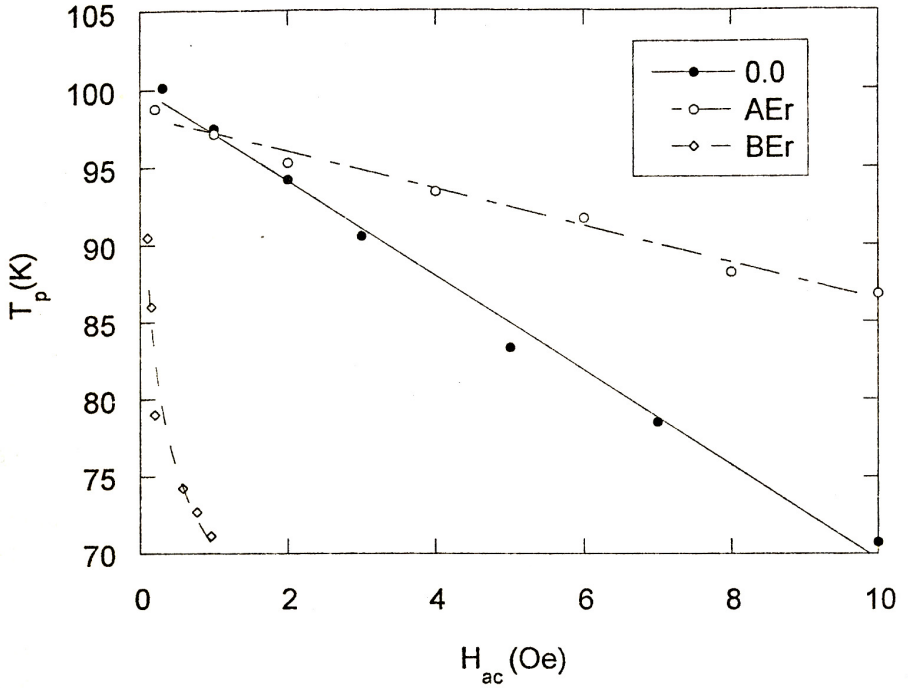

Fig. 3. Intragranular χ'' –peak temperature T_p versus AC field amplitude for x=0.00 (dark circles), x=0.02 Er in sample A (circles) and x=0.02 Er in sample B (squares)

The intergranular critical temperature T_p is described in the Müller critical state model [11] by a linear relation:

$$T_p = T_{p0} - T_{p0}[\mu_0 \mu_{eff}(0)/(2d\alpha_J(0))]^{1/2} H_{ac} \qquad (1)$$

where d is the height of cilindrical sample, μ_{eff} (0) is the effective permeability of the ceramic and $\alpha_J(0)$ is the intergranular pinning force density. By using in Eq. 1 the experimental slopes and T_{p0} values, the values d for cylindrical samples, and μ_{eff} (0) we obtain the values $\alpha_{J,R}/\alpha_0$, where α_0 are related to x=0.00 sample and α_{JR} to x=0.02 Er sample respectively. The $\alpha_{J,R}/\alpha_0$ values from Table 1 show that Er ions influenced the intergranular pinning force density.

By using in Eq. 1 the experimental slopes and T_{p0} values, the values d for cylindrical samples, and μ_{eff} (0) we obtain the values $\alpha_{J,R}/\alpha_0$, where α_0 are related to x=0.00 sample and α_{JR} to x=0.02 Er sample respectively. The $\alpha_{J,R}/\alpha_0$ values from Table 1 show that Er ions induced the increase for the intergranular pinning force density. The increase of intergranular pinning force density agree with increasing of residual resistivity in samples A.

In sample B with x=0.02 Er the T_p dependence as a function of H_{ac} is nonlinear (Fig. 3). The strongly depression of T_p for values of H_{ac} up to 1 Oe suggest a dramatical decrease of intergranular pinning force density with increasing the amplitude of alternative field. This result suggest that a partial substitution of Sr by Ba in (Bi, Pb):2223 sample A improve the quality of intergrain couplig in the presence of Er ions.

Conclusions

Two series of $(Bi_{1.6}Pb_{0.4})(Sr_{1.8}Ba_{0.2})(Ca_{1-x}Er_x)_2Cu_3O_y$(x=0;0.02-samples A) and $(Bi_{1.8}Pb_{0.46})(Sr_{1.88})(Ca_{1-x}Er_x)_2Cu_3O_y$ (x=0;0.02-samples B) polycrystalline samples were synthesized by conventional solid–state reaction method.

The samples A shows a linear dependence of intergranular temperature as a function of ac field amplitude. This dependence agrees with the Muller critical state model. The intergrain pinning force density obtained from this model increases for the sample with x = 0.02Er.

A strongly decrease of intergranular pinning force density with increasing the amplitude of alternative field was evidenced in sample B with x = 0.02Er.

The partial substitution of Sr by Ba in (Bi, Pb):2223 sample A improve the quality of intergrain couplig in the presence of Er ions.

REFERENCES

1. T. Tamegai, K. Koga, K. Suzuki, M. Ichihara, F. Sakai and Y. Iye, Jpn. J. Appl. Phys. 28, L112 (1989).
2. D. Mandrus, L. Forro, C. Kendziora and L. Mihaly, Phys. Rev. B 44, 2418(1991).

3. Y. Gao, P. Permabuco-Wise, J. E. Crow, J. O'Reilly, M. Spencer, H. Chen and R. E. Solomon, Phys. Rev. B 45, 7436(1992).
4. P. Sumana Prabhu, M. S. Ramachandra Rao, U. V. Varadaraju and G. V. Subba Rao, Phys. Rev. B 50, 6929(1994).
5. H. Yasuoka, M. Kakitana and H. Mazaki, Physica C185-189, 803 (1991).
6. K. Nanda Kishore, Phys. Stat. Sol. (A)143, 101(1994).
7. K. Nanda Kishore, S. Satyavathi, V. Hari Babu and O. Pena, Materials Science and Engineering B38, 267(1996).
8. V. Pop, Gh. Ilonca, G. Borodi, I. G. Deac, I. I. Geru, L. A. Konopko, V. I. Geru, I nt. J. Mod. Phys. B(1999)-in press.
9. Küpfer, I. Apfelstedt, R. Flükiger, C. Keller, R. Meier-Hirmer, B. Runtsch, A. Turowski, U. Wiech and T. Wolf, Cryogenics 29, 268(1988).
10. V. Pop, Gh. Ilonca, D. Ciurchea, M. Ye, R. Deltour I. I. Geru, V. G. Kantser, L. A. Konopko and V. I. Geru, *Int. J. Mod. Phys*. **B10**, 967(1996).
11. -H. Müller, *Physica* **C159** (1988) 717.

STUDIA UNIVERSITATIS BABEŞ-BOLYAI, PHYSICA, XLIV, 1, 1999

ELECTRICAL RESISTIVITY AND AC SUSCEPTIBILITY STUDY OF CO-DOPED $Y_{1-x}Zr_xBa_{2-2x}Ca_{2x}Cu_3O_{7-\delta}$ COMPOUNDS

I. GR. DEAC

ABSTRACT. Polycrystalline samples of stoichiometric composition $Y_{1-x}Zr_xBa_{2-2x}Ca_{2x}Cu_3O_{7-\delta}$ with x=0.0; 0.1; 0.2; 0.3 were prepared by the solid state reaction method. The effect of Zr and Ca, doped at the Y and Ba sites, simultaneously in the Y:123 composition was studied. Superconductivity was analyzed by both electrical resistivity and ac magnetic susceptibility measurements Electrical resistivity measurements showed that the $T_{c,\ R=0}$ value decreases from 88 K to 70.2 K as the level of doping (x) increases from 0.0 to 0.3 and they are in close agreement with ac susceptibility data. T_c depression with increasing dopants content is expected to be the effect of the in-plane oxigen disorder induced by the doping.

Introduction

Substitutions of various metallic dopants in high-T_c supeconductors (HTS'C) play an important role in understanding the origin of superconductivity and composition-structure-property correlations in these materials [1-5]. Several isovalent and aliovalent substitutions for the Y^{3+} and Ba^{2+} ions in $YBa_2Cu_3O_{7-\delta}$ have been made in order to study the behavior of these materials. It has been reported [1-4] that Ca substitutes on both the Y- and Ba-sites in a way that depends on the Ca concentration: the higher the Ca concentration the lower the relative fraction that substitutes onto the Y site. Such substitution have been found interesting since Ca^{2+} is the only alkaline-earth ion which can substitute for Y at its eight-fold coordinated site [4].

The valence state of Zr^{4+} is higher than that of $Y^{3+}$and the ionic radius of Zr^{4+} (0.8 Å) is somewhat smaller than that of Y3+ (0.89Å). The effect of Zr^{4+} on the behavior of Y:123 was investigated by some other workers [6], that found a slightly decrease of Tc with increasing the concentration of Zr^{4+} ions. Ca solubility on the Y site is limited by the

maximum oxidation state of Cu obtained under certain preparation conditions. If Ca concentration is above this limit Ca is forced to substitute for the isovalent Ba atoms. It is of interest to analyze to what extent the presence of zirconium ions will force Ca to substitute at the Ba site .

In this paper, we investigate the effect of simultaneous substitution of Zr and Ca for Y and Ba on the superconducting properties of $YBa_2Cu_3O_{7-\delta}$.

Experimental details

A series of compounds having the compositions $Y_{1-x}Zr_xBa_{2-2x}Ca_{2x}Cu_3O_{7-\delta}$ (x=0.0, 0.1, 0.2, 0.3) were prepared from a mixture of Y_2O_3, $BaCO_3$, CuO, CaO and ZrO_2 (all 99.99 % purity) powder materials through a solid-state reaction [9].

The phase and lattice parameters of the compounds were determined by X-ray powder diffraction using CuKα radiation with a computer-controlled spectrometer TURM-62.

Electrical resistivity measurements were carried out, in the interval from 77 K to 300 K. The resistivity of the samples was measured by a standard four-probe method, by using an Oxford Instruments MagLab System 2000 equipment. The samples were cut, using a low speed diamond saw, from pressed pellets into parallelepipeds of approximate dimensions 1x3x10 mm^3. High quality electrical contacts were made by applying silver loaded paint and using silver leads. Absolute values of the resistivity are accurate to within 10%, due to uncertainties in the geometrical factors.

The ac susceptibility measurements were performed by using the same Oxford Instruments equipment. The complex susceptibility was measured at 1 kHz as a function of temperature, at a field amplitude H_{ac} = 0.1 Oe. Bar specimens were cut from the sintered samples and used for ac susceptibility measurements.

Results and discussion

The X-ray diffraction patterns of YZrCaBCO suggested that these compounds have the YBCO structure. Small quantities of unreacted BaCO3 and CuO were found and these seem to be nearly the same in each sample [9] . Table 1. shows the behavior of the lattice parameters a,b and c as a function of x and some other quantitative data for the $Y_{1-x}Zr_xBa_{2-2x}Ca_{2x}Cu_3O_{7-\delta}$ system. There are no notice able structural changes in a, b, and c parameters and in the orthorhombicity of the system with Ca-Zr

doping. This behavior is consistent with the earlier reports [2-4] which have found that c-axis expands slowly, when Ca substitutes Y and then saturates, when Ca substitutes at the Ba site.

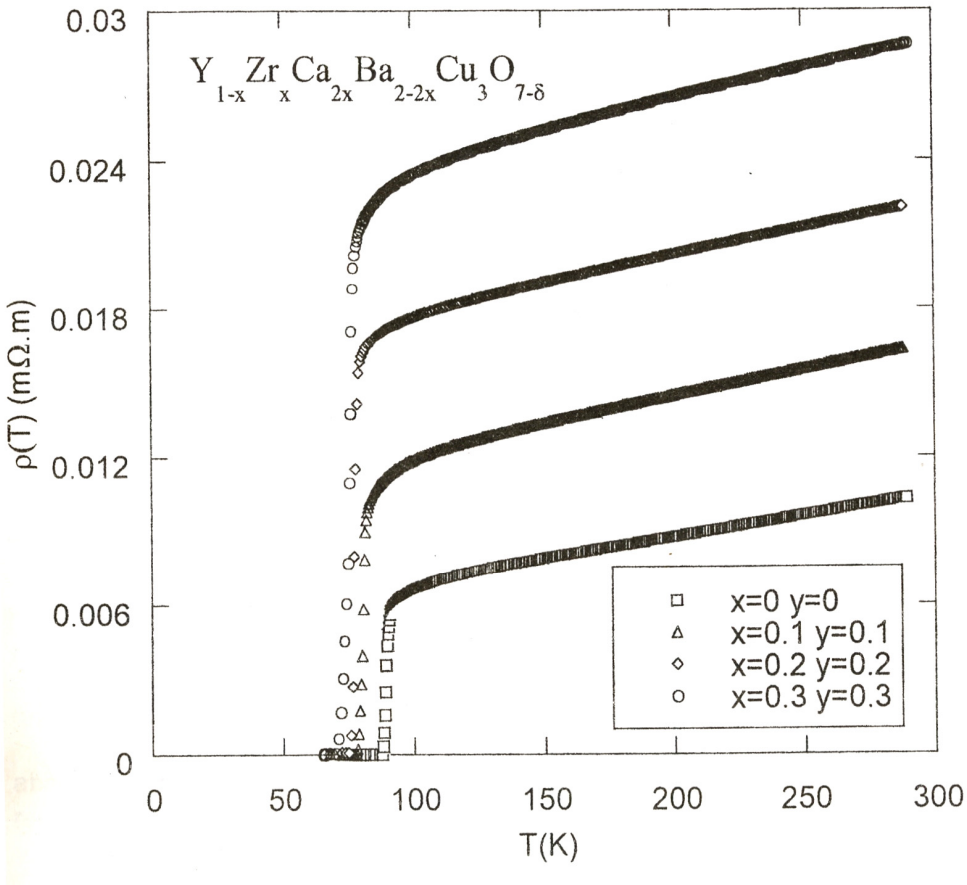

Fig. 1. Temperature dependence of the electrical resistivity for $Y_{1-x}Zr_xBa_{2-2x}Ca_{2x}Cu_3O_{7-\delta}$ compounds; x=0.0; 0.1; 0.2; 0.3

Figure 1 shows the temperature dependence of the electrical resistivity $\rho(T)$ for various x in the temperature range from 77 to 300 K. The resistivity of all the samples gradually decreased with decreasing temperature and then abruptly dropped when they transformed from the normal to the superconducting state.

Table I. Quantitative data for the $Y_{1-x}Zr_xBa_{2-2x}Ca_{2x}Cu_3)_{7\delta}$ system

Sample	a (Å)	b (Å)	c (Å)	$(b-a)/(a+b)$ %	T_c (χ) (K)	T_p (K)	$T_{c,R=0}$ (K)	$T_c(R)$ (K)	ρ_0 (μΩ cm)	α (μΩ cm/K)
x=0	3.825	3.887	11.676	0.8063	90.2	84.5	88	89.1	604	1.74
x=0.1	3.824	3.885	11.674	0.7910	83	79.3	78.2	80.6	1017	2.15
x=0.2	3.822	3.883	11.672	0.7915	79	72	74	78	1575	2.22
x=0.3	3.820	3.881	11.670	0.7933	76	66	71.1	75.8	2152	2.48

T_c(R) is the midpoint of the superconducting transition (determined from 10 % and 90 % of the extrapolated high temperature value). Above 120 K the resistivity shows linear temperature dependence for all the samples and therefore we assume that the normal state resistivity is given by $\rho_n = \rho_0 + \alpha \cdot T$. Here $\rho_{0 = } \rho_n$ (T=0) is the residual resistivity and α is the resistivity slope in the normal state.

The normal-state resistivity of the system, progressively increase with substitution and the slopes of the resistivity vs. temperature curves are nearly parallel at higher temperatures. In particular there is no signature of the so - called spin gap in resistivity behaviour. There is a well - established correlation between α and hole doping, and the single - crystal data, [10] in deed, show a linear dependence of α^{-1} on the carrier concentration. In a dilute (small concentration of defects) limit, one would expect the change in ρ_0 to be proportional to the concentration of in-plane defects [11 - 12]. In the present case, the increase of the residual resistivity could be related to oxygen disorder in the CuO2 plane created by the dopants.

The critical temperatures T_c (χ) determined as the temperatures where the ac - susceptibility becomes diamagnetic (for H_{ac} = 0.1 Oe) are in excellent agreement with Tc(R)'s. As seen in Fig. 2, for all the investigated samples χ' starts to decrease below Tc and at lower temperatures it begins to saturate at around 0.8 Tc. The first step corresponds to exclusion of magnetic field from the bulk superconducting grains and the second comes from magnetic shielding by the supercurents flowing between these bulk grains[13].

The imaginary component of the ac susceptibility, χ", measures the absorption of the flux inside the weak-links formed in the intergranular regions. χ" exhibits only a very smooth single peak at a temperature Tp (Tp<Tc). The absence of the second, intragranular peak near by T_c is a feature of strongly coupled, high quality ceramic superconductors where the coupling phase takes place immediately after the occurrence of superconductivity in grains[14].

The different valences of Y^{3+} and Zr^{4+} and the different ionic sizes of Ba^{2+} (rBa^{2+}=1.36 Å) and Ca^{2+} (rCa^{2+}=0.99 Å) could be favorable to increase the number of in-plane defects, and the oxygen disorder in planes seems to be (as shown in Ref.12) the main mechanism responsible for the observed decrease in Tc.

This assumption could explain, at least in aqualitative way, the electrical and magnetic behavior of these compounds in the normal state.

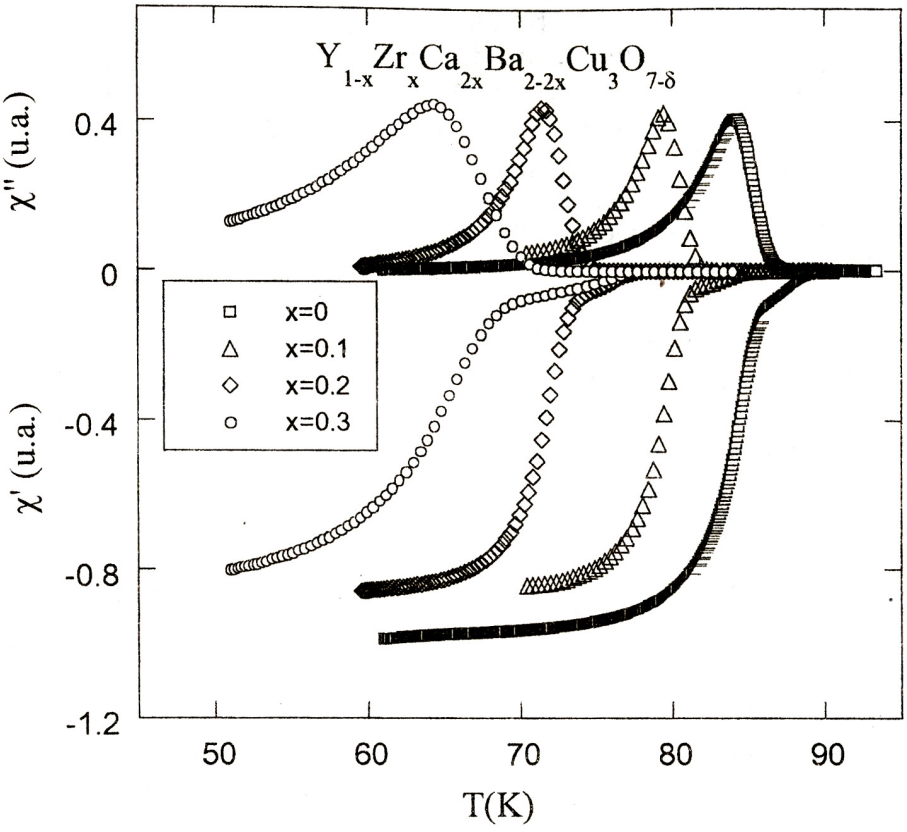

Fig. 2. Temperature dependence of the ac magnetic susceptibility for $Y_{1-x}Zr_xBa_{2-2x}Ca_{2x}Cu_3O_{7-\delta}$ compounds; x=0.0; 0.1; 0.2; 0.3

Conclusions

The superconducting compounds $Y_{1-x}Zr_xBa_{2-2x}Ca_{2x}Cu_3O_{7-\delta}$ with the oxygen-defect perovskite structure were obtained for x values between 0.0 and 0.3. There is no significant change in lattice parameters with Zr and Ca incorporation. Partial substitution of Zr^{4+} at Y^{3+} site could be favorable for Ca^{2+} to replace Ba^{2+}. The superconductivity transition was established in these compounds by both resistivity and ac susceptibility techniques. The T_c of the compounds decreases with increasing the dopants content, as a consequence of the oxygen disorder induced in planes, and this seems to be the main mechanism responsible for the observed decrease in Tc.

REFERENCES

1. A. Manthiram and J. B.Goodenough, Physica C159, 760 (1989).
2. R. G. Kulkarani, I. A. Shaikh, G. J. Bhalodia, D. G. Kuberkar, Phys Rev. B49, 6299 (1994).
3. R. G. Buckley et al. ,Physica C174, 383 (1991).
4. V. P. S. Awana and A. V. Narlikar, Phys. Rev. B49, 6353 (1994).
5. B. Fisher, J. Genossar, C. G. Kuper, L. Patlagan, G. M. Reisner and A. Knizhnik, PhysRev. B47, 4173(1993).
6. E. Burzo, V. Pop, J. Mat. Sci. 27, 5253, (1992).
7. T. Oka, et al., Physica C200, 55 (1992).
8. T. R. Chien, Z. Z. Wang and N. P. Ong, Phys. Rev. Lett. 67, 2088 (1991).
9. I. Gr. Deac, I. Pop, V. Pop and I. Burda, Mod. Phys. Lett B 11, 1175 (1997).
10. T. Ito, K. Takenaka, and S. Uchida, Phys. Rev. Lett. 70, 3995 (1993).
11. S. K. Tolpygo et al. Phys Rev. B53, 12462 (1996), and references therein.
12. S. K. Tolpygo et al. Phys Rev. B53,12454 (1996).
13. F. Gomorry, Supercond. Sci. Technol. 10, 523 (1997).
14. S. Ravi, Physica C 295, 277 (1998).

STUDIA UNIVERSITATIS BABEŞ-BOLYAI, PHYSICA, XLIV, 1, 1999

MAIN PARAMETERS OF THE MAGNETIC CORES MADE OF MOLIBDEN – PERMALLOY POWDERS

SABINA PICOŞ*

Abstract. The basis of this paper is a large experimental study which refers to the determination of the electric and magnetic parameters of the cores, from the molibden-permalloy iron powders concerning pressure density the resistivity the determination of the total magnetic losses and also the quality factor. Finally the equation of the quality factor, function of frequency of the coil feeding electric current on the basis experimental data have been determinated. The results are original other researches do not provide any information on this direction.

Introduction

The magnetic cores pressed from ferromagnetic powders have some advantages by compared to the casted ones as follows [3]:

- magnetic losses through eddy currents are reduced due to the protective coating of the granules before pressing;
- have reproductibile caracteristics;
- can be obtained after pressing final shapes without later mecanical manufacturing.

The adequate experimental researches have been using the molibden-permalloy iron powders MP_1 and MP_2. Their chemical composition and granulometric repartition are presented further.

Experimental process and the properties of magnetic cores [5]

Physical parameters

Two types of molibdenum-permalloy powders, MP1 and MP2, which have only a different grain size, were experimented in order to make an experimental study and a comparative analysis concerning the values of the main parameters of the magnetic cores made by pressing these types of powders.

* Technical University Iaşi, Romania

The grains size and distribution and also their chemical composition are shown in tables 1 and 2.

To insulate the grains, in order to decrease the magnetic losses, mainly through the eddy currents, the atomizated polystyrene, 2,5% of the powder weight, solved in benzene, finally in viscous shape, was used.

To decrease the friction forces that appear during pressing the zinc stearate was used as lubricant, 1% of the powder weight. The lubricant melting temperature (130^{o}C) allows its elimination without any difficulty during pressing, for increasing the product compactity, and before the insulator distruction due to the temperature which was experimentally measured to be between 190 and 200^{o}C.

For pressing the cores, pressures between 10^7N/m^2 and $5\cdot10^9$N/m^2 were used.

Table 1. Chemical composition of the used powders, %

Name of the Powder	Chemical composition, %											
	Fe	C	O	Si	SiO_2	Mn	P	S	Cu	N	Ni	Mo
Molibden-permalloy MP_1, MP_2	16,94	0,05					0,003	0,004			81	2,0

Table 2. Grain size and dimensional repartition

Name of the powder	Grai size, mm	Repartition, %	Grain shape
MP_1	0,045....0,075	100	Irregular polyhedron
MP_2	0,045.....0,01	100	Irregular polyhedron

Results and discussion

a) Density and compacting pressure [6]

Analysing the curve, which shows the influence of the compacting pressure on the apparent density of the cores (fig. 1), one can conclude:

- the compacting is stronger for the MP1 powder with larger grains. The maximum apparent densities are: $7,5\cdot10^3$ Kg/m^3 for MP_1 and $7,2\cdot10^3$ Kg/m^3 for MP_2.
- the magnetic cores porosity is ranged between 7% for the MP_1 powder made cores and 12% for the MP_2 powders.

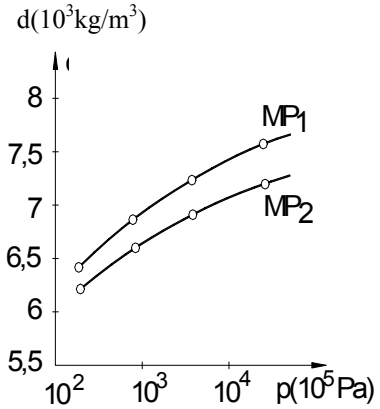

Fig. 1. The influence of pressure on densitv

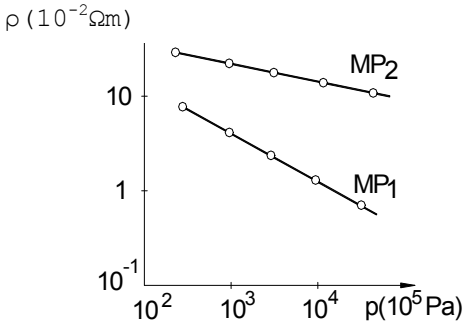

Fig. 2. The influence of pressure on resistivity

b) Study of the electrical resistivity [3]

Determination of the electrical resistivity has somehow relevance in indicating the losses through the eddy currents. To determine the electrical resistivity of magnetic cores with the transversal area S and length 1, using the relationship $\rho = R\frac{S}{l}$, initially the resisstance R of the samples has to be measured. In this purpose a bridge method was used.

The disc-shaped sample is introduced in a device which allows its gripping between two metallic electrodes, made of ground silver.

For achieving good contact between the sample and the silver electrodes, the sample extremities were silvered by covering with colloidal silver paste and then heat-treated for 1 hour at 100....130^{o}C.

The results concerning the influence of the compacting pressure on the sample resistivity are shown in fig. 2, from which the following conclusions can be drawn:

- the electrical resistivity simultaneously decreases with the increasing of the compacting pressure, due to the increasing of the grains contact surfaces and the decreasing of the samples porosity;

- for the larger grain size powder, the resistivity decreases due to the fact that the greater grain size, the better the compacting.

c) Study of the magnetic losses [4]

The total magnetic losses, represented by tgδ, have been determined by a bridge method for frequencies between 10 Hz and 1 MHz. The block diagram of the installation is shown in fig. 3, where: G – decadyc generator TR-0202; PA – admittance bridge SWM-3-2; mVs – selective millivoltmeter TT-1301; VE – selective voltmeter TT – 1302; T – torus (sample); R' – calibrated resistance.

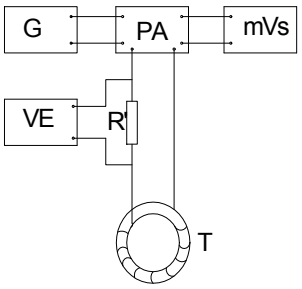

Fig. 3. Installation to measuring magnetic losses

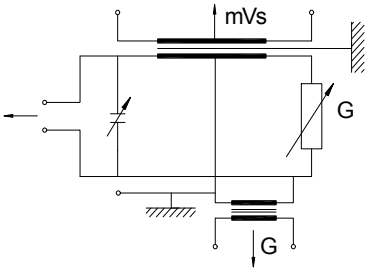

Fig. 4. Bridge schema of the admittance

The principle electric diagram has been extracted from the block diagram of the installation and shown in fig. 4. A torum-shaped sample has been used in the experiment.

For determining the magnetic field in which the sample lies, calibrated resistance R' = 1 Ω has been series inserted with the sample winding. On this resistance, the electronic voltmeter VE and therefore the current in the winding have measured the voltage drop.

In the bridge PA the sample admittance is compensated:

$$y = G - jB \tag{1}$$

through the gauged conductance G and susceptance B = ωC

with them, R and X = Lω are calculated with the following relationships:

$$R = \frac{G}{G^2 + B^2}; X = \frac{B}{G^2 + B^2} \tag{2}$$

and finally the total losses (expressed by tgδ) [18]

$$tg\delta = \frac{R - R_o - R'}{(L - L_o)\cdot \omega} \tag{3}$$

where R_o and L_o are the winding resistance and inductance respectively, without the magnetic cores; R, L are the resistance and the inductance of the coil with ferromagnetic powders core; and ω is the pulsation of the current.

The total magnetic losses have been measured in the following conditions:

- a constant frequency of 10^3 Hz and variable pressures between 10^7 and 10^{10} N/m^2;
- a constant pressure p=10^{10} N/m^2 and variable frequencies between 5 Hz and 10^5 Hz.

The influences of pressure and frequency on the total megnetic losses are presented in fig. 5 and fig. 6, from which, the following conclusions can be drawn:

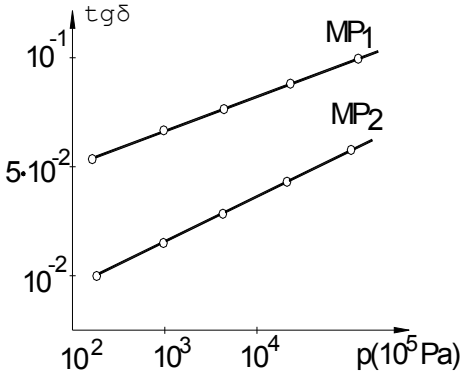

Fig. 5. The influence of pressure on the total magentic losses

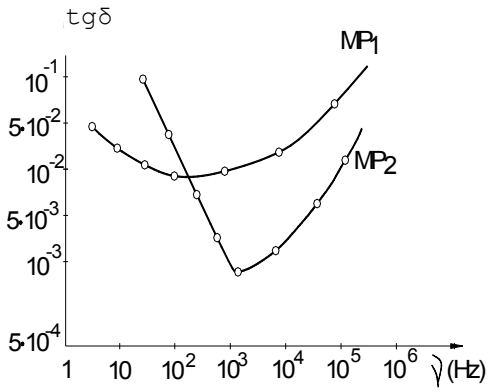

Fig. 6. The influence of the frequency on the total magentic losses

- total magnetic losses (tgδ) increase together with the compacting pressure of the magnetic cores and the powder grain size;
- total magnetic losses (tgδ) are influenced by the frequency of the supply current in the coil, a minimum value being observed for the so-called optimum frequencies.

The experiments pointed our the following minimum losses:

- for the magnetic core made of powders MP_1 - tgδ = $8 \cdot 10^{-3}$ at a frequency of 10^2 Hz;
- for the magnetic core made of powders MP_2 - tgδ = $8 \cdot 10^{-4}$ at a frequency of $2 \cdot 10^3$ Hz.

The conclusion is that the powders with smaller grains recommended for the magnetic cores running at higher frequencies.

d) Study of the quality factor Q [2]

The quality factor Q was measured by a Q-meter in the frequency range 50...$8 \cdot 10^4$ Hz for cores made of powder MP1 and in the range $8 \cdot 10^2$.... $5 \cdot 10^5$ Hz for powder MP2.

The frequency range was chosen so that the minimum values of the total magnetic losses, tgδ, to be included.

The experiments results concerning the quality factor values, shown in fig.7, emphasise the following:

- the quality factor varies together with the frequency;
- there is an optimal frequency for which a maximum value of the quality factor can be obtained.

The experiments results are:

- Q_{max}=135 for the cores made of powders MP_1 at the frequency of $3 \cdot 10^3$ Hz;
- Q_{max}=230 for the cores made of powders MP_2 at the frequency of $5 \cdot 10^4$ Hz;
- the optimal frequencies are greater for the cores made of powders with bigger grain size.

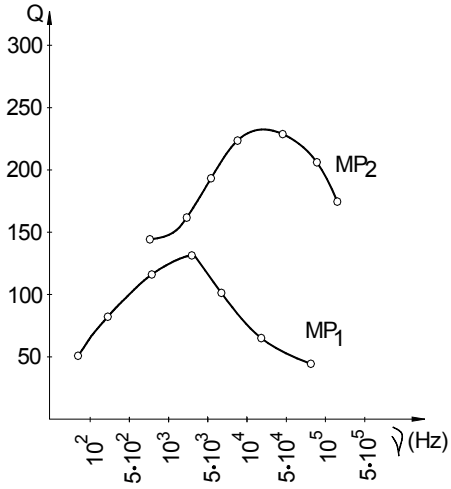

Fig. 7. The influence of frequency on the total quality factor.

e) Mathematical modelling of the influence of the frequency ν of the electric current on the quality factor Q

In order to obtain the optimum equation of the type $Q=f(\nu)$, based on the experimental data, for computing the quality factor as a function of the supply current frequency of the magnetic core coil, the following types of functions were taken into consideration: linear, logarithmic, power, exponential and polynomial.

The comparison criteria of these types of functions was the including percent of the experimental data R^2 (fig.8 a,b).The maximum value for R^2 was obtained for the polynomial function of the sixth degree.

The following equations were obtained for molibden-permalloy powders:

$Q=-0,002\ \nu^6+0,0962\ \nu^5 – 1,7591\ \nu^4 + 15,134\ \nu^3 – 63,966\ \nu^2 + 138,03\ \nu - 27,22$, with

$R^2 = 0,9938$, for the MP_1 powder and

$Q = - 0,0014 +0,0609\ \nu^5 – 1,0504\ \nu^4 + 8,4625\ \nu^3 – 31,487\ \nu^2 + 56,313\ \nu + 135,71$, with $R^2 = 0,998$, for the MP_2 powder.

Conclusions

The quality of the magnetic cores is influenced by several factors: physical factors (size, shape, granulometric distribution), chemical factors (nature of powder) and technological factors (compacting pressure, insulating materials).

The quality factor Q directly depends on the electrical resistivity of the magnetic cores and also on the supply current frequency of the coil, having a maximum value at a certain frequency denoted the optimal frequency.

The optimal frequency values and their scatter range, for which the quality factor has the maximum value, indicate the running field of these magnetic cores.

The frequency optimal range is experimentally determined on the basis of the powder grain size, for the same chemical composition and compacting pressure.

Through the variation of the powder grain size, a large running range of the optimal frequencies can be obtained.

For the experimental case presented in this paper we can calculate the quality factor for different frequencies, using the equations obtained through mathematical modelling.

Magnetic cores made of molibdenum-permalloy powders have a similar quality factor to those made of carbonyl.

Sort of function: Lineal Q_{MP1}=0.4484 ν + 109.64 R^2=0,0038 Logarithmic Q_{MP1}=13.565 Ln (ν) + 88.592 R^2=0,1197 Power Q_{MP1}=83.812 $\nu^{0,1462}$ R^2=0,159 Exponential Q_{MP1}=103,68 $e^{0,0067\nu}$ R^2=0,0098	Sort of function: Lineal Q_{MP2}=5.395 ν + 172.18 R^2=0,5563 Logarithmic Q_{MP2}=28.26 Ln (ν) + 160.18 R^2=0,6708 Power Q_{MP2}=162.35 $\nu^{0,1421}$ R^2=0,7031 Exponential Q_{MP2}=172,58 $e^{0,0027\nu}$ R^2=0,5782
Polynomial Q_{MP1}= 0,002 ν^6 + 0,0962 ν^5 – 1,7591 ν^4 + 15,134 ν^3 – 63,966 ν^2 + 138,03 ν – 27,22 R^2= 0,9938	Polynomial Q_{MP2}= 0,0014 ν^6 + 0,0609 ν^5 – 1,0504 ν^4 + 8,4625 ν^3 – 31,497 ν^2 + 56,313 ν – 135,71 R^2= 0,998

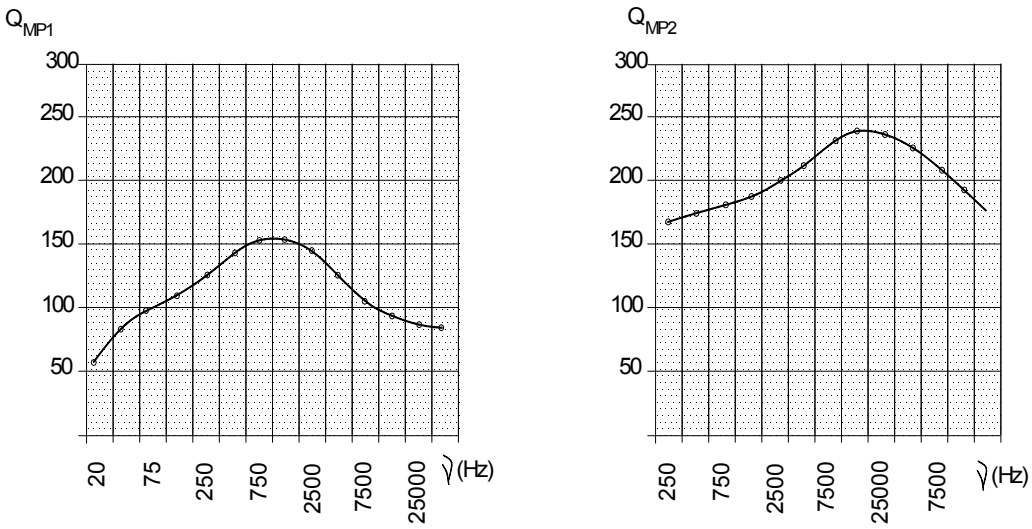

Fig. 8. Graphical representation of the equation Q=f(ν).

REFERENCES

1. E. B. Boltich, E. Oswald, M. Q. Hung, S. Hirosawa, W. E. Wallace and E. Burzo, J. Appl. Physics 57, 4106 (1985).
2. Eisenkolb F., *Fortschritte der Pulver Metallurgie*, Akademie Verlag, Berlin, 1963.
3. Goetzel, C. *Treatise on Powder Metallurgy*, vol. 1, New York-London Interscience Publ., 1949.
4. Hansner, H. H., *Progress in powder metallurgy*, Detroit, 1963.
5. Jones, W. D., *Osnovii poroskovoi metallurgii*. *Proisvostvo metalliceskih poroskov.* Izd. Mir. Moskva, 1965.
6. Jones, W. D., *Osnovii poroskovoi metallurgii*. *Presovanie I spekanie*. Izd. Mir. Moskva, 1965.
7. Legg, V. E., Given, F. J., *Compressed powder molibden-permalloy for high quality inductance coils,* Bell. Syst. T. J. 19, 385, 1940.
8. Owens, C. D. *Stability characteristics of molibden-permalloy powder cores,* El. Eng. 75, 252, 1958.
9. Picoş, S., *Studiul comparativ al miezurilor magnetice din pulberi feromagnetice de carbonil şi molibden-permaloi,* Rev. Construcşii de Maşini nr. 4-5, pag. 82-85, 1995.
10. Picoş, S., *Asupra procesului tehnologic de obşinere a semifabricatelor din pulberi feromagnetice* Rev. Construcşii de Maşini nr. 8-9, pag. 61-65, 1994
11. Picoş, S., *Experimental research about magnetic qualities of magnetic cores from densed molibden-permalloy dusts resing pressuring*. Internationales DAAAM Symposion, pag. 337-339, 1994.
12. Picoş, S. *Researches concerning the determination of the optimal field to woarking the magnetic cores of electrolytic iron and molibden-permalloy powders on the basis of the qualitative parameters: the magnetic losses and the quality factor. 12th International Conference on Process Control and Simulation.* Kosice, Slovac-Republic, 1996, pag. 154-157.
13. Richard, C. E., Bardell, P. R., Bukley, E. S., *Some properties and tests of magnetic powder and powder cores,* El. Comm. 28, 55, 1954.
14. Rives, J, Zamarro, J. M, Martin, E. Pereira C – Simple aproximation for magnetisation Courves and Hysteresis Loapes. I. E. E. E. Trans. On Mag. nr. 4, 1981.
15. Schackelton, W. J., Barber, J. G. *Compressed powder permalloy,* Trans. AIEE, 27, 429, 1928.

16. Schatt, W., *Pulvermetallurgie, Sinter und Verbundwerkstoffe,* Leipzig, VER Deutscher Verlag, 1977.
17. H. S. Göktürk, T. J., Fische, T. J, Kaylon, D. M., *Electric and magnetic properties of a thermoplastic elastomer incorporated with ferromagnetic powders*, I. E. E. E Transaction on Magnetics, vol. 29, nr. 6, November 1993.
18. Eder, X. F., *Moderne Messmethoden der Physics,* Teil 3, Berlin, 1972.
19. Cedighian, S., *Ferite*, Bucureşti, Ed. Tehnică, 1980.

STUDIA UNIVERSITATIS BABEŞ-BOLYAI, PHYSICA, XLIV, 1, 1999

THE TEMPERATURE BEHAVIOUR OF THE THERMAL PARAMETERS OF TRIGLYCINE SULPHATE, AROUND THE FERRO-PARAELECTRIC PHASE TRANSITION, AS OBTAINED BY PHOTOPYROELECTRIC CALORIMETRY

C. MARTIN*, C. ANDREI*, AL. DARABONT*,
D. DADARLAT, D. BICANIC***, A. PASCA***

ABSTRACT. The photopyroelectric (PPE) calorimetry in the standard configuration, with optically opaque sample and thermally thick sample and sensor, was applied for thermal characterization of triglycine sulphate (TGS). The temperature behaviour of all static (volume specific heat) and dynamic (thermal conductivity, diffusivity and effusivity) thermal parameters was measured, in a temperature range that encompasses the ferro-paraelectric phase transition.

Introduction

During the last years, photothermal techniques have been largely applied to the study of thermal and optical properties of condensed matter. Photoacoustic, photothermal radiometry and deflection, thermal lensing and photopyroelectric techniques, in various configurations, have been used; the selection depended on the experimental conditions and on the purpose of the investigation [1]. It has also been shown that, under particular experimental conditions, the photopyroelectric (PPE) method is a very sensitive calorimetric technique, able to offer qualitative and quantitative information about the values and the temperature behaviour of the static (specific heat) and dynamic (thermal conductivity, diffusivity and effusivity) thermal parameters of (semi)liquid and solid samples [2,3]. Phenomena connected with the temperature behaviour of the thermal parameters, as phase transitions, were also studied by PPE [2,5]. Concerning the samples

* Faculty of Physics, Cluj-Napoca University, Romania

** Institute of Isotopic and Molecular Technology, POB 700, Cluj-Napoca 5, R-3400 Romania

*** Wageningen Agricultural University, Department of Agricultural Engineering and Physics, Agrotechnion, Bomenweg 4, 6703 HD, Wageningen, The Netherlands

under investigation, they ranged from "classical" (magnetic, ferroelectric, superconducting, etc, materials) up to more sophisticated systems as foodstuffs, agricultural and biological samples [1]. The main advantages of the PPE method are the simplicity, high sensitivity and fast time response. The critical behaviour of the thermal parameters of TGS was previously investigated by classical calorimetry [6]. PPE was used before only for qualitative measurements (detection of Curie point) [7].

In this paper we will investigate quantitatively the critical behaviour of the thermal parameters of this material.

Theory

Basically, the PPE method is concerned with the measurement of the heat developed in a sample (due to the absorption of a modulated light), with a pyroelectric sensor, situated in intimate thermal contact with the sample [7]. Various experimental configurations and PPE cell geometries have been proposed to increase the sensitivity of the method and the accuracy of the measurements, and much effort has been devoted to simplifying the general expression for the PPE signal and to obtain experimental conditions for which the amplitude or phase of the PPE voltage depends solely on a single sample's related thermal parameter, allowing its direct evaluation [8]. Between these particular cases the most suitable seems to be the standard configuration with opaque sample and thermally thick sample and sensor.

In this configuration, the incident radiation impinges on the front surface of the sample, while the sensor, situated in a good thermal contact with the rear side of the sample, measures its temperature variation. A given medium is called "thermally thick" if its geometrical thickness, l, is larger than the thermal diffusion length, u (if l<u, the layer is thermally thin). For a modulated excitation, the thermal diffusion length is connected with the thermal diffusivity, D, and angular chopping frequency, w, through the relationship:

$$u = (2D/w)^{1/2} \quad (1)$$

It has been shown that, in this standard configuration, if the sample and sensor are thermally thick, and, additionally, the sample is opaque, the amplitude, V, and phase, F, of the complex PPE signal are given by :

$$V = V_0 \frac{\exp\left[-l_s \left(\frac{w}{2D_s} \right)^{1/2} \right]}{e_p + e_s}$$

$$F = F_0 - l_s (w/2D_s)^{1/2} \quad (3)$$

In Eqs.(1-2), V_0 is a calibration factor depending on the power of the incident radiation and on the electrical and geometrical properties of the equivalent sensor-lock-in circuit, F_0 is a frequency independent offset, and e represents the thermal effusivity, related with the other three thermal parameters, thermal diffusivity, D, conductivity, k, and volume specific heat, C, by:

$$e = (Ck)^{1/2} ; \; e = kD^{1/2} \quad (4)$$

The subscripts 's' and 'p' refer to the sample and pyroelectric sensor, respectively.

The main conclusion of this theoretical section is that it is possible to obtain the temperature behaviour of all four thermal parameters, from one measurement (see Eqs. (2-3)), if we have for the investigated sample an isolated value of a thermal parameter (another than D), to calibrate the amplitude measurements (Eq. (2)). Fortunately, for TGS, such data (especially room temperature values of D and k) are available in the literature.

Experiment

a. The preparation of the TGS single crystals.

TGS is a representative compound of the ferroelectric materials class. In the ferroelectric state it belongs crystallographically to the $P2_1$ /m space group of the monoclinic system. This compound has a very good solubility in water and, for this reason, it can be obtained in single crystalline form from aqueos solution.

The starting materials were: glycine (glycocoll) and concentrated H_2SO_4 acid. For the preparation of polycrystalline TGS these starting materials were mixed in a 3:1 molar ratio. The resulted polycrystalline triglycine sulphate, $(NH_2CH_2COOH)_3 \; H_2SO_4$, was purified by repeated recrystallization from distillated water. The growth of relatively large and good-quality crystals from aqueous solutions takes place in two stages. First, a crystal nucleus (seed) must be formed, which then grows in a new solution to the desired dimension. Both the formation of the nucleus (seed) and its further growth are based on the relation between solubility and

temperature. The nuclei are obtained from unstable solutions, from highly supersaturatted solutions. The require supersaturation is generally obtained by evaporation of the solvent or by a constant decrease of the temperature. These methods may be carried out in various ways. We have produced seed crystals by temperature decrease. A solution which is saturated at 5-7 ^{0}C above the saturation temperature was prepared from about 200 ml distillated water. It was filtered at a temperature of 1-2 ^{0}C above the saturation temperature and was left to cool in a covered glass to the room temperature (aprox. 24 ^{0}C). After few hours, a large number of little single crystals (seed crystals) precipitated. From these crystals, the best seeds were selected and used for further growth to the desired dimensions. For the growth of large single crystals of TGS an aqueous solution, saturated at 35 ^{0}C, was warmed to 38 ^{0}C and filtered into a 0.8-1 l glass and was placed in a thermostat. The previously prepared seed crystals were placed in the solution at suitable distances. After these operations the thermostat was kept at 35.2-35.5 ^{0}C and finally to the saturation temperature. The decrease of temperature has begun only few hours later. The growth was concluded at room temperature. After few weeks we obtained single crystals of size: 30x40x10 mm .

b. The experimental set-up.

The experimental set-up is presented in Fig. 1.

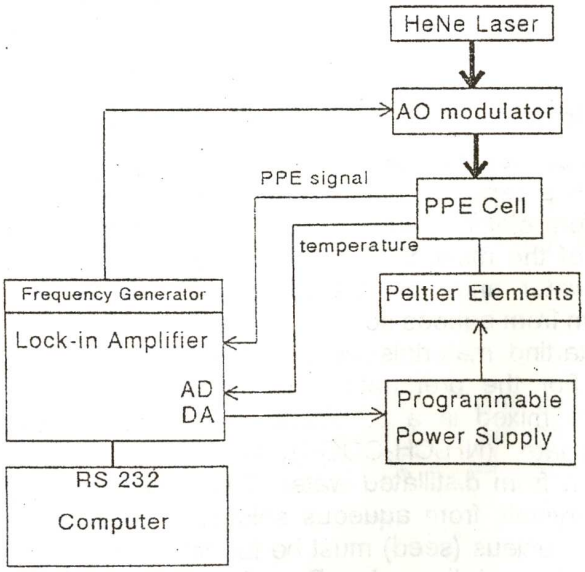

Fig. 1. The experimental set-up used for PPE calorimetric investigations.

The radiation source was a 10mW HeNe laser (Melles Griot), chopped by an acousto-optical modulator. A lock-in amplifier (SR 850 Stanford Research), was used for signal processing. The temperature of the cell was controlled with two Peltier elements, through a programmable power supply; the temperature variation rate was 0.6 ^{0}C/min. A PC was used for data acquisitions.

A 0.3 mm thick $LiTaO_3$ single crystalline pyroelectric sensor was glued with silicone grease to a 0.37 mm thick sample, which was short-cuted with silver paste to avoid the electrical influences on the signal. The front surface of the sample was blackened in order to make it opaque and to increase the absorption coefficient of the radiation.

Results

An example of room temperature frequency scans of the phase of the PPE signal for TGS is presented in Fig. 2.

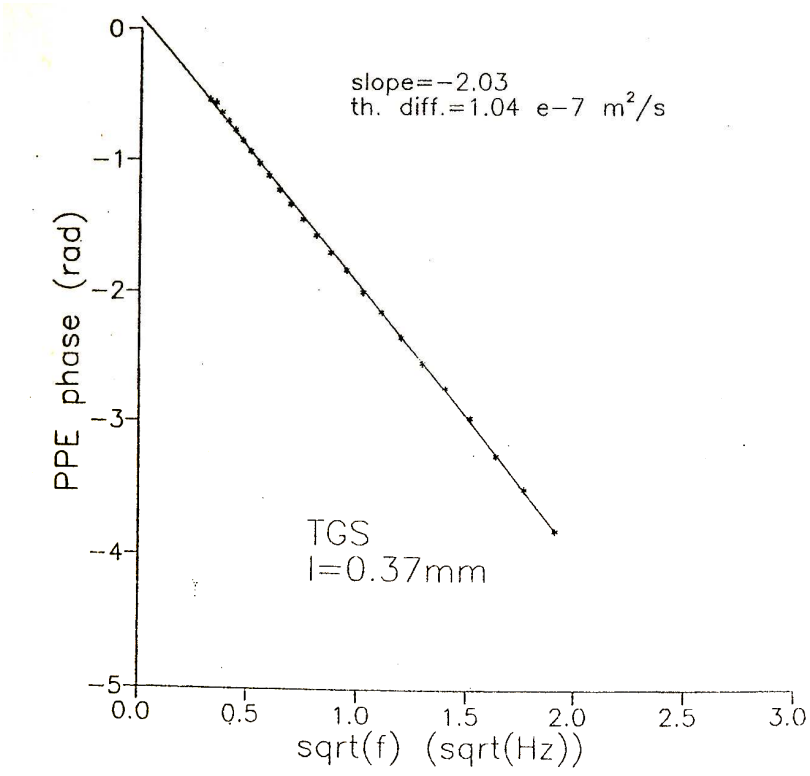

Fig. 2. Room temperature frequency scan for the phase of the PPE signal.

As mentioned in the theoretical section, in the thermally thick regime for the sample and sensor, the dependence F vs. sqrt(f) is linear and the slope of the curve allows the direct and absolute calculation of room temperature thermal diffusivity

For the temperature scan, a chopping frequency of 0.3 Hz assures both a thermally thick regime for the sample and sensor and a good enough (higher than 20) signal to noise ratio.

Figs. 3 and 4 display the temperature scans for the amplitude and phase of the complex PPE signal. The anomaly present at 49 ^{0}C is associated with the ferro-paraelectric phase transition of TGS.

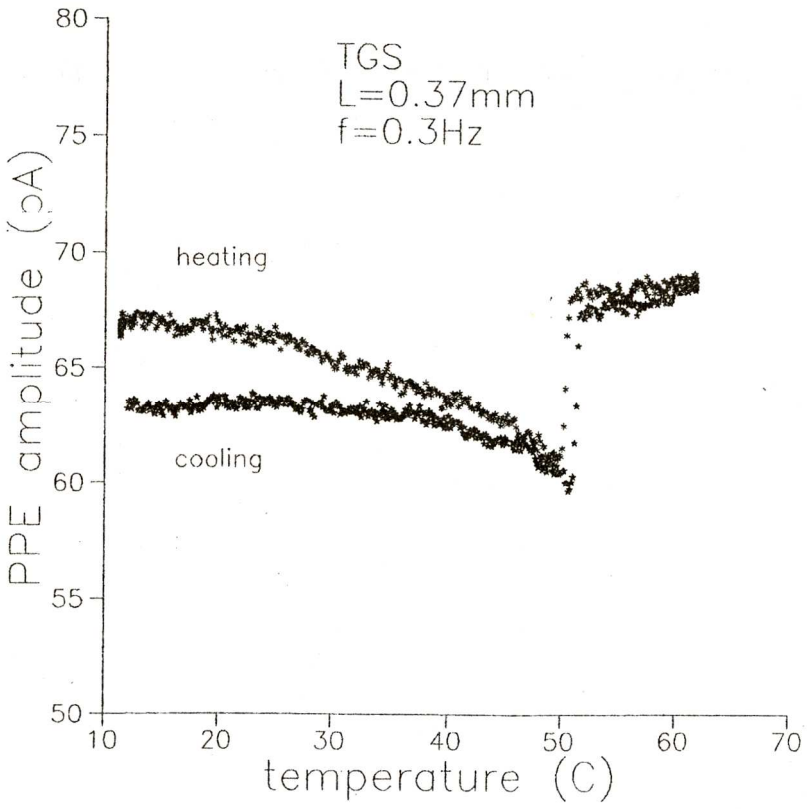

Fig. 3. Temperature scan for the amplitude of the PPE signal.

Using Eqs. 2-4 one can obtain the critical behaviour of all 4 thermal parameters. They are presented in Figs. 5-8.

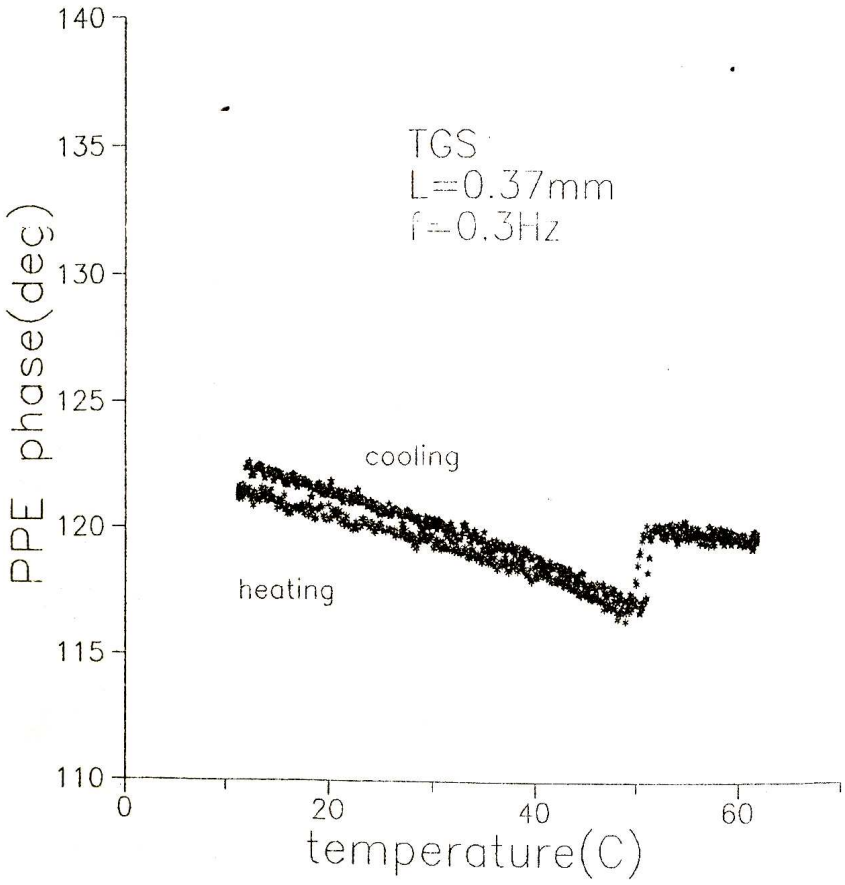

Fig. 4. Same as Fig. 3, but for the phase of the signal.

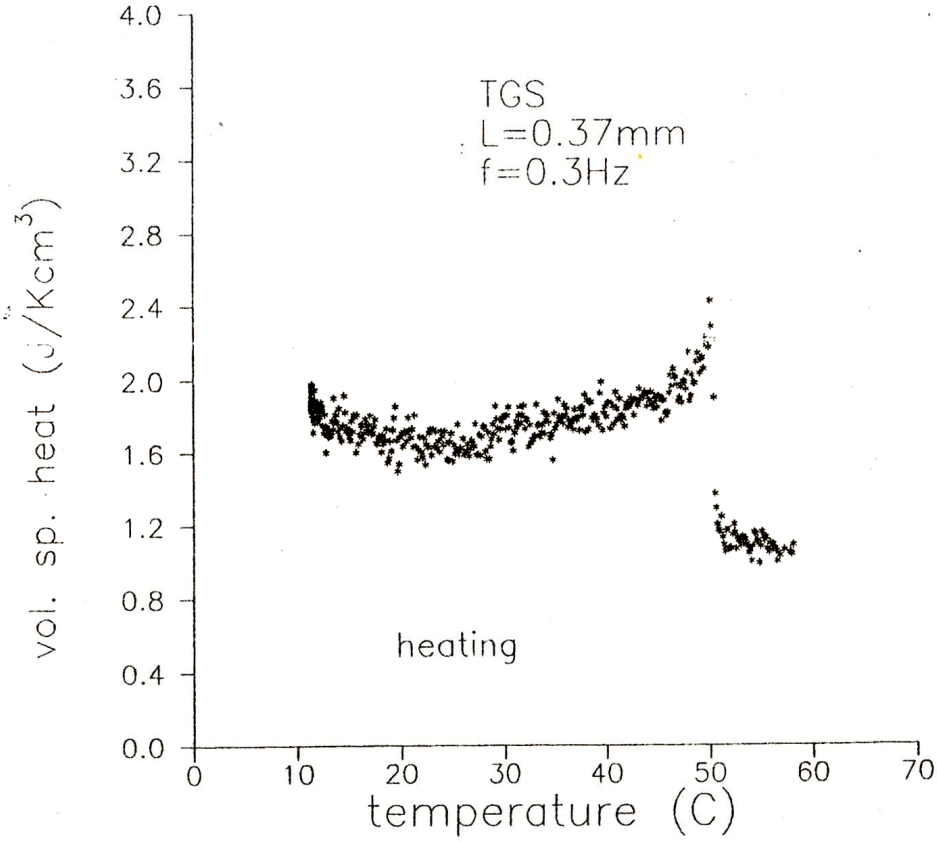

Fig. 5. The temperature behaviour of the volume specific heat for TGS in a temperature range encompassing the ferroelectric Curie point.

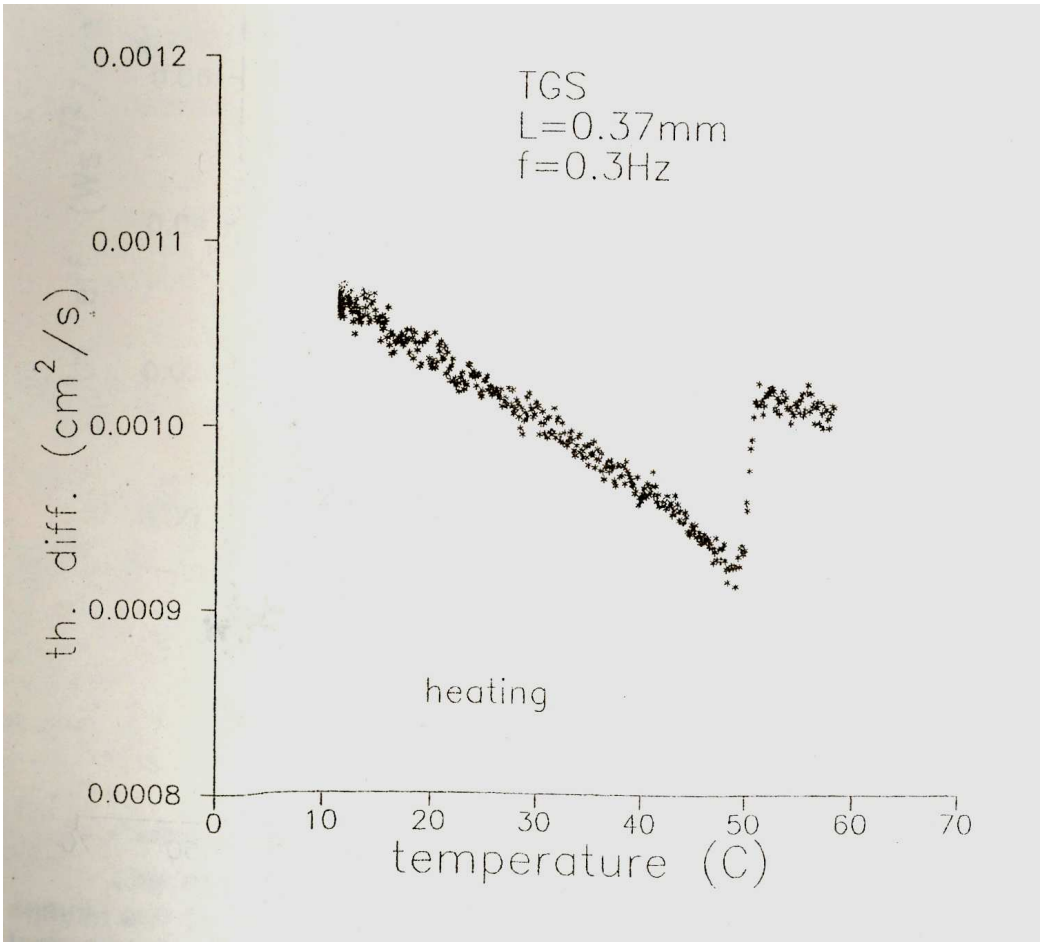

Fig. 6. Same as Fig. 5, but for the thermal conductivity.

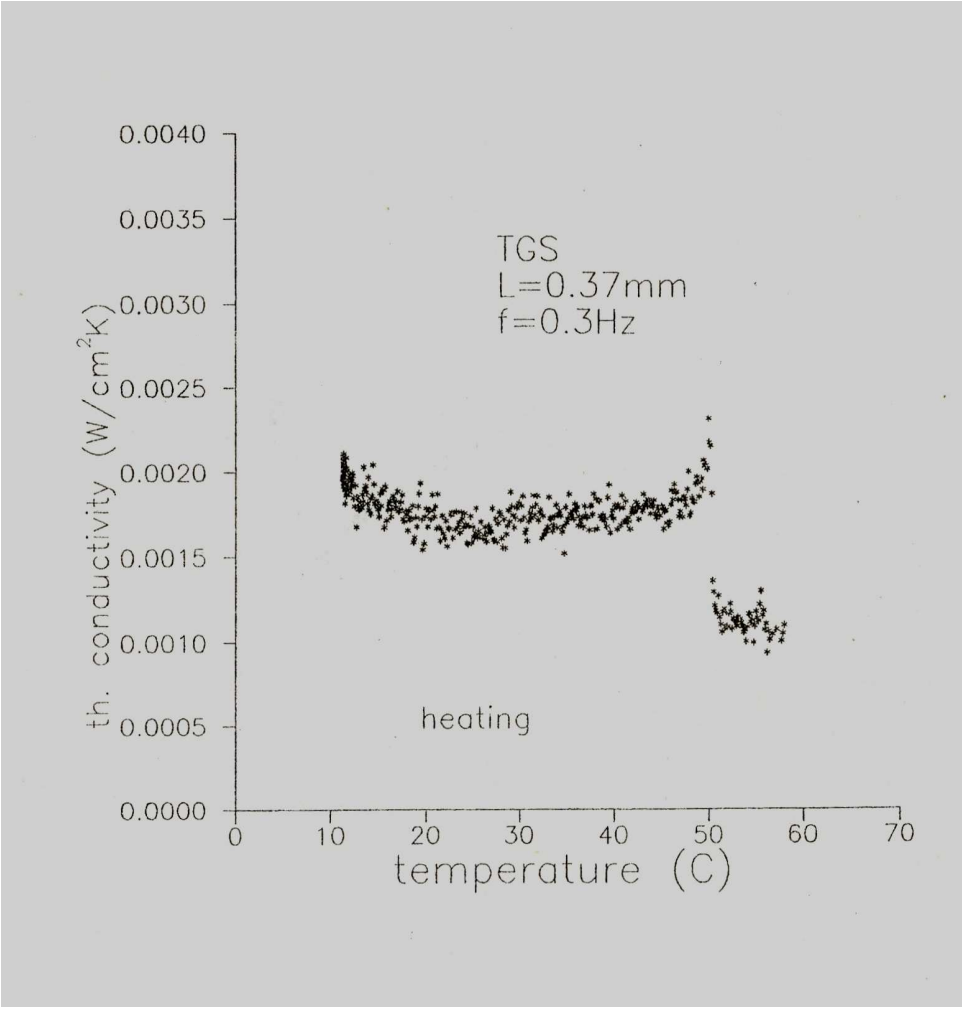

Fig. 7. Same as Fig. 5, but for the thermal diffusivity.

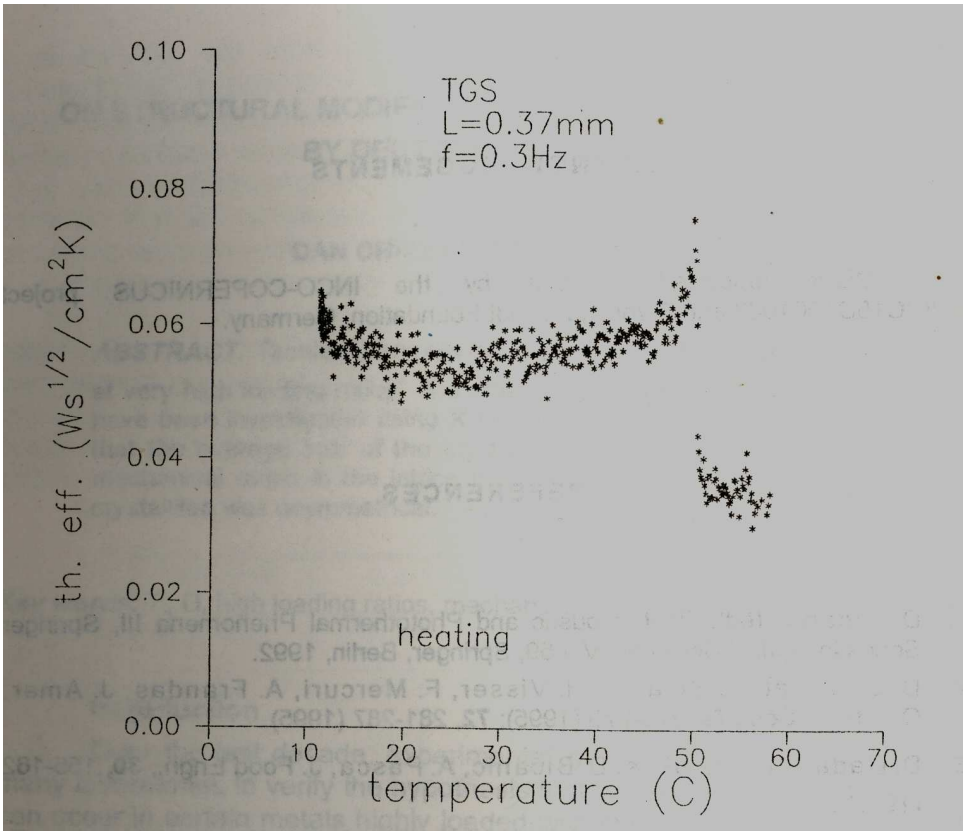

Fig. 8. Same as Fig. 5, but for the thermal effusivity.

Conclusions

The PPE calorimetry (in the standard configuration, with opaque sample and thermally thick sensor and sample) was used to measure the temperature behaviour of the static and dynamic thermal parameters of TGS in a 10-60 ^{0}C temperature range. The ferro-paraelectric phase transition was detected at around 49 ^{0}C. The critical behaviour of the thermal parameters indicates a second order phase transition. The results are in agreement with data obtained by classical calorimetry.

The main advantage of the PPE technique concerning the calorimetric investigations is the possibility of obtaining the temperature behaviour of all static and dynamic thermal parameters from one measurement.

ACKNOWLEDGEMENTS

Work supported in part by the INCO-COPERNICUS project ERBIC15CT961003 and A.von Humboldt Foundation, Germany.

REFERENCES

1. D. Bicanic (ed), Photoacoustic and Photothermal Phenomena III, Springer Series in Optical Sciences, Vol 69, Springer, Berlin, 1992.
2. D. Dadarlat, D. Bicanic, H. Visser, F. Mercuri, A. Frandas, J. Amer, Oil Chem. Soc., **72**, 273-279 (1995); **72**, 281-287 (1995).
3. D. Dadarlat, J. Gibkes, D. Bicanic, A. Pasca, J. Food Engn., **30,** 155-162 (1996).
4. D. Dadarlat, D. Bicanic, J. Gibkes, W. Kloek, I. van den Dries, E. Gerkema, Chem. Phys. Lipids**, 82**, 15-23 (1996).
5. M. Marinelli, F. Mercuri, U. Zammit, R. Pizzoferrato, F. Scudieri, D. Dadarlat, Phys. Rev**. B49**, 9523-9532 (1994).
6. J. del Cerro, J. Phys. E: Sci. Instrum., **20**, 609 (1987).
7. D. Dadarlat, M. Chirtoc, C. Neamtu, D. Bicanic, J. Phys. Chem. Solids, **51**, 1369 (1990).

STUDIA UNIVERSITATIS BABEŞ-BOLYAI, PHYSICA, XLIV, 1, 1999

ON STRUCTURAL MODIFICATIONS INDUCED IN TI SAMPLES BY DEUTERIUM LOADING

DAN CHICEA*, EMIL INDREA**

ABSTRACT. Titanium samples have been loaded with deuterium at very high loading ratios. The structural changes of the samples have been investigated using X ray diffraction. The results reveal that the average size of the crystallites size has decreased, the mechanical strain in the lattice increased and the fracture of the crystallites was asymmetrical.

Key words: Ti, D, high loading ratios, mechanical strain, bulk fracture.

Introduction

Over the last decade, experimental work [1], [2] has been done in many laboratories to verify the hypothesis that low energy nuclear reactions can occur in certain metals highly loaded with hydrogen isotopes. Some of the accepted models that try to offer an explanation for of the very low intensity nuclear reactions in solids assume that a microscopic ion acceleration mechanism occurs when the crystal bulk fractures [3], [4] as a result of the large mechanical strain which accompanies the high hydrogen isotope loading ratios. The subject of this paper is the structural modifications produced in the bulk of the Ti slab samples by the loading of Deuterium at very high loading ratios.

1. Sample preparation

Four samples consisting of Ti slabs, 1.5 x 8 x 9 mm., were the subject of a special surface activation treatment for the deuterium to be absorbed in the bulk, which has been extensively described in [5], [6]. The loading process was conducted slightly different for the four samples.

---

* University Lucian Blaga, Physics Dept., Str. Dr. I. Ratiu nr. 7-9, Sibiu, phone:069-211338, fax: 069-210512, email:dchicea@vectra.sibiu.ro (pt. corespondență)

** Institute of Isotopic and Molecular Technology, Cluj-Napoca, Str. Donath 10.

The activated samples were loaded from the gas phase at temperatures ranging from 500 ^{o}C to 820 ^{o}C and initial Deuterium pressures from 6 to 8.25 MPa. The deuterium absorption process in the samples 2 and 3 was very fast, leading to the rapid creation of a high loading ratio region under the surface and causing mechanical strain in the bulk of the sample, producing macroscopic cracks on the surface of the slabs accompanied by the specific noise in the minutes when the temperature was high and for another 10 minutes while the temperature of the reactor was decreasing.

The values of the initial mass, the mass of the absorbed Deuterium and the average loading factor X defined as the ratio between numbers of D and of Ti atoms, for the four samples, are presented in the table 1.

Table 1. The characteristics of the samples used in the experiments

Sample	m_{Ti}, g	M_D, g	$X=N_{Ti}/N_D$
1	9.7	0.2322	0.573
2	6.9	0.556	1.93
3	3.9	0.308	0.31
4	4.9350	0.2771	1.345

2. X-ray structural analyse

One of the samples (number 2) has been analysed by X-ray diffraction. The sample, first unloaded and than loaded at X=1.93 have been irradiated with the Co Kα line (λ=1,78902 Å). The recorded reflected intensity I=f(2θ) was analysed using the program XRLINE [7]. The program outputs the distribution of the crystallites by their sizes and the distribution of the mean quadratic deformation $<\varepsilon^2>^{1/2}$ of the crystallites.

Table 2. The results of the X-ray analyses of the samples before and after loading with Deuterium at a loading factor of 1.93.

Sample	$2\theta_{max}$, ^{o}	$\Delta 2\theta$, ^{o}	D_m, Å	$<\varepsilon 2>^{1/2}$
Initial	47,40	0,681	164	$1,34*10^{-3}$
Final	48,15	0,812	135	$1,76*10^{-3}$

The results are presented in table 2, where $2\theta_{max}$ is the position of the maximum of the diffracted intensity, $\Delta 2\theta$ is the width of the distribution, D_m is the average size of the crystallites.

The average size of the crystallites decreased from 164 to 135 Å, revealing that the mechanical stress produced by the absorbed deuterium induced the fracture of the larger crystallites. Rather unusual seems to us to be the minimum of the mean quadratic deformation at the value of 120 Å for the size. A possible explanation might be that the larger crystallites absorbed deuterium and were fractured asymmetrically, one of the fragments having a preferential size around 120 Å and presenting reduced mechanical stress. Figures 1 and 2 present the values of the mean quadratic deformation of the crystallites before and after loading the sample with deuterium.

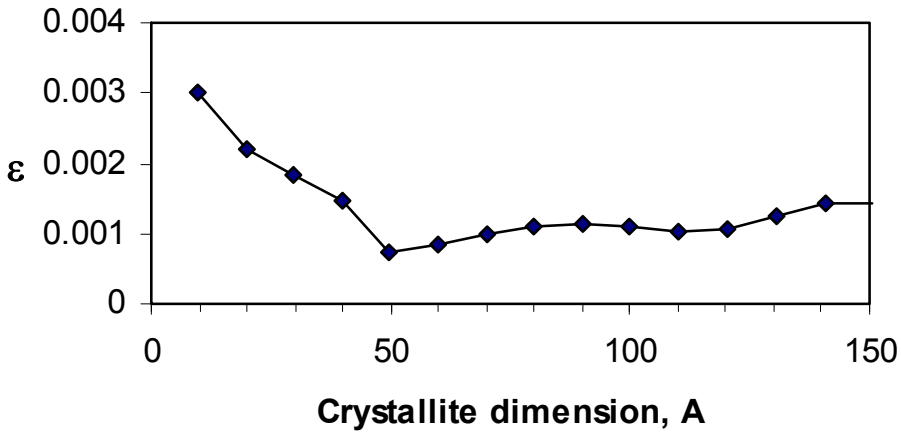

Fig. 1. The mean quadratic deformation of the crystallites before loading the sample with deuterium (first order spline).

The mean quadratic deformation for the crystallites having a smaller size is increased and the curve in figure 2 has the same variation as for the unloaded sample. This suggests that the small crystallites were loaded at a smaller loading ratios than the larger ones, as their bulk areas represent smaller part of the material compared to the under surface area than for larger crystallites. The mechanical stress produced by the absorbed Deuterium was lower for the small sized crystallites than for the large sized, and that left them unfractured.

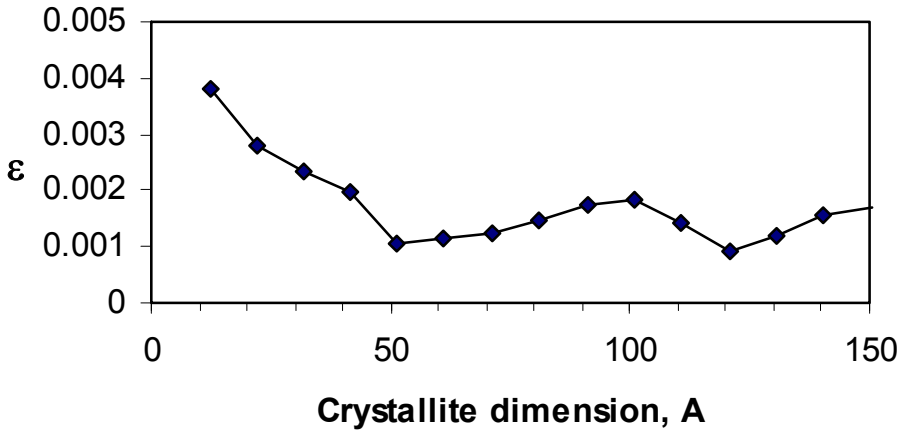

Fig. 2. The mean quadratic deformation of the crystallites after loading the sample with deuterium (first order spline).

Conclusions

The results of the X-ray structural investigation of the slab Ti samples loaded with deuterium from the gas phase, at temperatures of 800 ^{o}C reveal that the crystallites absorbed it preferentially. The larger crystallites absorbed the deuterium up to a larger loading ratio, becoming the bearer of a larger mechanical strain that statistically fractured them with a larger probability than the small sized ones. The difference between the mean quadratic deformation versus the crystallite size before and after the loading indicate that as an average the larger crystallites are less strained after the loading than before and that the small crystallites are more strained after the loading.

Another interesting result is that the large crystallites get fractured in an asymmetrical way, which is supported by the local minimum in the figure 2, leaving one of the fragments with a size close to 120 - 130 Å, as indicated by the value of the average size of the crystallites. The size of 120 Å has been found to be the less strained after the loading, while the small fragment remained strained, which "rose" the part of the distribution corresponding to the low crystallite size after the loading, in figure 2 in respect to the distribution before loading, in figure 1.

ACKNOWLEDGEMENTS

We fully acknowledge Drs. Dan Lupu and Alexandru Biris of I.T.I.M. Cluj-Napoca for their direct help and fruitful discussions.

REFERENCES

1. E. Storms, "Critical Review of the Cold Fusion Effect", Journal of Scientific Exploration 10, June1996.
2. J. F. Fernandez, F. Cuevas, M. Alguero, C. Sanchez, "Experimental Investigations of Neutron Emissions During Thermal Cycling of TiD_x" ($X \approx 2.00$), Fusion Technology 31, 237, 1997.
3. K. Yasui, "Fractofusion Mechanism", Fusion Technology 22, 400, 1992.
4. T. Takeda, T. Takizura, "Fractofusion Mechanism", J. of the Phys. Soc. of Japan, vol. 55, no. 9, 3073, 1989.
5. D. Chicea, D. Lupu, "About the random neutron emission from TiD_x samples", Romanian Reports in Physics No. 1-2, 1999.
6. D. Chicea, D. Lupu, I. Chereji, "Experimental Evidence of Neutron Emission from TiD_x Samples", Hadronic Journal Vol. 21, pg. 567-582, 1998.
7. N. Aldea, E. Indrea, "XRLINE, a Program to Evaluate the Crystallite Size of Supported Metal Catalysts by Single X-Ray Profile Fourier Analysis", Computer Physics Communications 60, 155-163, 1990.

STUDIA UNIVERSITATIS BABEŞ-BOLYAI, PHYSICA, XLIV, 1, 1999

OPTICAL PROPERTIES OF METALLIC NANOSTRUCTURES

S. ASTILEAN*

ABSTRACT. Numerical calculations show that metal transmission gratings of nanometric slits exhibit surprising high transmission efficiency. The transmission enhancement is a result of a resonant interaction of the incident light with surface plasmons, electronic excitations which are confined to the metal surface. The results indicate also a high level of sensitivity to the dielectric function of metal.

Introduction

In recent years the interest in the characterization and fabrication of nanostructured materials has grown constantly because of their distinctive properties and potential use in technological applications [1]. The grating nanostructures are a novel class of artificially fabricated diffractive structures that have the ability to control and manipulate the propagation of visible light [2]. The concept combines the rigorous (electromagnetic) diffraction theory with several lithographic techniques (electron-beam lithography) in order to produce high-quality periodic structures at nanometer-scale (50-500 nm). Properly designed periodic nanostructures with either dielectric and/or metallic materials are very attractive for a variety of applications in integrated optics, nonlinear optics and spectroscopy. Recently, several striking optical responses of such structures have been identified. For example, it was reported experimentally that cylindrical nanochannels, regularly perforated through optically-thick metallic films display unusually-high transmission spectra in the visible and near-infrared [3-4]. Because the light transmission is very efficient, such perforated metals films have a vast potential for applications and may constitute a novel basis for electro-optic devices for use in flat-panel displays, spatial light modulators, and tunable filters.

It is well known that all noble metals (Au, Ag, Cu) exhibit very strong linear and nonlinear optical response connected with excitation of surface plasmons when they are structured on the nanometer scale [5]. Motivated by this behavior and the results of Refs. [3,4], this paper is focused on the

* Optics and Spectroscopy Dept., Faculty of Physics, Babes-Bolyai University, 3400 Cluj-Napoca, Romania

examination of optical properties (light transmission, absorption and reflexion) in the near infrared region of the spectrum of several nanostructured metals. We will consider simple nanostructures, namely lamellar gratings made of Drude metals (noble metals) or metals for which the Drude model is not a good model (transition metals). The computational approach is based on the enhanced version of the Rigorous Coupled-Wave Analysis (RCWA), a versatile and efficient tool for modeling the diffraction of electromagnetic waves by periodic structures, especially when highly conductive metals are considered [6]. Our results obtained in the case of these simple nanostructures could serve as model for more complex metallic nanostructures and provide insights in photonic transport in mesoscopic and nanometric optical systems.

Theory

The model considered here is a freestanding, mono-periodic metallic structure consisting of spatially vacuum metal rods of rectangular cross section (see Fig. 1). The width of the gap (slit) between rods, the period and the thickness of the grating are *w*, Λ, and *d*, respectively. The grating is situated in the Oxy plane and extended along the Oz axis; its structural periodicity is only along the Ox axis. This metallic structure is illuminated at normal incidence by a plane electromagnetic wave of TM polarization (the magnetic-field vector is parallel to the metal rods and Oy axis). The wavelength is denoted by λ. As a response to the incident field, the grating will give rise to a diffracted field in the region above and below it and also a stationary field pattern inside it.

The RCWA is a versatile and efficient tool for describing the diffraction of electromagnetic waves in periodic structures. The relative permittivity $\varepsilon(x)$ in the grating region is a periodic function along the Ox direction and therefore can be expanded in a Fourier series of the form:

$$\varepsilon(x) = \sum_m \varepsilon_m \exp[\, jm(\frac{2\pi}{\Lambda})x] \tag{1}$$

where ε_m is the m-th Fourier component of the relative permittivity.

Because of periodicity along Ox axis, the electromagnetic fields inside the grating region (0<z<d) can be also expressed as a Fourier expansion of space-harmonic fields:

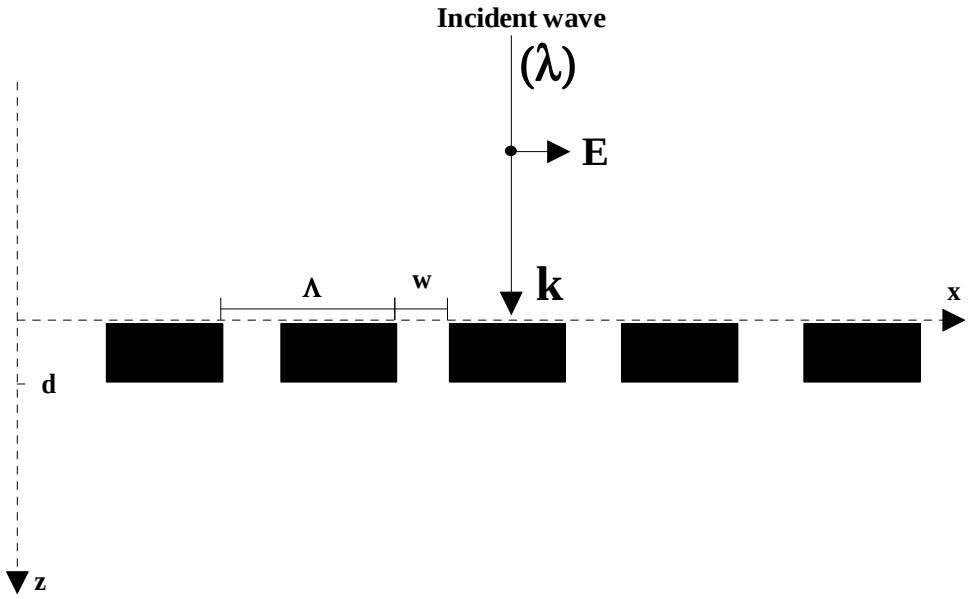

Fig. 1. Lamellar grating analyzed in this paper. The optical indices of the incident medium and of the substrate are equals to unity (vacuum). In the grating region, the relative permittivity is alternatively 1 (vacuum) or ε (metal).

$$H_y(x,z) = \sum_i U_{yi}(z)\,\exp(-jk_{xi}x) \qquad (2)$$

$$E_x(x,z) = j\left(\frac{\mu_0}{\varepsilon_0}\right)^{1/2} \sum S_{xi}(z)\,\exp(-jk_{xi}x)$$

where $U_{yi}(z)$ and $S_{xi}(z)$ are the normalized amplitudes of the i-th space-harmonic fields such that $H_y(x,z)$ and $E_x(x,z)$ satisfy Maxwell's equation in the grating region (near-field region).

Away from the grating (far-field region) the diffracted fields are taken as a superposition of plane waves (i.e. Rayleigh expansions):

$$H_y^1 = \exp(-j\frac{2\pi}{\lambda}z) + \sum_i R_i \exp[-j(k_{xi}x - k_{1,zi}z)] \quad in \ \ the \ \ input \ \ region \ z<0$$

$$H_y^2 = \sum_i T_i \exp[-j(k_{xi}x - k_{2,zi}(z-d))] \qquad in \ \ the \ \ output \ \ region \ z>d \tag{3}$$

where the projections k_{xi} of k-vector are given by the Floquet condition [6]: $k_{xi} = -i(2\pi/\Lambda)$ and the projections k_{zi} can be calculated from:

We noted by R_i the normalized magnetic-field amplitude of the i-th backward-diffracted wave and by T_i the normalized magnetic-field amplitude of the i-th forward-diffracted wave. Introducing the Fourier

$$k_{input,zi} = +\left(\sqrt{(\frac{2\pi}{\lambda})^2 - (k_{xi})^2}\right) \qquad if \qquad \frac{2\pi}{\lambda} > k_{xi}$$

$$k_{output,zi} = -j\left(\sqrt{k_{xi}^2 - (\frac{2\pi}{\lambda})^2}\right) \qquad if \qquad k_{xi} > \frac{2\pi}{\lambda} \tag{4}$$

expansions (Eq. 1 and Eq. 2) in the wave equation results a set of coupled-wave equations which alows to to represent the electromagnetic field inside the grating (amplitudes U and S) as a function of the eigenvectors and

$$S_i(z) = \sum_q C_q A_{q,i} \exp(B_q z) \tag{5}$$

eigenvalues of the coupled equation system:

where ($A_{q,i}$) and (B_q)are the eigenvectors and eigenvalues of the coupled equation system. Finally, the unknown coefficients (C_q) and the amplitude of reflected (R_i) and transmitted (T_i) waves are found by matching the electric and magnetic field components at the boundaries (z=0 and z=d).
The numerical implementation of the RCWA involves two steps: First, the eigenvalues and the eigenvectors of the matrix have to be computed and then a linear system of boundary equations has to be solved for finding R_i and T_i amplitudes. The diffraction efficiencies are defined:

where k_0 is the wave vector in vacuum ($2\pi/\lambda$).

The sum of the reflected and the transmitted diffraction efficiences given above must be unity for lossless gratings The dimension of the matrix associated with the eigenvalue problem is given by the number (N) of space harmonics taken to develop the field inside the grating. In order to get convergence, all propagating diffraction orders and a lot of evanescent waves have to be retained in the RCWA.
Recently, the RCWA has been revisited by several authors and an enormous increase in the convergence speed for the computation of grating efficiencies has been reported [7].

Results and discussion

We investigate the optical response of several nanostructured metals in the near infrared region (λ = 1.433 μm). Metals are nanostructured in the shape of the above transmission grating of fixed period (Λ=0.9 μm) and thickness (d=1.8 μm) and for a slit width varying between 0 and 100 nm. For the purpose of RCWA calculations the complex index of refraction of metals was interpolated from the values tabulated in Ref [8,9]. In order to rationalize our results, we also included a "lossless metal" modeled by a Drude free-electron dielectric function. The complex permitivities of metals at λ=1.433 μm are collected in Table 1.

Table 1 The complex permitivities ($\varepsilon = (n+ik)^2$) of metals at λ = 1.433 μm

Metal	n	k	Real(ε)=n2-k2	Im(ε)=2nk
Ag	0.133	10.381	-107.748	2.770
Au	0.446	9.797	-95.781	8.739
Cu	0.623	9.702	-93.755	12.090
Al	1.353	14.680	-213.642	39.727
Fe	3.560	5.297	-15.382	37.721
Ni	3.237	6.412	-30.635	41.517
W	2.80	4.51	-12.47	25.29
Pt	4.91	6.88	-23.24	67.57
Losless metal	0	3.77	-14.25	0

We mention that the periodic nanostructures under examination behaves as a 'zero-order' diffraction grating because all diffracted orders, other than zeroth forward-transmitted and backward-reflected order are evanescent waves. Therefore losses to metal associated with the imaginary part of the refractive index, physically manifested as carrier heating in the metal, can be extracted from RCWA calculations by the relation $A=1-\eta_{0,t}-\eta_{0,r}$, where $\eta_{0,t}$ and $\eta_{0,r}$ is the zero-order transmission and reflection efficiency, respectively. (The incident power to nanostructures is normalized to the unity).

(6)

$$\eta_i^{rreflection} = R_i \, R_i^* \, \mathrm{Re}(k_{zi}^{input} / k_0)$$

$$\eta_i^{transmission} = T_i \, T_i^* \, \mathrm{Re}(k_{zi}^{output} / k_0)$$

Optical responses of identical nanostructure made of different metals (Ag, Au, Cu, Al, Ni, Fe, Pt, and lossless metal) were evaluated by RCWA and the results are presented in Figures 2, 3 and 4. The light energy flow through gratings (Fig. 2) and the energy dissipation into metal (Fig. 3) undergoes strong modulation, contributing to dips in the reflected spectrum (Fig. 4). As in Ref [3], the absolute transmission efficiency calculated by dividing the grating transmission efficiency ($\eta_{0,t}$) to the grating transparency (w/Λ) is *greater than the unity* for several metals. In particular, silver gratings with slits of 32 nm width (that is 45 times much smaller than the wavelength!) transmit 10 times more light than directly impinging on the slits. While losseles metal can provide 100% transmission efficiency at a well-defined slit width (when all incident energy is channeled trough slits), silver metal shows a better transmission than other real metals. In principle, gratings made of Drude metal exhibit unusual transmittance peaks at well-defined slit dimensions.

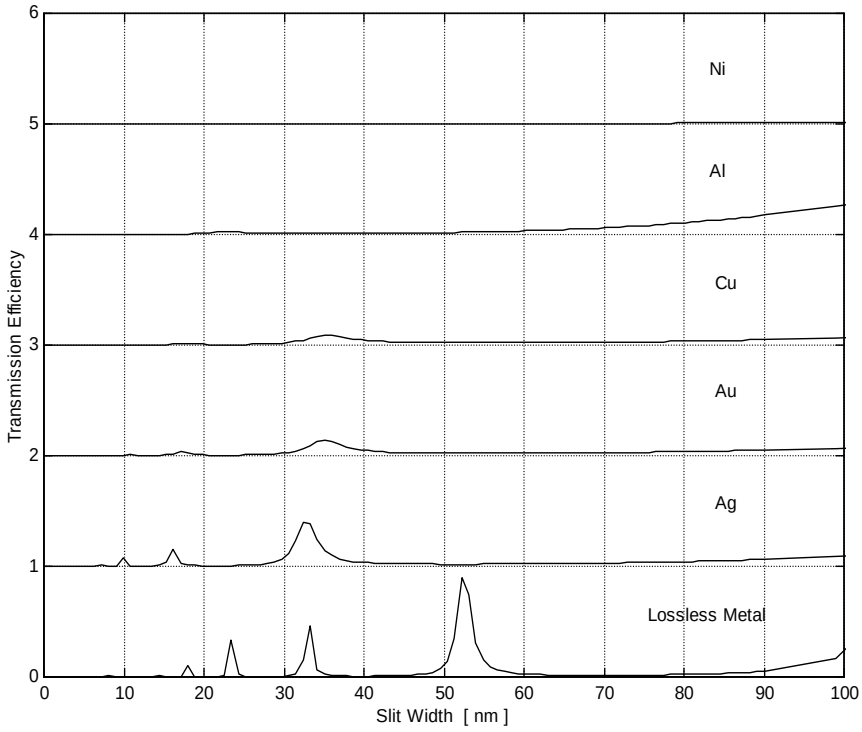

Fig. 2. Transmission efficiencies of grating nanostructures as a function of the slit width. The optical response is calculated for a grating of fixed period (Λ=0.9 μm) and thickness (d= 1.8 μm) when illuminated at normal incidence with light of λ= 1.433 μm wavelength and TM-polarization state. For the sake of clarity each curve is shifted up by +1 with respect to the previous one.

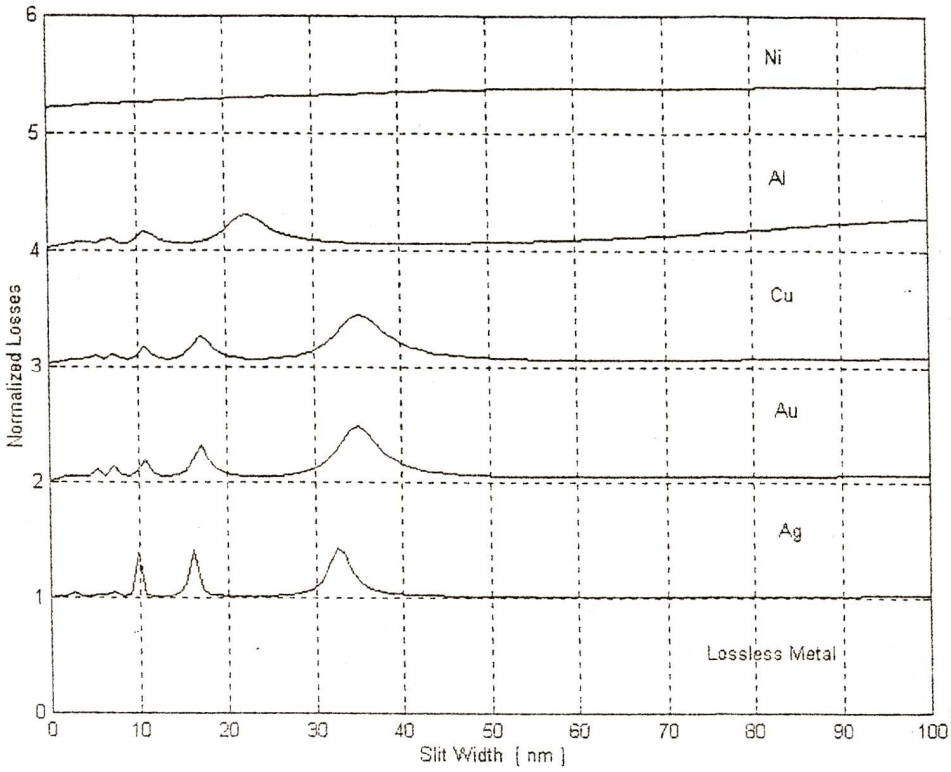

Fig. 3. Reflexion efficiencies of grating nanostructures as a function of the slit width. For the sake of clarity each curve is shifted up by +1 with respect to the previous one. (see also Figure 2)

Since the metals are highly reflective in the near infrared spectrum, one might expect that gratings of very narrow slits would have a high reflectance rather than a high transmittance. However, the results show that some metal nanostructures have a high transmittance rather than a high reflectance, even in the visible and near-infrared regions of the spectrum. Generally speaking, optical properties of classically opaque, metallic particles appear to be strongly dominated by near-field optical effects when they are are brought in close vicinity. These effects are linked to the surface plasmons exciation and the dielectric function of metal.

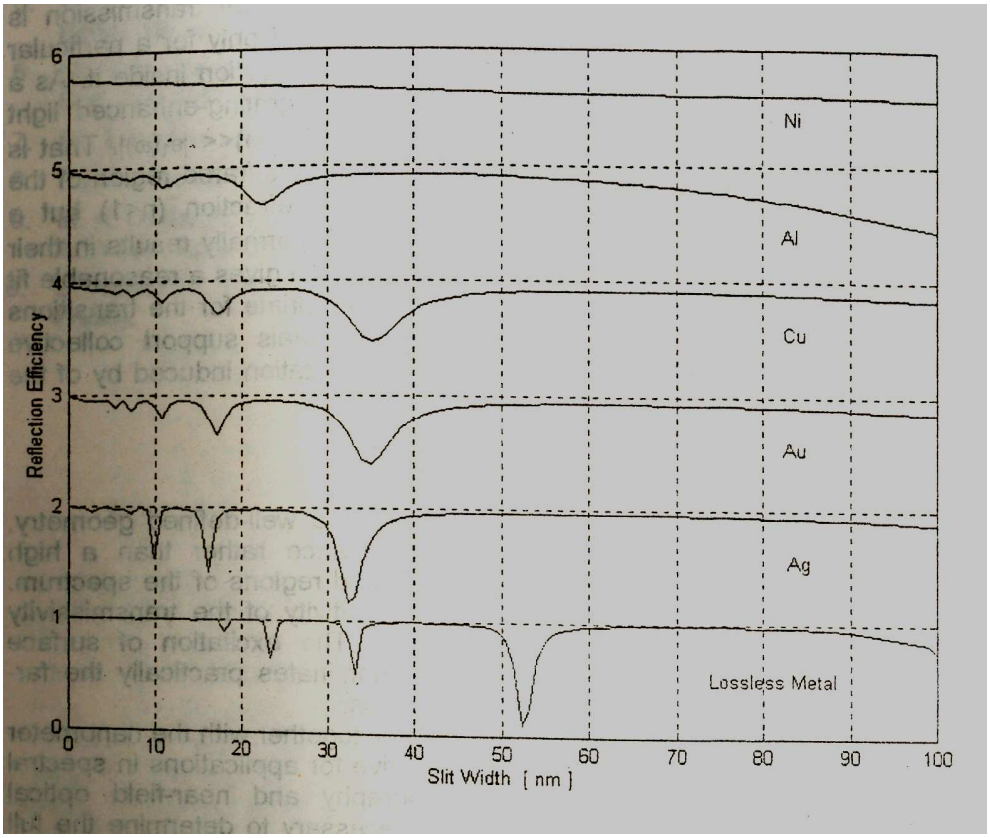

Fig.4. bsorption losses of grating nanostructures as a function of the slit width. For the sake of clarity each curve is shifted up by +1 with respect to the previous one. (see also Figure 2).

Surface plasmons are trapped electromagnetic waves, which propagate along metal surface and decay exponentially with distance away from the interface. In the case of metal transmission gratings when the gap between metal rods decreases, the surface waves begin to overlap and the resulting field can excite the fundamental mode supported by slits. We can interpret the origin of the extraordinary optical transmission as a strong interaction between on side, two surface plasmons counter-propagating along two metallic surfaces *in close vicinity* and on the other side, the fundamental mode supported by the cavity [10]. As a result, the collection

of light into the slit is favored and an unusual optical transmission is achieved. It is understood that this effect is observed only for a particular slit geometry which provides a particular field configuration inside it. As a result of our examination, a good metal favoring grating-enhanced light transmission is the metal exhibiting $\varepsilon_1(\omega) < -1$ and $\varepsilon_2(\omega) << |\varepsilon_1(\omega)|$. That is the case of Drude metals (see Table 1). In the near infrared region of the spectrum, noble metals have a small index of refraction ($n<1$) but a relatively large extinction coefficient ($k\approx10$), which normally results in their low dissipation ($nk<<1$). In general, the Drude model gives a reasonable fit to optical data for noble metals but it is not appropriate for the transitions metals. Contrary to noble metals, transition metals support collective surface excitations strongly modified by the polarization induced by of the core electrons (d electrons).

Conclusions

In conclusion, our results predict that in a well-defined geometry, metallic nanostructures exhibit high transmittance rather than a high reflectance, even in the visible and near-infrared regions of the spectrum. The results indicate also a high level of sensitivity of the transmissivity property to the dielectric function of metal. The excitation of surface plasmons and other near-field interactions dominates practically the far-field optical properties of metallic nanostructures.

The very high transmission efficiencies, together with the nanometer resolution, make such structures very attractive for applications in spectral filtering with metallic meshes, nanolithography and near-field optical microscopy. Further investigations will be necessary to determine the full potential of this phenomenon and its relation with spectroscopy of metallic nanostructures.

REFERENCES

1. A. S. Edelstein and R. C. Cammarata (Eds), *Nanomaterials: Synthesis, Properties and Applications*, Inst. of Phys. Publ. (1997).
2. S. Astilean, Ph. Lalanne, P. Chavel, E. Cambril. and H. Launois, Opt. Lett. 23, 552 (1998).
3. T. W. Ebbesen, H. J. Lezec, H. F. Ghaemi, T. Thio, and P. A. Wolff, Nature 391, 667 (1998).
4. H. F. Ghaemi, T. Thio, D. E. Grupp, T. W. Ebbesen and H. J. Lezec, Phys. Rev. B 58, 6779 (1998).

5. U. Kreibig and M Vollmer, *Optical Properties of Metal Clusters* (Springer, Berlin, 1995).
6. M. G. Moharam, E. B. Grann, D. A. Pommet, and T. K. Gaylord, J. Opt. Soc. Am. A 12, 1068 (1995).
7. Ph. Lalanne and G. M. Morris, J. Opt. Soc. Am. A 13, 779 (1996).
8. P.B.Johnson and R.W.Christy, Phys.Rev.B 6, 4370 (1972).
9. M. A. Ordal, L. L. Long, R. J. Bell, S. E. Bell, R. W. Alexander Jr, and C. A. Ward, Appl. Optics, Vol 22, 1099 (1983).
10. S. Astilean, Ph. Lalanne and M. Palamaru, submitted to Europhys. Lett. (1999).

STUDIA UNIVERSITATIS BABEŞ-BOLYAI, PHYSICA, XLIV, 1, 1999

PRELIMINARY EVALUATION OF THE CORRELATION TIME OF LOCAL DYNAMICS IN SOME POLYBUTADIENES

M. TODICA*

ABSTRACT. The correlation time of the local dynamics in molten and cross-link polybutadienes was calculated from the proton spin-lattice relaxation data, using the model of the passage of a particle over a barrier energy potential. The local dynamics is affected by the presence of molecules of CCl_4 in the vicinity of the polymeric chain also in the case of molten and cross-link polymer.

Introduction

Molecular dynamics in the polymeric materials is a complex process which include many kinds of motions, like the motions of chemical bonds inside the monomeric unit, the motion of polymeric segments which includes few monomers, or the diffusion of the entire chain, [1, 2]. Every description of this dynamics must be based on the knowledge of the local dynamics of polymeric links. This dynamics can be affected by presence of solvent molecules in the vicinity of the polymeric segments, or by the existence of temporary or permanent junctions between different chains, [3].

The aim of our study is to evaluate the correlation time of these local motions in molten, cross-link and some solutions of polybutadienes, using the NMR method.

Experimental

Our polymer of interest was the polybutadiene PB1009 with the microstructure 8% vinyl and 38% "cis". The molecular mass is 70 000 g/mole, the glass transition temperature T_g=175K and the density d=0.898 g/cm^3. We studied also the solution polybutadiene-CCl_4 with the concentration 80%, (PB80%) and the vulcanised polymer, NFA100%, with 1% sulphur. The vulcanised polymer was studded also in gonfled state with CCl_4.

*"Babes-Bolyai" University, Faculty of Physics, 3400 Cluj-Napoca, Romania.

The polymeric samples were supplied by the "Manufacture Michelin", France. The samples were enclosed in NMR tubes (diameter 4mm) and sealed under a primary vacuum. All the measurements were performed using a CXP Bruker spectrometer working at 45 MHz, in the temperature range of 254 K to 344K. The spin-lattice relaxation time was measured using the "inversion recovery" method, [4]. The samples temperature was controlled within 1 K.

Results and discussion

The most important motions involving the polymeric chains, which are clearly separated in the space and time scale, are the long range fluctuations or slow motions, and the high frequency motions or local fluctuations.

The first ones are associated with the diffusion of the entire chain along the "reptation tube", correspond to the low frequency motions and are characterised by long correlation time. These kinds of motions are strongly dependent on the molecular mass of the polymeric chains and are influenced by the existence of temporary or permanent junctions between different polymeric chains, [5]. Temporary junctions exist also in molten or polymeric solutions and they are determined by the swelling of different chains. The time life of these junctions is affected by the temperature and the solvent concentration in the case of polymeric solution. Increasing of the temperature or solvent concentration diminish the time life of these junctions. Viscoelastic behaviour of the polymeric materials is mainly determined by the existence of the temporary junctions.

The permanent junctions appears when chemical links between two different polymeric chains are established by the intermediate of one additional atom which do not appertain of the chain. Vulcanisation with sulphur is one of the most used method to generate permanent junctions in polymeric materials. Generally the time life of the permanent junctions are weakly affected by the temperature or solvent concentration. Increasing of temperature amplifies the magnitude of the segmental motion between two junctions, but only high thermal energies can destroyed these chemical links. The existence of the permanent junctions is associated with the rigidity of the polymeric materials. Generally the temporary or permanent junctions affects the long range dynamics of the chains. The local dynamics of the polymeric segments is affected by the temporary or permanent junctions only if the density of these junctions are enough high, so that the length between two junction be comparable with the size of few monomers.

The high frequency motions involves the polymeric segments, which includes one or few monomers and are characterised by short correlation time. These motions are not dependent on the molecular mass of the chain but are affected by the presence of solvent molecules in the vicinity of polymeric chains.

The modification of the local dynamics of polymeric segments, determined by the existence of temporary or permanent junctions or by the presence of solvent molecules, is reflected by the modification of the correlation time of the rotation motions of the polymeric segments. Every rotation of the C-C and C-H bonds modifies the relative orientation of the atoms attached to the chains, and thus the relative orientation of the nuclear spins. The dominant mechanism which governs the spin-lattice relaxation process of the protons attached to the polymeric chain is the dipolar interaction between the nuclear spins located within one given chain segment. This interaction decreases rapidly with the distance between the spins, so that only the neighbouring spins are taken into account, [6].

For identical nucleus, the spin-lattice relaxation rate is given by the relation:

$$\frac{1}{T_1} = K\left[\frac{\tau_c}{1+\omega^2\tau_c{}^2} + \frac{4\tau_c}{1+4\omega^2\tau_c{}^2}\right] \tag{1}$$

K is one parameter depending on the distance between the interacting spins, ω is the resonance frequency of the protons and τ_c is the correlation time of the orrientational motion of the spins. The mathematically expression for τ_c is derived on the basis of the specific model for the polymeric dynamics. One of the most used model is based on the passage of a particle over a barrier energy potential, [7,8]. In this case the correlation time is given by the expression:

$$\tau_c = B\exp\left(\frac{E_a}{RT}\right) \tag{2}$$

B is one parameter depending on the nature of the polymer and E_a is the activation energy required for the passage over the potential barrier.

Combining the relation (1) and (2) we can obtain the temperature dependence of the spin lattice relaxation rate.

Two situation are of great interest: the extreme narrowing condition $\omega\tau_c << 1$, and the minimum relaxation time condition $\omega\tau_c \approx 0.616$, (2*). In the first case the relation (1) simplify to:

$$\frac{1}{T_1} \propto \exp\left(\frac{E_a}{RT}\right) \tag{3}$$

This relation allow us to calculate the activation energy from the slope of the plot ln(T_1) versus 1/ T_1.

In the second case we obtain a direct relation between the minimum relaxation time $T_{1\min}$ and the parameter K. For the Larmor frequency ω=45 Mhz, we obtained the relation:

$$\frac{1}{T_{1\min}} = K \cdot 5.035 \cdot 10^{-9}(s) \tag{4}$$

When the activation energy E_a and the parameter K are knows, then the parameter B of equation (2) can be evaluated from the best fit of the experimental data T_1(T). Knowing the value of B we can estimate the correlation time at any temperature using the equation (2).

The minimum of the spin-lattice relaxation time was observed for a characteristic temperature θ(φ) for the samples PB100%, PB80% and NFA100% in the domain of 244 to 344K (fig.1). For the sample NFA gonfled in the CCl_4 we not observed this minimum, but we estimated (by extrapolation) that this minimum will correspond to the temperature θ=220K and will have the value $T_{1\min}$=62ms.

If we utilise the equation (2*) we can calculate, for each sample, the correlation time of the local dynamics of polymeric segments corresponding to the temperatures θ(φ). We found the values τ_c(θ)=2.17*10^{-9} ±5% s.

We observed also that the curves T_1(T) for the molten and the cross-link polybutadienes are very close each other. This result is not surprising because the two samples contain polymeric chains with the same molecular mass and the same microstructure. The only difference is the existence of the sulphur links between the chains of the second sample. This behaviour shows that little concentration of permanent cross-links, (1%), between the polymeric chains do not affect the local dynamics of the chain.

On the other hand we observed some differences between the curve T_1(T) for the molten polymer and for its solution. That means that the presence of the solvent molecule in the vicinity of the polymeric chains affects the local dynamics of the polymer.

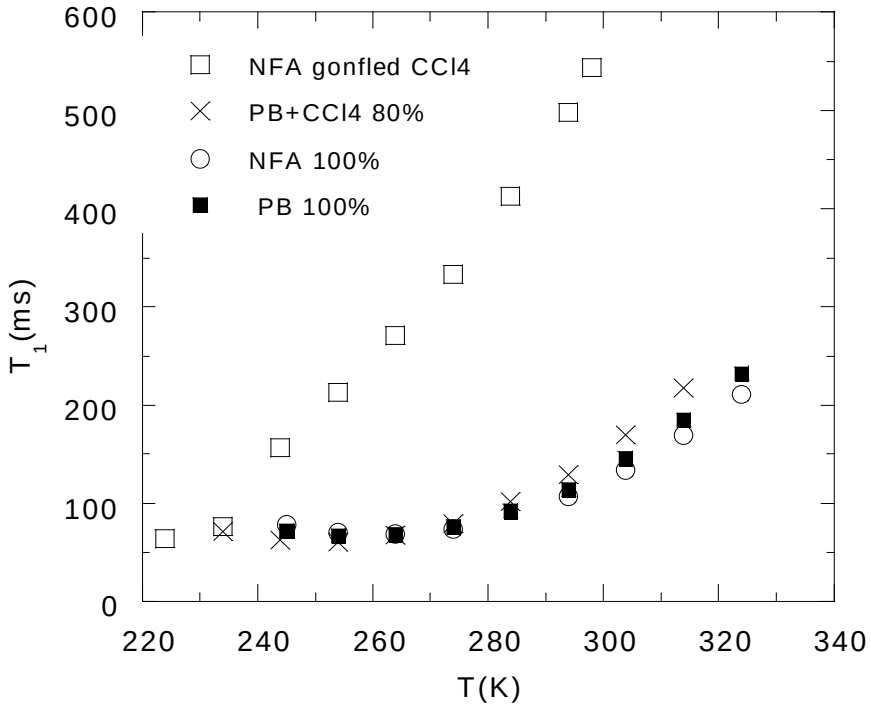

Fig. 1. Temperature dependence of the spin-lattice relaxation time.

The extreme narrowing condition $\omega\tau_c << 1$ is fulfilled for the temperatures higher then $\theta(\varphi)$. For each sample, we calculated the activation energy E_a from the Arrhenius plot of $\ln(T_1)$ versus 1/ T, (fig.2).

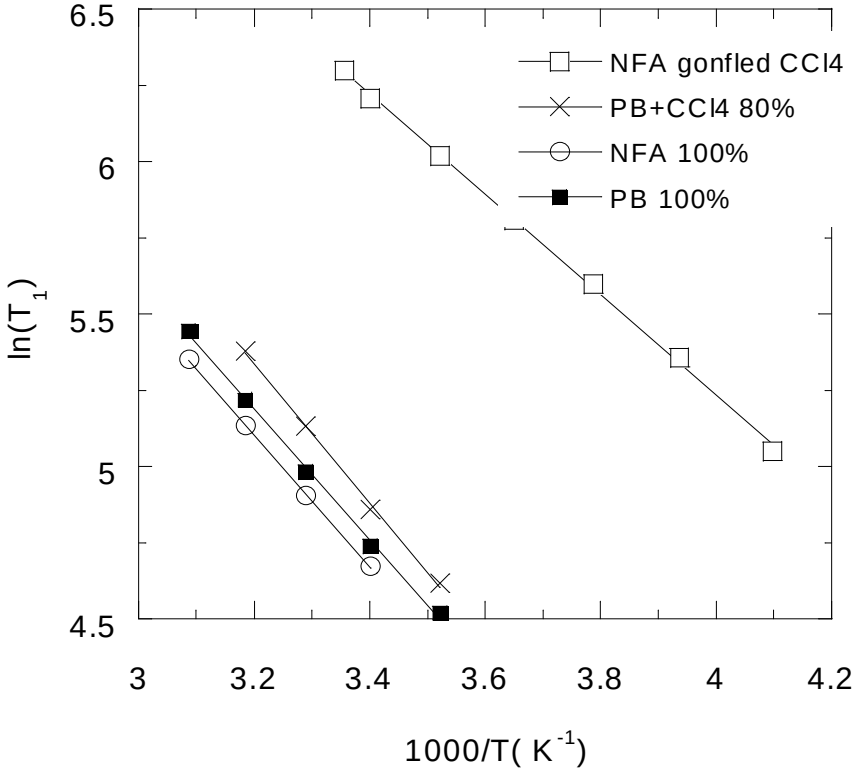

Fig. 2. Arrhenius plot of experimental data $T_1(T)$.

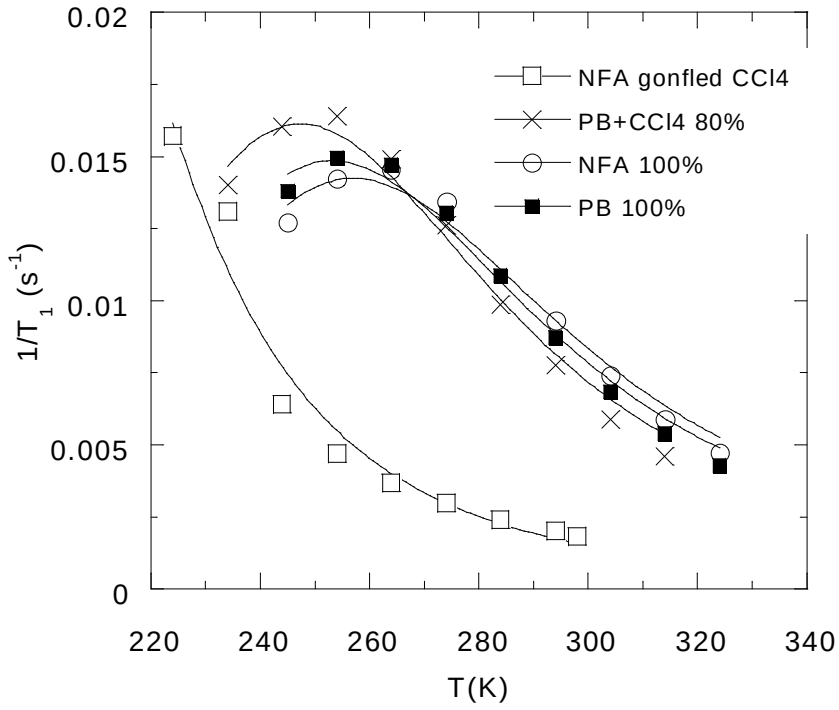

Fig. 3. The best fit of the experimental data $1/T_1(T)$ with the equation (1).

The values of activation energy are very closed each other for the molten and cross-link polybutadiene, E_a=17.8%±5%Kj/mole, and E_a=17.9%±5%Kj/mole respectively, but they are higher then the values obtained for the solution and gonfled cross-link polymer, E_a=17.45%±5%Kj/mole and respectively E_a=16.4%±5%Kj/mole. This behaviour indicates also the effect of the solvent on the dynamics of the polymeric segments.

For each sample we calculated the parameter K from the minimum values of T_1 using eq. (4). Then we used these values of the constant K to fit the experimental data $T_1(T)$ using eq. (1). In this fit B is an adjustable parameter. The values of E_a, K and B are listed in the table 1.

Table 1

Samples	Ea [Kj/mole]	K	B
PB 100%	17.8	$3.0*10^{9}$	$4.49*10^{-13}$
PB 80%	17.45	$3.3*10^{9}$	$4.24*10^{-13}$
NFA 100%	17.92	$2.9*10^{9}$	$4.83*10^{-13}$
NFA gonfled	16.4	$3.2*10^{9}$	$1.71*10^{-12}$

In the first order of approximation the fit is satisfactory for all the samples, especially in the domain of higher temperatures, (fig. 3). However deviations of the fit were observed in the domain of lower temperatures. This result is not surprising because the constant parameters of the fit, E_a and K, were determined in the domain of high temperatures. On the other hand, these results shows that the simplest model of the passage of a particle over a barrier energy potential is applicable to the polymeric materials only for preliminary investigations of the local segmental dynamics. More precisely investigations can be done by the use of specific model for each polymer, [9].

Using the values of parameters K and B obtained by this way, we generated with equation (2), the correlation time at any temperature. For all the samples the correlation time decreases rapidly with the temperature, which indicate an increasing of the local mobility of the polymeric chains, (fig. 4). The values of τ_C for the molten and cross-link polybutadienes are practically identically in the whole range of temperatures, only little differences being observed for low temperatures. This means that low degree of vulcanisation do not affect essentially the local dynamics of the cross-link polymer by rapport of the molten polymer, [10].

Important differences were observed in the domain of low temperatures between the correlation time of the molten polymer and its solution and between the molten polymer and the gonfled cross-link polymer. However, in the domain of high temperatures the differences between the values of τ_C for all the samples diminish. We can assume that the local dynamics of the polymeric chain is more affected by the specific local environment of the chain in the domain of low temperatures than in the case of higher temperature.

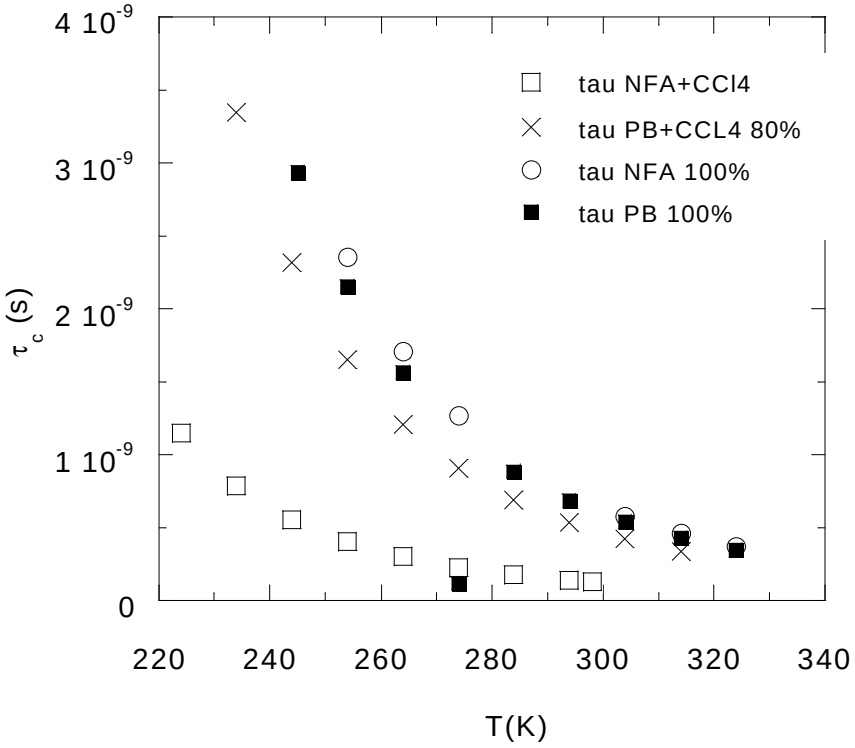

Fig. 4. The values of the correlation time generated with the equation 2.

Equation (2) allows us also to calculate the correlation time corresponding to the temperatures $\theta(\varphi)$ for which the spin-lattice relaxation time reach its minimum. The values obtained with the equations (2) and (2*) are so closed each to others, which indicate that the two ways for the evaluation of τ_C are in satisfactory agreement. Important differences appear only in the case of the gonfled cross-link polymer at low temperatures. It is clear that our model (used for the evaluation of the τ_C) can give good results for all the samples only in a restraint domain situated in the range of higher temperatures.

CONCLUSION

The analyse of the proton spin-lattice relaxation data using the model of the passage of a particle over a barrier energy potential provide goods results to evaluate the correlation time of the local dynamics in some polybutadienes. The values obtained for the molten and cross-link polymer are very closes each to others. This fact indicate that low degree of vulcanisation with sulphur do not affect dramatically the local dynamics of polymeric segments.

The presence of molecules of CCl_4 in the vicinity of the chains increases the local dynamics of the macromolecules, also in the solutions or in the case of cross-link polymer.

REFERENCES

1. P. G. De Gennes, Scaling concepts in polymers physics, Cornell University Press, Ithaca, New-York, 1979.
2. J. D. Ferry, Viscoelasticity of Polymers, Third edition, New York, John Wiley and Sons, 1980
3. J. P. Cohen-Addad, Physical properties of polymeric gels, John Wiley and sons, Chicester, New-York, Toronto, 1996.
4. H. Y. Carr, E. R. Purcell, Phys. Rev., 1954, 94, 630
5. J. P. Cohen-Addad, NMR and fractal properties of polymeric liquids and gels, Pergamon Press, London, 1992.
6. A. Abragam, The Principles of Nuclear Magnetism, Clarendon Press, Oxford, 1961
7. H. A. Kramers, Physica, 1940, 7, 284
8. E. Helfand, J. Chem. Phys., 1971, 54, 4651.
9. Dejan de la Batie, F. Laupretre, L. Monneire, Macromolecules, 22, 122, 1989.
10. M. Todica, J. P. Cohen-Addad, A. V. Pop, G. Damian, Studia Univ. Babes-Bolyai, Physica, XL, 1, 1995.

STUDIA UNIVERSITATIS BABEŞ-BOLYAI, PHYSICA, XLIV, 1, 1999

METHOD FOR PRELIMINARY ANALYSE OF THE SPIN-LATTICE NMR RELAXATION TIME IN SOME POLYMETRIC MATERIAL

M. TODICA*, I. BURDA*

ABSTRACT. A method for preliminary evaluation of the correlation time of local dynamics of some polymeric materials, using the experimental NMR spin-lattice relaxation data, is proposed. The algorithm is based on the model of the passage of a particle over a barrier energy potential. This method was tested for some molten polymers and polymeric concentrated solutions.

Introduction

The molecular dynamics in the polymeric materials is a complex process which include many kinds of motions, but the elementary motions which governs the whole dynamics of the polymeric chains are the elementary motions of the polymeric segments. The knowledge of the correlation time of these motions is an important step to characterise the local dynamics of the macromolecules, [1]. In this work is presented a method for preliminary evaluation of this parameter from NMR spin-lattice relaxation data. The method is based on the model of the passage of a particle over a energy barrier potential, [2, 3]. This method was applied to some molten polymers and concentrated polymeric solutions.

* "Babes-Bolyai" University, Faculty of Physics, 3400 Cluj-Napoca, Romania.

Experimental

We studded some linear polymers:

-the polybutadiene PB1507, (PB-100%), with the microstructure 40% vinyl and 24% "cis" and the molecular mass 190 000 g/mole

-the polyisoprene IR307, (IR-100%), with the conformation of 92% "cis";

-the vulcanised polybutadiene NFA 1, with 1% sulphur, with the microstructure 8% vinyl and 38% "cis", and the molecular mass 120 000 g/mole; We studded also the solutions PB1507-CCl4 with the concentration 86%, (PB-86%) and 74% (PB-74%).

The polymeric samples were supplied by the "Manufacture Michelin", France. The samples were enclosed in NMR tubes (diameter 4mm) and sealed under a primary vacuum. All the measurements were performed using a "CXP Bruker" spectrometer working at 45 MHz, in the temperature range of 254 K to 344K. The samples temperature was controlled within 1 K. The spin-lattice relaxation time was measured using the "inversion recovery" method, [4].

Results and discussion

The most important motions which governs the dynamics of the entire chain are the local rotations of the polymeric links. Every rotation of the C-C and C-H bonds modifies the relative orientation of the atoms attached to the chains, and thus the relative orientation of the nuclear spins. The dominant mechanism which governs the spin-lattice relaxation process of the protons attached to the polymeric chain is the dipolar interaction between the nuclear spins located within one given chain segment, [5]. This interaction decreases rapidly with the distance between the spins, so that only the neighbouring spins are taken into account, [6].

For identical nucleus, the spin-lattice relaxation rate is given by the relation:

$$\frac{1}{T_1} = K\left[\frac{\tau_c}{1+\omega^2\tau_c{}^2} + \frac{4\tau_c}{1+4\omega^2\tau_c{}^2}\right] \qquad (1)$$

K is one parameter depending on the distance between the interacting spins, ω is the resonance frequency of the protons and τ_c is the correlation time of the orientational motion of the spins. The mathematically expression for τ_c is derived on the basis of the specific model for the polymeric dynamics. One of the most used model is based on the passage of a particle over a barrier energy potential, [2,3]. In this case the correlation time is given by the expression:

$$\tau_c = B \exp\left(\frac{E_a}{RT}\right) \tag{2}$$

B is one parameter depending on the nature of the polymer and E_a is the activation energy required for the passage of a particle over the potential barrier. We used this model for preliminary evaluation of the correlation time in some polymeric materials.

Combining the relation (1) and (2) we can obtain the temperature dependence of the spin lattice relaxation rate. This relation contains three unknowns parameters, K, B and E_a. If we fit the experimental T1(T) data, using common computing algorithm, like the least mean square method, it is possible to obtain values of these parameters without physical relevance. Our interest is to reduce the number of the unknown parameters in the fit, or to find a methods to attribute real physical values for these parameters. To do this, two situation are of great interest:

-the extreme narrowing limit, $\omega\tau_c << 1$ and

-the minimum of the spin-lattice relaxation time,

In the first case, the relation (1) simplify to:

$$\frac{1}{T_1} \propto \exp\left(\frac{E_a}{RT}\right) \tag{3}$$

This relation allow us to calculate the activation energy from the slope of the plot ln (T_1)versus $1/T_1$.

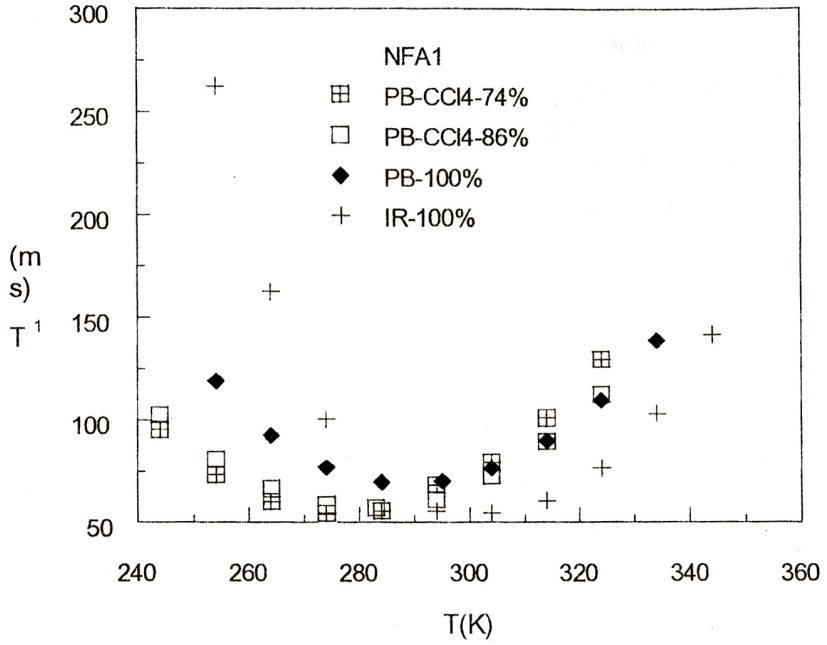

Fig. 1. Temperature dependence of the spin-lattice relaxation time.

In the second case we utilise the condition of the minimum of the T1(T) function,

$$\frac{\partial T_1}{\partial T} = 0$$

From equation (1), we obtain the simplest relation at the minimum of the spin-lattice relaxation minimum:

$$\omega\tau_c \approx 0.616 \qquad (4)$$

Using the equation (4) we can obtain a direct relation between the minimum relaxation time T_{1min} and the parameter K. For the Larmor frequency ω=45 Mhz, we obtained the relation:

$$\frac{1}{T_{1\,\min}} = K \cdot 5.035 \cdot 10^{-9}(s) \qquad (5)$$

These two particularly situations allows us to estimate two of three parameters of relations (1) and (2). To can profit of these situations, it is necessary to record the experimental T1 data in a large domain of temperatures, including also the minimum of the spin-lattice relaxation time and temperatures far for this minimum.

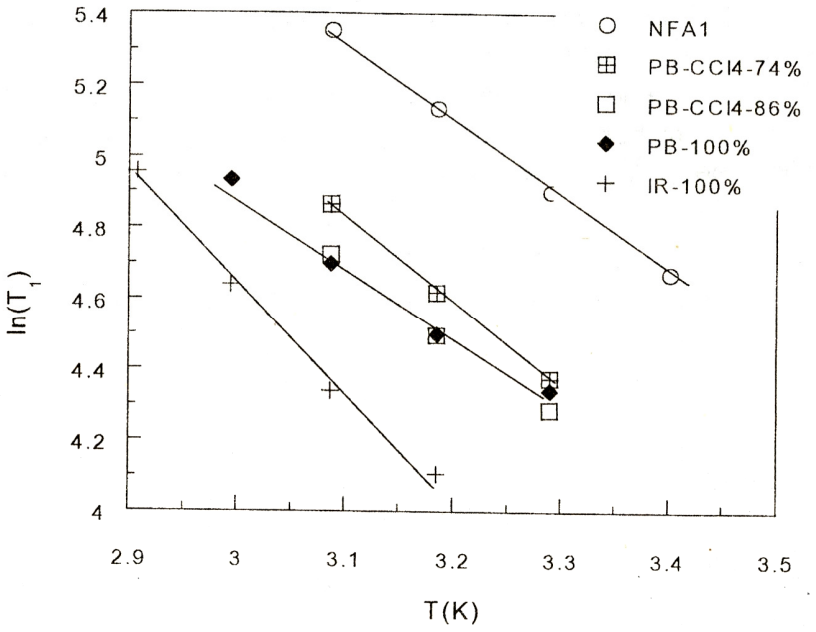

Fig. 2. Arrhenius plot of experimental data $T_{1(T)}$.

When the activation energy E_a and the parameter K are knows, then the parameter B of equation (2) can be evaluated from the best fit of the experimental data $T_{1(T)}$. Knowing the value of B we can estimate the correlation time at any temperature using the equation (2).

For all the samples the spin-lattice relaxation time was measured in a large domain of temperatures, including the two situation. The minimum of the relaxation time was observed for each sample for a characteristic temperature $\theta(\varphi)$ in the domain of 244 to 344 K, (fig.1). Using the relation (5) we can calculate the parameter K for each sample. The values of K are listed in the Table 1. If we utilise the equation (4) we can calculate directly,

for each sample, the correlation time of the local dinamics of polymetric segments corresponding to the temperatures $\theta(\varphi)$. It is important to retain that the relation (4) give the correlation time only for a single temperature, $\theta(\varphi)$. We found the values τ_c $(\theta)=2.17^{*}10^{-9}$ $\pm 5\%$ s. We will utilise these values of τ_c to test the validity of our method, after the evaluation of all τ_c. For other temperatures the correlation time must be calculate with the relation (2). The parameter B is determined from the fit of the all experimental $T_{1(T)}$ data.

The extreme narrowing condition $\omega\tau_c << 1$ is fulfilled for the temperatures higher then $\theta(\varphi)$. For each sample, we calculated the activation energy E_a from the Arrhenius plot of ln(T1) versus 1/T, (fig. 2).

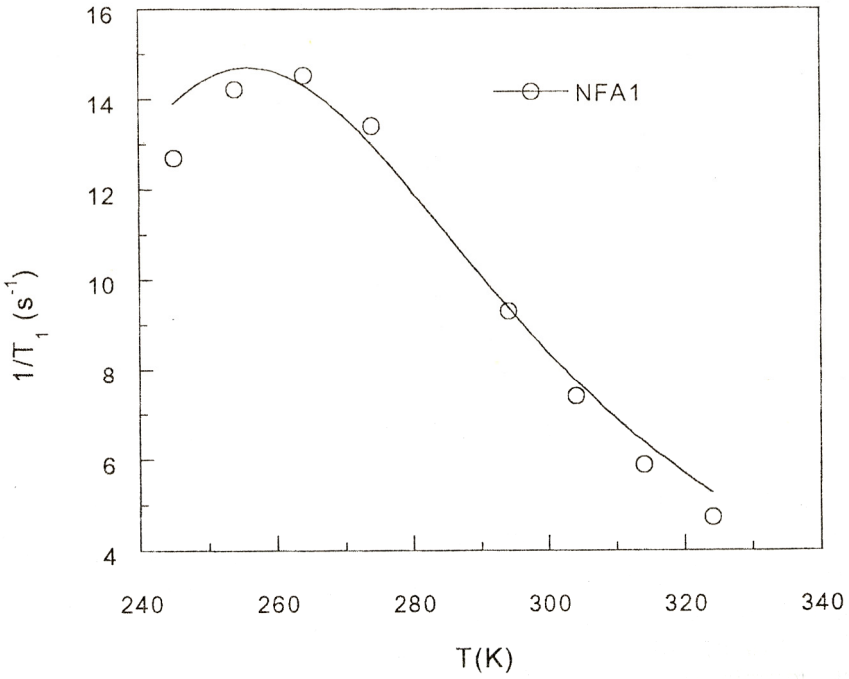

Fig. 3. The best fit of the experimental data $1/T_1(T)$ for the sample NFA 1, using the equation (1).

Then we used these values of E_a and K to fit the experimental data $T_{1(T)}$ using eq. (1). In this fit B is an adjustable parameter. The values of E_a, K and B are listed also in the table 1.

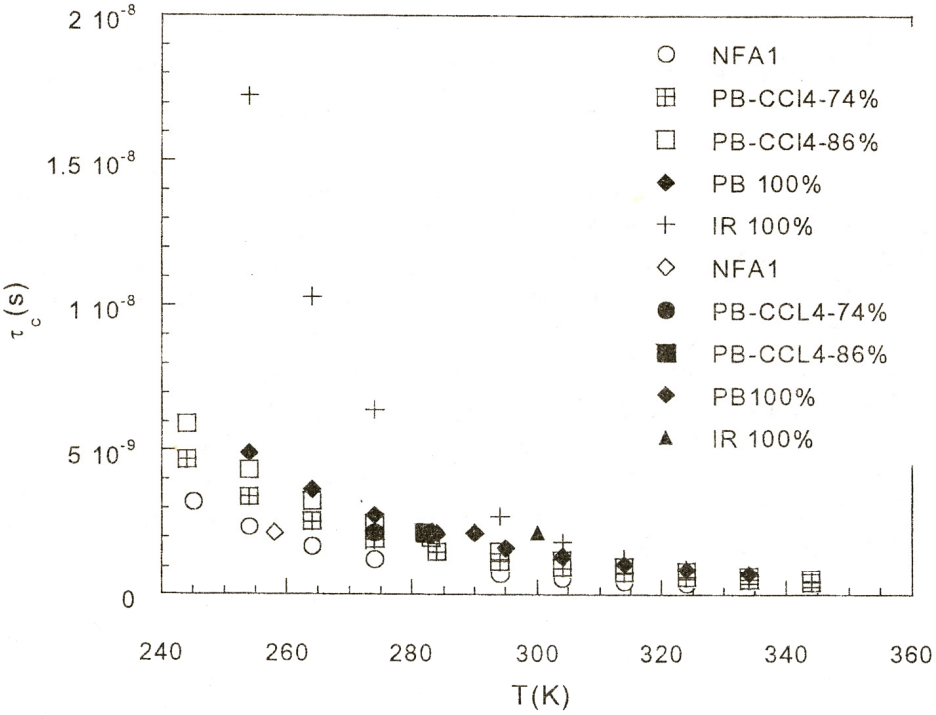

Fig. 4. The values of the correlation time generated with the equation 2. The next symbols (✧, ●, ■, ◆, ▲). represents the values of correlation time obtained with the equation 4.

Table 1

Samples	Ea [Kj/mole]	K	B
PB 100%	18.8	$2.9^{*}10^{9}$	$7.73^{*}10^{-13}$
PB 86%	16	$3.5^{*}10^{9}$	$2.03^{*}10^{-12}$
PB 74%	16	$3.7^{*}10^{9}$	$1.45^{*}10^{-12}$
NFA 1	17.9	$2.9^{*}10^{9}$	$4.83^{*}10^{-13}$
IR 100%	28.5	$3.4^{*}10^{9}$	$2.93^{*}10^{-14}$

In the first order of approximation the fit is satisfactory for all the samples, especially in the domain of higher temperatures. For example the figure 3 shows the fit of the experimentaldata for the sample NFA-1. However deviations of the fit were observed in the domain of lower temperatures. This result is not surprising because the constant parameters of the fit, E_a and K, were determined in the domain of higher temperatures. On the other hand, these results shows that the simplest model of the passage of a particle over a barrier energy potential is applicable to the polymeric materials only for preliminary investigations of the local segmental dynamics. More precisely investigations can be done by the use of specific model for each polymer, [7].

Using the values of parameters K and B obtained by this way, we generated with equation (2), the correlation time at any temperature, also for the temperatures $\theta(\varphi)$. The values of τ_c obtained directly bu the use of equation (4) and by the equation (2), are in satisfactorily accord, (fig. 4). We observed also that the correlation time decreases rapidly with the temperature, for all the samples, which indicate an increasing of the local mobility of the polymeric chains, (fig. 4). This behaviour is in accord with the general behaviour of the polymeric materials.

CONCLUSION

Evaluation of the correlation time of the polymeric segments can be done from the NMR experiments, when the experimental T1 data are recorded in a large domain of temperatures, including also the minimum of the relaxation time and the extreme narrowing limit. The model of the passage of a particle over a barrier energy potential can be used for preliminary evaluations of the correlation time of the local dynamics in some polymeric materials.

REFERENCES

1. P. G. De Gennes, Scaling concepts in polymers physics, Cornell University Press, Ithaca, New-York, 1979.
2. H. A. Kramers, Physica, 1940, 7, 284
3. E. Helfand, J. Chem. Phys., 1971, 54, 4651.
4. H. Y. Carr, E. R. Purcell, Phys. Rev., 1954, 94, 630
5. J. P. Cohen-Addad, NMR and fractal properties of polymeric liquids and gels, Pergamon Press, London, 1992.
6. A. Abragam, The Principles of Nuclear Magnetism, Clarendon Press, Oxford, 1961
7. Dejan de la Batie, F. Laupretre, L. Monneire, Macromolecules, 22, 122, 1989.

STUDIA UNIVERSITATIS BABEŞ-BOLYAI, PHYSICA, XLIV, 1, 1999

CUBIC U(IV)-ION ENVIRONMENT IN $K_{19}[U_2KAs_4W_{40}O_{140}]\cdot 42H_2O$ POLYOXOMETALATE COMPLEX

C. CRĂCIUN*, L. DAVID*, M. RUSU, O. COZAR*, C.BĂLAN*, D.RISTOIU***

ABSTRACT. The polyoxometalate $K_{19}[U_2KAs_4W_{40}O_{140}]\cdot 42H_2O$ complex was investigated by IR and ESR spectroscopy. IR spectrum of the uranium(IV)-complex contains an additional band at ≈1133 cm^{-1} assigned to the ν_{as}(U-O) vibration and presents changes of bicentric (ν_{as}(W=O_d), ν_{as}(W-O_a)) and tricentric (ν_{as}(W-O_c-W), ν_{as}(W-O_b-W)) bands comparative with the IR spectrum of the ligand, owing to the uranium coordination at four terminal O_d atoms from the {AsW_9} units and four O_d atoms from WO_6 binding octahedra. ESR spectra at room and nitrogen liquid temperatures correspond to a triplet spin ground state (S_{eff}=1) of uranium(IV) ions. The values of fine structure (g_{z_1}=2.098, g_{y_1}=2.089, $g_{x_1} = g_{x_2}$=2.067, g_{y_2}=2.051, g_{z_2}=2.031) show a small orthorhombic distortion from the cubic symmetry.

Introduction

Polyoxometalates (POM) are molecular blocks of metal oxide formed by MO_6 octahedra (M=Mo, W, V…) sharing vertices or edges. The most general formulation for the POM is $[X_xM_mO_y]^{q-}$ (x<m) where X is the central heteroatom (X=P, Ge, As, Si…) and M is the addend atom [1]. In the last years, polyoxometalates and their metallic complexes have been intensely studied for the important applications in catalysis, biology and materials science [2].

The fundamental POM structure is the Keggin unit with 12 MO_6 octahedra arranged in four M_3O_{13} groups. If one M_3O_{13} group of the Keggin unit is removed (Fig.1), two or more such trilacunar units can form large and complicated structures.

* Department of Physics, Babeş-Bolyai University, 1 Kogalniceanu, 3400 Cluj-Napoca

** Department of Chemistry, Babeş-Bolyai University, 1 Kogalniceanu, 3400 Cluj-Napoca

Different metallic ions can coordinate the POM by entering into their lacunar structures. The MO_6 octahedra could contain four oxygen type atoms [2]: O_a atom binds the X heteroatom from the XO_4 tetrahedron and the M addends from the MO_6 octahedra; O_b atom binds two M addend atoms from two MO_6 octahedra sharing a corner; O_c atom binds two M atoms from two MO_6 octahedra sharing an edge; O_d is a terminal oxygen atom.

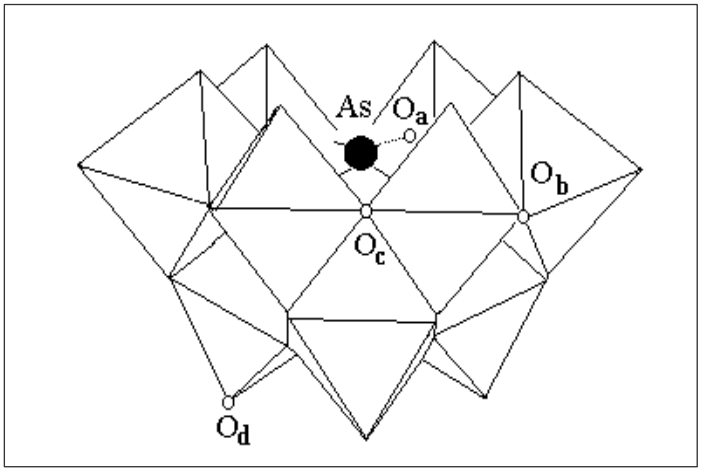

Fig.1. The fundamental trilacunar Keggin structure

In this report we are dealing with an uranium(IV) complex of $[KAs_4W_{40}O_{140}]^{27-}$ cryptate heteropolyanion (Fig.2). This POM contains four trilacunary $\{AsW_9\}$ Keggin units bound by four WO_6 octahedra [3].

Each Keggin unit has a tetrahedral AsO_4 core, surrounded by three W_3O_{13} configurations. The metallic complexes of $[KAs_4W_{40}O_{140}]^{27-}$ polyoxometalate presents five sites [4,5], one central cryptate site (K) in which one alkaline ion is eight coordinated and four other lacunary sites ($S_1 \div S_4$) which can be coordinated by different cation.

These last secondary sites are symmetrically placed two by two at the central cryptate site, without being in the same plane.

The flexibility of the structure allows an uranium cation to coordinate the active sites (S_1, S_2 or S_3, S_4), in spite of his important size and electrostatic charge [6]. Each Keggin unit have two O_d atoms from ($W=O_d$) bonding, towards the lacunar part, which could be involved in coordination at the uranium ions.

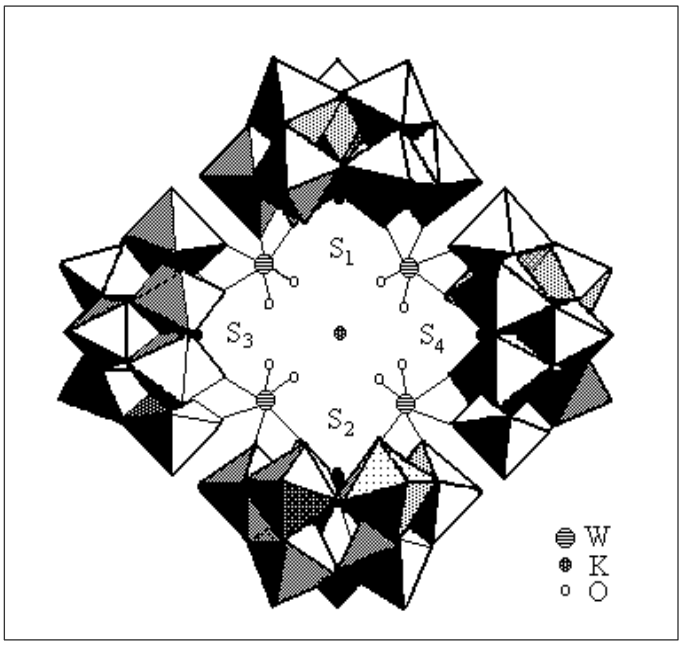

Fig.2. Structure of $[KAs_4W_{40}O_{140}]^{27-}$ cryptate heteropolyanion

Into the cavity of the criptand there are also eight terminal oxygen atoms from binding WO_6 octahedra, also active in the coordination process.

In order to obtain information on the local structure around the uranium(IV) ions, the $K_{19}[U_2KAs_4W_{40}O_{140}]\cdot 42H_2O$ complex was investigated by IR and ESR spectroscopy.

For the uranium (IV) ion ($5f^2$ configuration) in inorganic compounds, there are available two approximations, depending on the magnitudes of spin-orbit and metal-ligand interactions, respectively. If the two interactions are of the same magnitude and exhibit a dominant covalent character, the intermediate crystal field approximation is valid and the electrons are delocalized into the ligand orbital. The situation is alike the 3d ions complexes. Otherwise, if the metal-ligand interaction is much smaller than the spin-orbit coupling we talk about weak field-approximation in which the ground state has a purely metallic character and the electrons of U(IV) are more localized towards the uranium center [7]. In this case, the uranium(IV) ion behaves like the isoelectronic rare-earth ion Pr^{3+} ($4f^2$ configuration).

Experimental

IR spectra were obtained in KBr pellets in the range 4000÷400 cm^{-1} with a Carl Zeiss Jena model UR-20 spectrophotometer.

ESR measurements were performed at 9.4 GHz (X band) using a standard JEOL-JES-3B equipment, at room and liquid nitrogen temperatures.

Results and Discussion

IR Spectra

The representative frequencies range of the ligand and U(IV)-complex IR spectra is given in Fig.3 and some vibration bands are presented in Table 1.

The presence of an additional band at ≈1133 cm^{-1} in the U(IV)-complex spectrum, which can be attributed to the ν_{as}(U-O) vibration [8], confirms the coordination of the uranium ions at the ligand through the oxygen atoms.

Vibrations corresponding to polyoxoanions appear in the 400÷1000 cm^{-1} region [9]. The IR spectrum of the ligand presents two asymmetric vibration frequencies for the W=O_d bond (at 950 and 970 cm^{-1}), due to the difference between W=O_d bonds into the {AsW_9} units and into the four binding WO_6 octahedra [10]. In the uranium(IV)-complex spectrum, ν_{as}(W-O_d) vibration band appears as a single broad absorption at ≈960 cm^{-1}.

In the IR spectrum of the complex, the asymmetric vibrations of the tricentric W-O_c-W bonds into the edge-sharing WO_6 octahedra are shifted with ≈5 cm^{-1}.

The ν_{as}(As=O_a) vibration band which appears as a shoulder into the ligand spectrum is missing into the complex spectrum.

The frequencies corresponding to the W-O_b-W bonds into the corner-sharing WO_6 octahedra of the ligand present a red-shift of ≈15 cm^{-1} into the IR spectrum of the complex, when O_b binds one {AsW_9} unit and one coupling WO_6 octahedron, and a small blue-shift of ≈5 cm^{-1}, when O_b binds two octahedra of the same Keggin unit.

The broad band centered at 740 cm^{-1} in the IR spectrum of the complex is the superposition of ν_{as}(W-O_a) and tricentric ν_{as}(As-O-W) vibrations.

The broad band in the 700-600 cm^{-1} region of the IR ligand spectrum assigned to ν_{as}(W-O-W) vibrations becomes more distinct in the IR spectrum of the complex (619 cm^{-1}, 640 cm^{-1}).

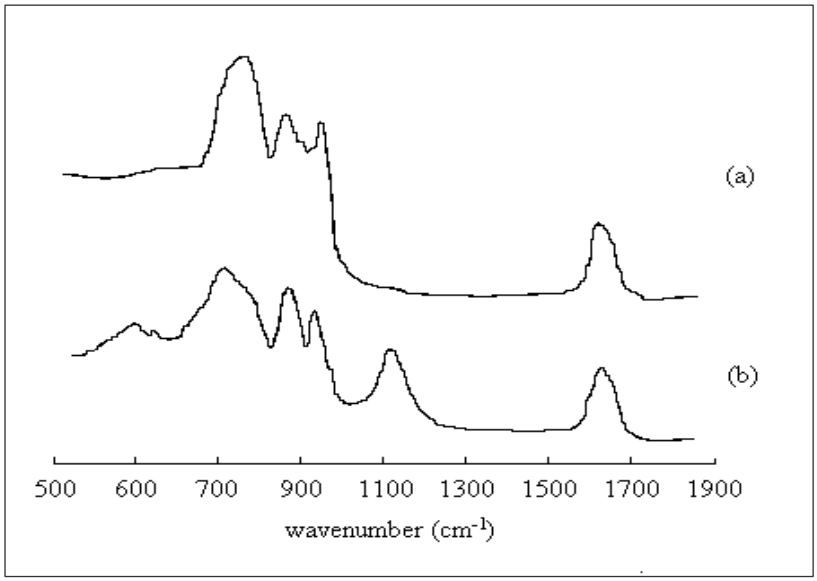

Fig. 3. IR spectra of the ligand (a) and of the U(IV)-complex (b)

The stretching and deformation bands of the water molecules (Table 1) are very broad and present some shoulders. This proves the existence of some hydrogen bonds involving the external oxygen atoms of the complex.

Table 1. The most important IR vibrations of the ligand and U(IV)-POM complex

	$\nu_{as}(W=O_d)$	$\nu_{as}(W-O_c-W)$	$\nu_{as}(W-O_b-W)$	$\nu_{as}(W-O_a)+\nu_{as}(As-O-W)$	$\delta(H-O-H)$	$\nu(H_2O)$
Ligand	950 (m,sp) 970 (s,sp)	890 (s,b)	805 (sh,b) 785 (vs,b)	765 (sh,b)	1 630 (m,b) 1 648 (sh,b) 1 668 (sh,b)	3 450 (s,b) 3 580 (s,b)
U(IV)-POM	960 (s,b)	895 (s,b)	810 (sh,b) 770 (sh,b)	740 (sh,b)	1 633 (m,b) 1 655 (sh,b)	3 500 (s,b)

w-weak, m-medium, s-strong, sh-shoulder, b-broad, sp-sharp, vs-very strong, vw-very weak

The analysis of the IR spectra indicates the coordination of U(IV) ions at the lacunar regions of the ligand ($S_1 \div S_4$ sites) by the oxygen atoms O_d from the Keggin units and WO_6 binding octahedra.

ESR Spectra

The ESR spectrum obtained at room temperature (Fig.4) exhibits the most intense signals in the 3250÷3400 G region. The values of the corresponding gyromagnetic factors, being slightly increased above the free electron g_0=2.0023 value, indicate that the oxidation state of tungsten ions is 6+ (the paramagnetic state of this ion would give ESR signals with $g<g_0$) [11]. Thus, the obtained spectrum is the exclusive contribution of U(IV) ions.

The shape of ESR spectrum could be treated conveniently by considering each U(IV) ion in a cubic configuration and the weak field approximation, with states $\left|L=3,S=1,JM_J\right\rangle$ (hereafter referred to as [$\left|JM_J\right\rangle$] representation), where J=L+S,…, | L-S| =4,3,2 is the total angular momentum and M_J their Oz component. In a cubic crystalline field, the degenerance of the ground state (J=4) is partial removed, resulting the $\Gamma_1(1)$, $\Gamma_4(3)$, $\Gamma_3(2)$, $\Gamma_5(3)$ multiplets. Γ_5 or Γ_1 can be the lowest, but only the first of them is ESR active [12]. Because we have obtained ESR spectrum even at room temperature, we conclude that Γ_5 is the lowest multiplet. Their three sulevels Ψ_1, Ψ_2, Ψ_3 are linear combinations of different $\left|J=4,M_J\right\rangle$ wave functions as Table 2 indicates. Using the Clebsch-Gordan coefficients $\left\langle M_L M_S \left| JM_J \right.\right\rangle$ we have the wave functions in [$\left|M_L M_S\right\rangle$] representation ($M_L$=±3, ±2, ±1, 0 and M_S=±1/2) and the composition (in %) of the atomic $\left|JM_J\right\rangle$ states in terms of f_σ, f_π, f_δ and f_ϕ orbitals.

f_σ (f_{z3}), f_π (f_{xz2}, f_{xy2}) and f_ϕ ($f_{x(x^2-3y^2)}$, $f_{y(3x^2-y^2)}$), corresponding respectively to | M_L| =0,1,3, are localized and considered as nonbonding. f_δ ($f_{z(x^2+y^2)}$, f_{xyy}) is one antibonding orbital and interacts with the ligand orbital. We observe that for $5f^2$ actinide, f_π and f_δ dominate Ψ_1 wave function and f_δ dominates, Ψ_2 and Ψ_3 which indicate a small probability of superposition between the U(IV) and As(III) orbitals. So, U(IV) binds only the oxygen atoms.

The contribution (in %) of the atomic $|JM_J\rangle$ states in terms of M_S values are presented in Table 3. Ψ_1 is dominate by M_S=0, Ψ_2 by M_S=1 and Ψ_3 by M_S=-1, which confirm the model of effective spin S_{eff} =1.

The g values of the fine structure (g_{z_1} =2.098, g_{y_1} =2.089, $g_{x_1} \approx g_{x_2}$ =2.067, g_{y_2} =2.051, g_{z_2} =2.031) indicate a small orthorhombic distortion from the cubic symmetry.

This results indicates that every U(IV) ion is surrounded by eight O^{2-} ions, arranged like basis for two antiprism configurations.

Table 2. The composition of Γ_5 multiplet in [$|JM_J\rangle$] and [$|M_L M_S\rangle$] representations

[$\|JM_J\rangle$] REPRESENTATION	[$\|M_L M_S\rangle$] REPRESENTATIONS			
	f_σ (%)	f_π (%)	f_δ (%)	f_ϕ (%)
$\Psi_1 = \frac{1}{\sqrt{2}}[\|4,-2\rangle - \|4,2\rangle]$		53.6	42.9	3.6
$\Psi_2 = -\frac{1}{\sqrt{8}}\|4,1\rangle + \sqrt{\frac{7}{8}}\|4,-3\rangle$	4.46	6.7	66.96	21.88
$\Psi_2 = -\frac{1}{\sqrt{8}}\|4,-1\rangle + \sqrt{\frac{7}{8}}\|4,3\rangle$	4.46	6.7	66.96	21.88

The orthorhombic ESR spectrum obtained even at room temperature proves that the 5f electrons are trapped at the uranium sites, indicating the dominance of the spin-orbit coupling.

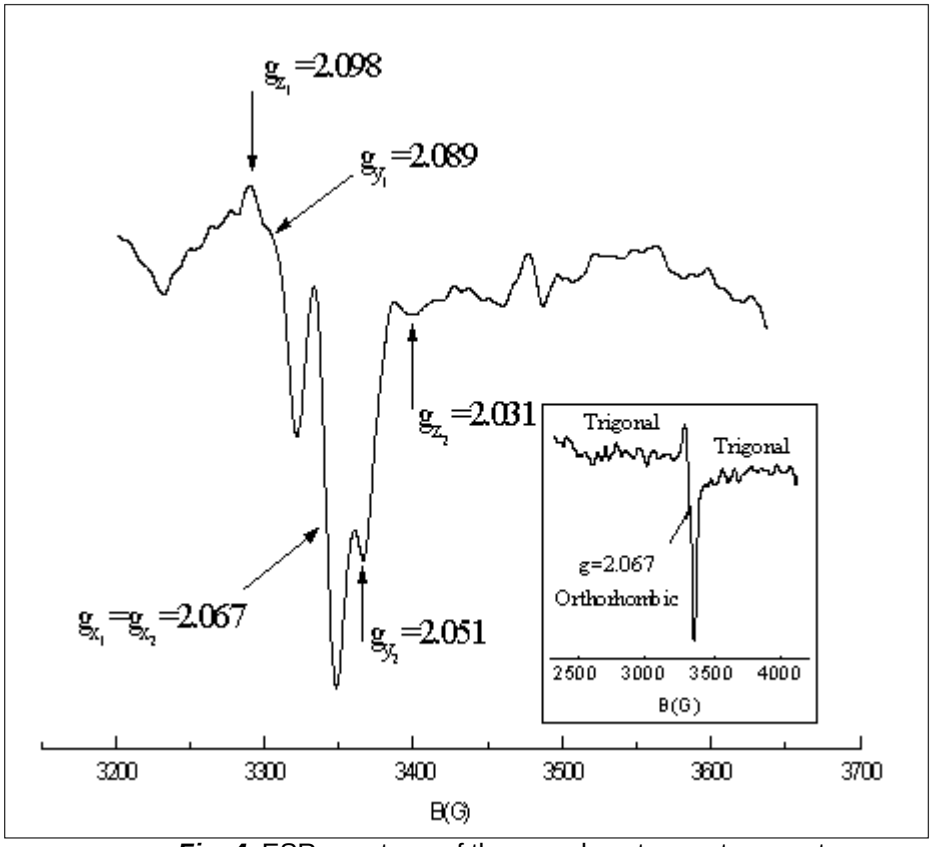

Fig. 4. ESR spectrum of the complex at room temperature

Table 3. The composition of Γ_5 multiplet in M_S values

Orbital	(%) M_S values		
	M_S=-1	M_S=0	M_S=1
Ψ_1	28.6	42.9	28.6
Ψ_2	4.46	28.58	66.96
Ψ_3	66.96	28.58	4.46

By lowering the temperature to T=77 K, the shape of the spectrum remains unchanged. The small features around the “central” signals (Fig.4, into the medallion of the figure) are due to the transitions into the excited multiplets of U(IV) ions or to some trigonal distorted species length-ways the diagonals of the cube [13].

Conclusions

Uranium(IV) ions coordinate the oxygen atoms of the POM, this fact resulting from the appearance of the additional band (ν_{as}(U-O)) in the IR spectrum of the complex.

The vibration IR bands of the U(IV)-polyoxometalate are shifted due to the coordination of uranium ions into the S_i (i=1,…,4) active sites of the ligand, at terminal oxygen atoms O_d from $\{AsW_9\}$ units and binding WO_6 octahedra.

The U(IV) ions are situated in distorted orthorhombic cubic environment, as the ESR spectra indicate.

The Γ_5 multiplet is energetically the lowest and can be characterized by an effective spin S_{eff}=1. Some amount of the complex can be distorted towards the cube diagonals, resulting some trigonal distorted cubic species.

Based on these results, we propose in Fig.5 a schematic representation of the uranium ions coordination at the ligand, in which the two U(IV) ions coordinate the S_1-S_2 and S_3-S_4 sites, respectively.

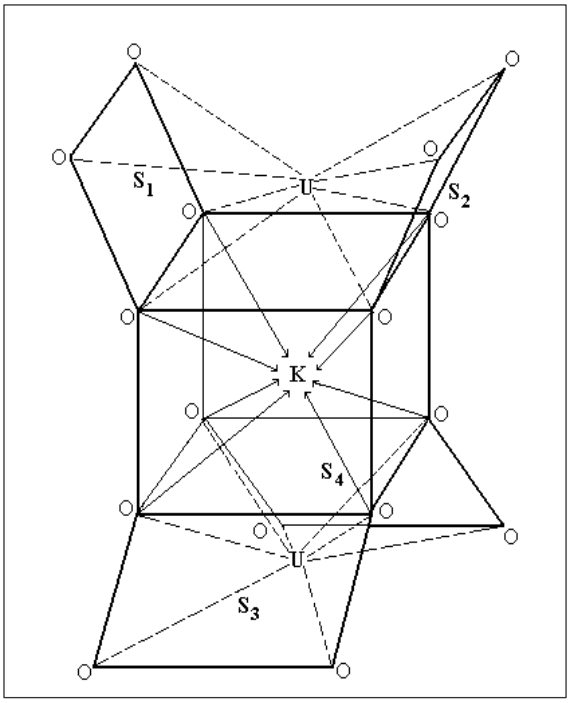

Fig. 5. A representation of U(IV) coordination at POM

REFERENCES

1. Gh. Marcu, M. Rusu, Chimia polioxometalatilor, Ed. Tehnica, Buc. 1997.
2. P. Le Maguerés, L. Ouahab, S. Golhen, D. Grandjean, O. Peña, J.-C. Jegaden, C.J. Gómez-Garcia, and P. Delhaés, *Inorg. Chem*., **33**, 5180 (1994).
3. M. Leyrie, J. Martin-Fréré, and O. Hervé, *C.R. Acad. Sci., Ser.C*, **279**, 895 (1974).
4. A. Müller, F. Peters, M. T. Pope, and D. Gatteschi, *Chem. Rev*., **98**, 239 (1998).
5. M. Leyrie, O. Hervé, A. Tézé, J. Jeannin, Inorg. Chem., 19 (1979) 1746.
6. J. Jeannin, and J. Martin-Fréré, *J. Am. Chem. Soc*., **103**, 1664 (1981).
7. D. Gournier, D. Caurant, J. C. Berthet, C. Boisson, and M. Ephritikhine, *Inorg. Chem*., **36**, 5931 (1997).
8. R. A. Satten, D. Young, and D. M. Gruen, *The J. of Chem. Phys*., **33**, 1140 (1960).
9. C. J. Gómez-Garcia, E. Coronado, P. Gómez-Romero, and N. Casañ-Pastor, *Inorg. Chem*., **32**, 89 (1993).
10. C. J. Gómez-Garcia, C. Giménez-Saiz, S. Triki, E. Coronado, P. Le Magueres, L. Ouahab, L. Ducasse, C. Sourisseau, and P. Delhaes, *Inorg. Chem*., **34**, 4139 (1995).
11. Jing-yang Niu, Xiao-zeng You, and Chun-ying Duan, *Inorg. Chem*., **35**, 4211 (1996).
12. I. Ursu, Magnetical Resonance of uranium compounds, Acad. RSR Ed., Bucureşti, p.189,1979.
13. A. Yariv, *Phys. Rev*., **128**, 1588 (1962).

STUDIA UNIVERSITATIS BABEŞ-BOLYAI, PHYSICA, XLIV, 1, 1999

IR, ESR, AND MAGNETIC INVESTIGATIONS OF SOME TRANSITION METAL COMPLEXES OF γ-L-GLUTAMYL DERIVATIVES

CRĂIȚA BĂLAN*, L. DAVID*, LETIȚIA GHIZDAVU, CORA CRĂCIUN*, O. COZAR*, D. RISTOIU***

ABSTRACT. Transition metal complexes of the three γ-L-glutamyl derivatives (γ–L–glutamyl–5–(*p*–nitroanilide) = L_1; γ–L–glutamyl–5–(*m*–nitroanilide) = L_2 and γ–L–glutamyl–5–(2-metoxy–nitroanilide) = L_3) with Cu(II), Co(II), Mn(II) and Fe(III) were synthesized and investigated by spectroscopic and magnetic measurements. In all the studied complexes the ligands act bidentately, the carbonyl oxygen and the nitrogen atom of the second amino group being involved in the coordination at metal ion. The local structure around the Cu(II) ions is pseudotetrahedral for the complexes of L_1 and L_2 and tetrahedral in the case of L_3 complexes. In Co(II), Mn(II) and Fe(III) complexes the metal ions are in the high spin form, with an octahedral stereochemistry.

Introduction

Glutamic acid is a natural aminoacid involved in glutamine, glutathion and a considerable number of proteins composition [1-5]. The ϒ–L–glutamyl amides and their organic and some inorganic derivatives have biological and pharmaceutical importance, being immunostimulator, analgesic, antiinflamator, and antitumoral agents [6-10]. In some previously synthesized metal complexes, the glutamic acid acts like bidentate ligand and some of these complexes present cis-trans isomers [11]. The metal complexes of the glutation were proved to be chemically very stable [12] and to have a considerable antifungal activity [10].

Given the important biochemical applications of γ-L-glutamyl derivatives (Fig.1), this paper presents some chemical-physical properties of their coordinative transition metal complexes with Cu(II), Co(II), Mn(II), and Fe(III).

* "Babeş-Bolyai" University, Departament of Physics, 3400 Cluj-Napoca, Romania

** "Babeş-Bolyai" University, Departament of Chemistry, 3400 Cluj-Napoca, Romania

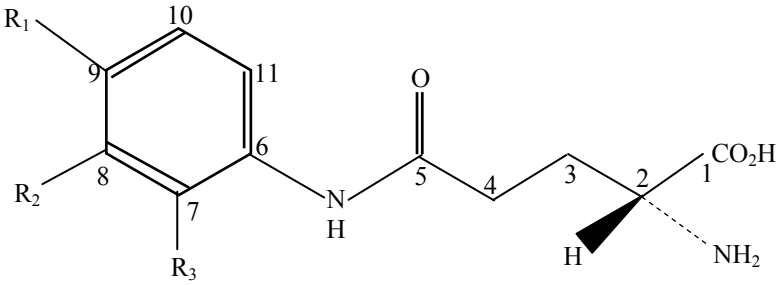

Fig. 1. Molecular structure of the investigated γ-L-glutamyl derivatives (L_1: R_1=NO_2, R_2=H, R_3=H; L_2: R_1=H, R_2=NO_2,R_3=H;L_3: R_1=NO_2, R_2=H, R_3=OCH_3

Experimental

The ligands L_1, L_2 and L_3 were prepared by reported procedure [4].

The $CuSO_4 \cdot 5H_2O$, $CoSO_4 \cdot 7H_2O$, $MnSO_4 \cdot 7H_2O$ and $Fe(NH_4)(SO_4)_2 \cdot 12H_2O$ solutions were prepared by solvating the corresponding metal salts in distilled water at high temperature. The ligand was solvated in NaOH solution at pH=9. The precipitate formed by mixing the ligand solution with metal salts solutions was filtered off, washed in NaOH solution, then in water, dried and kept in dark coloured bottles.

Elemental and thermal analysis leaded to the following molecular formulas of the synthesized metal complexes:

$Cu(L_1)_2 \cdot 2H_2O$	$Cu(L_2)_2 \cdot H_2O$	$Cu(L_3)_2 \cdot 5H_2O$
$Co(L_1)_2 \cdot 3H_2O$	$Co(L_2)_2 \cdot 2H_2O$	$Co(L_3)_2 \cdot 4H_2O$
$Mn(L_1)_2 \cdot 2H_2O$	$Mn(L_2)_2 \cdot 4H_2O$	$Mn(L_3)_2 \cdot 2H_2O$
$Fe(L_1)_3 \cdot 2H_2O$	$Fe(L_2)_3 \cdot 5H_2O$	$Fe(L_3)_3 \cdot 7H_2O$

IR spectra were recorded with a Karl Zeiss Jena UR-20 Spectrophotometer, in KBr pellets, in a range of 400-4000cm^{-1}. EPR spectra were recorded at 9.4 GHz (X band), using a standard JEOL–JES–3B equipment. Magnetic susceptibility measurements were made on powered samples using a Faraday type balance.

Results and discussion

Partial assignments of the IR absorption bands observed for the free ligands and the metal complexes are given in Table 1.

Table 1. Some IR absorption bands (cm^{-1}) of the investigated ligands and their metal complexes.

	ν(C=O)	$\nu(NH_2)$	ν(O–H)	$\nu(M–OH_2)$
$L_1 \cdot H_2O$	1700	3280	3500	–
$Cu(L_1)_2 \cdot 2H_2O$	1640	3180	3525	–
$Co(L_1)_2 \cdot 3H_2O$	1628	3152	3560	762
$Mn(L_1)_2 \cdot 2H_2O$	1617	3125	3510	760
$Fe(L_1)_3 \cdot 2H_2O$	1610	3100	3534	–
$L_2 \cdot 4H_2O$	1692	3112	3440	–
$Cu(L_2)_2 \cdot H_2O$	1611	2984	3522	–
$Co(L_2)_2 \cdot 2H_2O$	1642	3108	3651	758
$Mn(L_2)_2 \cdot 4H_2O$	1681	3114	3510	760
$Fe(L_2)_3 \cdot 5H_2O$	1688	3122	3530	–
$L_3 \cdot 2H_2O$	1650	3192	3385	–
$Cu(L_3)_2 \cdot 5H_2O$	1632	3144	3502	–
$Co(L_3)_2 \cdot 4H_2O$	1614	3075	3428	754
$Mn(L_3)_2 \cdot 2H_2O$	1605	3108	3425	758
$Fe(L_3)_3 \cdot 7H_2O$	1610	3132	3410	–

A comparative study of these spectral data reveals significant shifts of the following three vibration bands:

- the lowering of the ν(C=O) frequency values in the complexes spectra, indicating the involvement of the carbonyl oxygen atom in the metal coordination [13];
- the shift of the $\nu(NH_2)$ vibration bands, stating the involvement of the nitrogen atom from the secondary amino group in the metal coordination;
- the ν(O-H-O) vibration band is slightly shifted in the coordinative compounds, due to the increased number of hydrogen bonds.

Additional bands appearing at ≈760 cm^{-1} in the IR spectra of Co(II) and Mn(II) complexes are characteristic for water molecules in the inner coordination sphere [14, 15].

The ν(C=O) and $\nu(NH_2)$ stretching vibrations are shifted to lower frequencies as the metal is changed in the order Fe(III)<Mn(II)<Co(II)<Cu(II). The IR data are in good agreement with Irving-Williams stability [16, 17].

The powder ESR spectra of Cu(II) complexes at room temperature (Fig.2) are typical for monomeric species with a CuN_2O_2 cromophore [18]. The values of the *g* factors (Cu(II)–L_1: $g_{\|}$ = 2.254, $g_{\perp}$ = 2.150; Cu(II)–L_2: $g_{\|}$ = 2.238, $g_{\perp}$ = 2.071 and Cu(II)–L_3: $g_{\|}$ = 2.417, $g_{\perp}$ = 2.065) suggest psudotetrahedral (Cu(II)–L_1 and Cu(II)–L_2) and tetrahedral (Cu(II)–L_3) environments around the metal ions.

The powder ESR spectra of Mn(II) complexes are characterized by quasi-isotropic *g* tensors with principal values (g ~ 2.0018) close to the spin-only value.

ESR spectra of Fe(III) are almost isotropic (g ~ 2.002). The presence of a weak signal at g ≈ 4 suggests a small distortion of the octahedral symmetry around the metal ion.

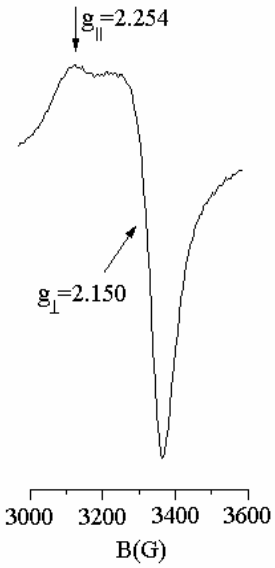

Fig. 2. Powder ESR spectrum of Cu(II)-L_1 complex at room temperature

The magnetic susceptibility measurements indicate a Curie–Weiss behaviour (Fig.3), with magnetic moments specific for monomeric species. The values of the magnetic moments (Table 2) were calculated considering the temperature independent contributions.

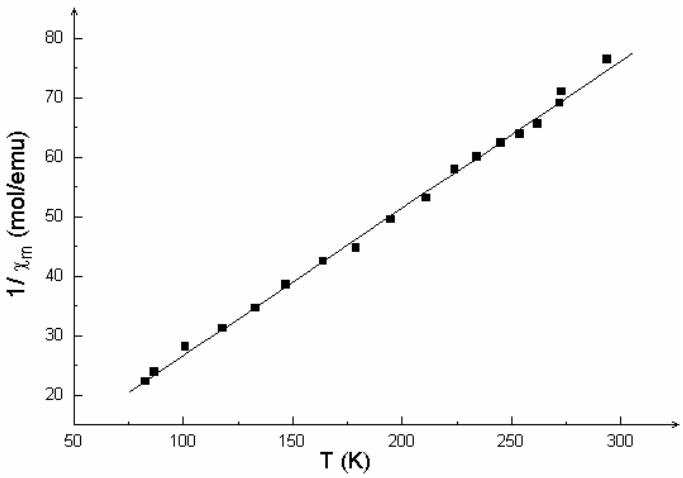

Fig. 3. Temperature dependence of $1/\chi_m$ for $Co(L_2)_2 \cdot 4H_2O$

Table 2. Values of magnetic moments and Curie temperatures for the investigated metal complexes

	μ_{ef} (μ_B)	θ (K)
$Cu(L_1)_2 \cdot 2H_2O$	1.71	5
$Co(L_1)_2 \cdot 3H_2O$	3.63	-12
$Mn(L_1)_2 \cdot 2H_2O$	6.71	-18
$Fe(L_1)_3 \cdot 2H_2O$	5.05	35
$Cu(L_2)_2 \cdot H_2O$	1.80	13
$Co(L_2)_2 \cdot 2H_2O$	5.14	-32
$Mn(L_2)_2 \cdot 4H_2O$	6.71	-20
$Fe(L_2)_3 \cdot 5H_2O$	5.87	30
$Cu(L_3)_2 \cdot 5H_2O$	1.92	-11
$Co(L_3)_2 \cdot 4H_2O$	5.20	-10
$Mn(L_3)_2 \cdot 2H_2O$	5.87	36
$Fe(L_3)_3 \cdot 7H_2O$	5.25	42

The magnetic moments are in the normally observed range for four-coodinated Cu(II) species, while those corresponding to high–spin Co(II), Mn(II) and Fe(III) rather yield local octahedral environments. The paramagnetic Curie temperatures (Table 2) indicate the presence of some exchange interactions between the metal ions, due to the formation of intermolecular hydrogen bonds [19].

Conclusions

The IR spectra show γ–L–glutamyl derivatives acting as bidentate ligands with coordination involving the carbonyl oxygen and the nitrogen atom of the second amino group. In the case of Co(II) and Mn(II), two H_2O molecules coordinate in the apical postions, resulting an octahedral local structure. Three bidentate ligand molecules coordinate Fe(III) ions. The ESR spectra and magnetic data confirm the mentioned local symmetries.

The obtained structural data allow us to propose the following molecular formulas for the studied metal complexes:

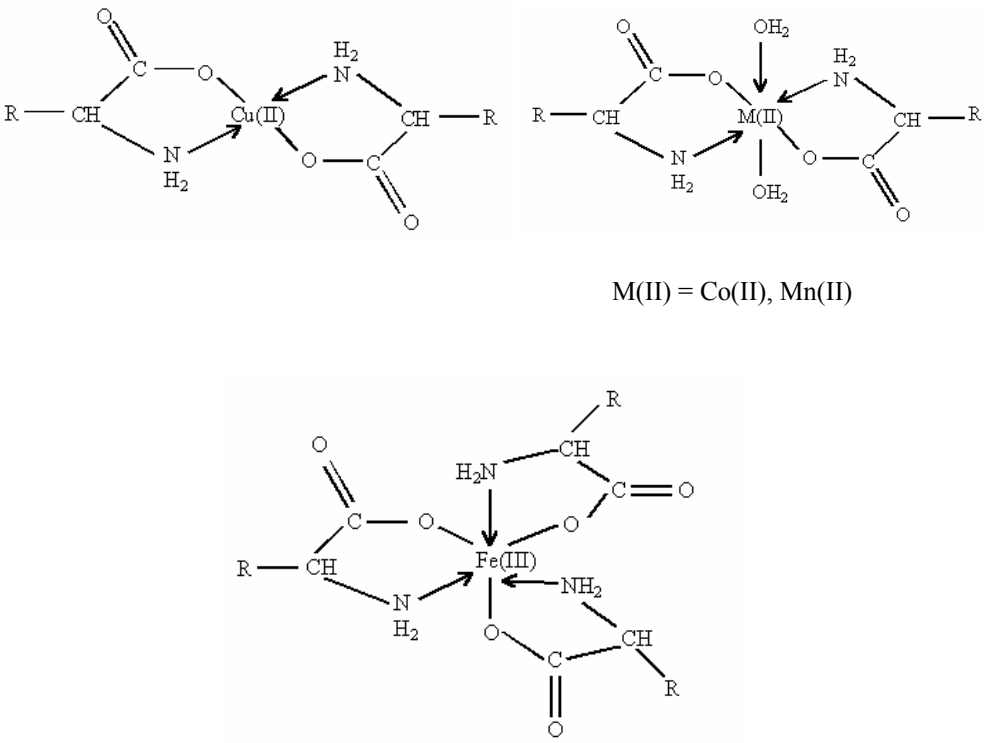

Fig. 4. Suggested structures of the studied complexes

REFERENCES

1. L. F. Mackenzie, G. J. Davies, M. Schuelein, S. G. Withers, Biochemistry, 36, 5893 (1997).
2. A. Adach, J. Janyst, M. Cieslak-Golonka, Spectrosc. Lett., 28, 1259 (1995).
3. P. Francesco, J. Chromatogr., A 802, 315 (1998).
4. K. J. Alok, K. Farid, J. Electrochem. Soc. India, 45, 115 (1996).
5. Ye. I. Dudina, V. Ye. Formazyuk, V. I. Sergiyenko, T. N. Gorshkhova, Vestn. Ross. Akad. Med. Nauk, 3, 31 (1995).
6. F. Tellier, F. Acher, I. Brabet, J. P. Pin, J. Bockaert, R. Azerad, C. R. Acad. Sci. Ser. II, Mec., Phys., Chim., Astron., 321, 385 (1995).
7. C. Biggs, M. Starr, L. Fowler, P.Whitton, Biochem. Soc. Trans., 24, 173 (1996).
8. J. Krieglstein, K. Lipperd, G. Poech, Neuropharmacology, 35, 1737 (1997).
9. W. L. Jacobs, Clin. Chim. Acta, 31, 175 (1971).
10. H. P. Shirastava, R. K. Shirastava, J. Indian Chem. Soc., 72, 435 (1995).
11. Kh. Khakimov, N. T. Ahmkhodzhaeva, O. T. Khadzhaev, Koord. Khim., 5, 21 (1979).
12. I. Cristea, S. Mager, C. Bâtiu, G. Plé, Rev. Roum.Chim., 39, 1435 (1994).
13. K. Nakamoto, "Infrared Spectra of Inorganic and Coordination Compounds", Wiley-Interscience, New York, 1970.
14. S. L. Stefan, B. A. El-Shetary, W. G. Hanna, S. B. El-Maraghy, Microchemical J., 35, 51 (1987).
15. H. A. Dessouky, R. M. Issa, M. M. Moustafa, Acta Chim. Hung., 126, 653 (1969).
16. J. J. R. Frausto da Silva, R. J. P. Williams, "The Biological Chemistry of the Elements", Clarendon Press, Oxford, 1994.
17. W. B. Jensen, "The Lewis acid-base concepts" , Wiley, New York, 1980.
18. F. E. Mabbs, D. Colisson, "Electron Paramagnetic Resonance of d Transition Metal Compounds", Elsevier, Amsterdam, 1992.
19. R. L. Carlin, "Magnetochemistry, Springer Verlag, Berlin, 1986.

STUDIA UNIVERSITATIS BABEŞ-BOLYAI, PHYSICA, XLIV, 1, 1999

IR AND ESR STUDIES OF $K_5[PVMo_2W_9O_{40}(H_2O)]\cdot 23H_2O$ HETEROPOLYOXOMETALATE COMPLEX

C. CRĂCIUN*, L. DAVID*, M. RUSU, O. COZAR*, D.RISTOIU*, I. BRATU***[3]**

ABSTRACT. The $K_5[PVMo_2W_9O_{40}(H_2O)]\cdot 23H_2O$ complex was investigated by IR and ESR spectroscopy. The shift of the $\nu_{as}(M{=}O_{a,d})$ and $\nu_{as}(M\text{-}O_{b,c}\text{-}M)$ vibrations (M=W, Mo) in the 700÷1100 cm^{-1} region of the IR spectrum of the complex comparative with the IR spectrum of the ligand shows the substitution of one tungsten atom of the POM by the vanadium atom. The ESR spectrum of the complex obtained at room temperature is a superposition in the same amount of one axial spectrum with the resolved V(IV) hyperfine structure (g_{II}=1.922, $g_{\perp}$=1.972, A_{II}=181 G, $A_{\perp}$=63 G) and a very large isotropic component (g_{iso}=1.972, ΔB_{iso}(p-p)=450 G) due to dipolar interactions between V(IV) and Mo(V) ions into a one-electron-reduced specie. The ESR spectrum of the frozen DMSO-H_2O solution of the complex indicates the coexistence of two magnetically nonequivalent isomers.

Introduction

Polyoxometalates with mixed addend atoms like vanadium, molybdenum or tungsten are very interesting from structural point of view [1]. Some structural features namely the presence of mixed valence anions, the proximity of the easier vanadium and molybdenum ions into the structure, the electron delocalisation into the POM or contrary the presence of trapped electrons on different ions [1-3] lead to different spectroscopic properties and applications of these compounds.

This paper reports IR and ESR spectroscopic investigations of the $K_5[PVMo_2W_9O_{40}(H_2O)]\cdot 23H_2O$ heteropolyoxometalate, which presents one α-Keggin structure (Fig.1) [4]. This complex derives from the α-

* Department of Physics, Babeş-Bolyai University, 1 Kogalniceanu, 3400 Cluj-Napoca
** Department of Chemistry, Babeş-Bolyai University, 1 Kogalniceanu, 3400 Cluj-Napoca
*** Inst. of Isotopic and Molec. Tech., 3400 Cluj-Napoca, Romania

$[PMo_2W_{10}O_{40}]^{3-}$ anion in which one tungsten atom is replaced by a vanadium ion. The addends (V, W, Mo) are usually octahedraly coordinated by the oxygen atoms. Previous X-ray and NMR studies on Keggin isostructural complexes showed that the MoO_6 and VO_6 octahedra are adjacent and share a corner oxygen atom [5].

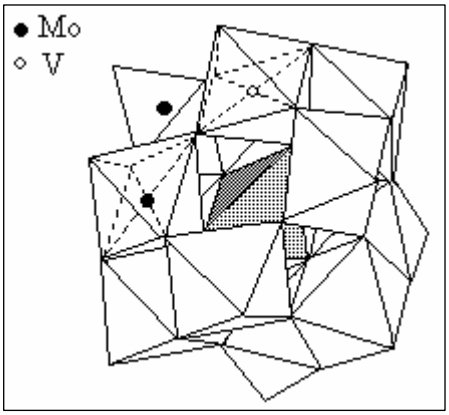

Fig.1 Structure of $K_5[PVMo_2W_9O_{40}]\cdot 23H_2O$ heteropolyoxometalate complex

Experimental

The V(IV)-POM complex was prepared according to the procedure described in paper [1]. IR spectra were obtained in KBr pellets in the 4000÷400 cm^{-1} range with a Carl Zeiss Jena model UR-20 spectrophotometer.

ESR measurements were performed at 9.4 GHz (X band) using a standard JEOL-JES-3B equipment, at room temperature and T=100 K.

Results and discussions

IR Spectra

The coordination mode of the vanadium(IV) ion at the ligand was obtained by comparing the IR frequencies of the V(IV)-POM complex with those of the polyoxometalate (Table1). Fig.2 shows the 700÷1900 cm^{-1} IR spectra of the complex and the ligand. The strong shift of $\nu_{as}(W{=}O_d)$ and $\nu_{as}(Mo{=}O_d)$ frequencies in the IR spectrum of the complex indicates the formation of the $V{=}O_d$ vanadyl group into the complex [6]. These bands are independently resolved in the ligand spectrum and in the complex spectrum they are superposed into a single band with a shoulder.

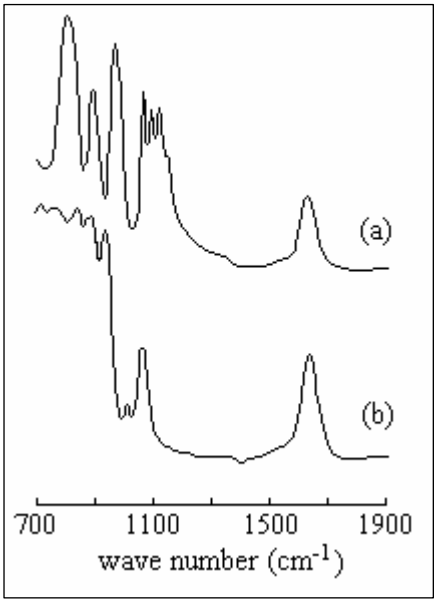

Fig.2 IR spectra of the V(IV)-POM complex(a) and the ligand (b)

Two vibration bands for tricentric W-O_c-W units are present in the IR spectrum of the ligand, while the complex spectrum shows only the highest of these two.

The coordination of the vanadium ion at O_a and O_b atoms results by comparing the shape of the spectra in 750÷850 cm^{-1} region. The ν_{as}(W-O_a) (760 cm^{-1}) and ν_{as}(W-O_b-W) (840 cm^{-1}) vibration bands form only one strong broad band in the complex spectrum, approximately centered at the average of the above frequencies.

The presence of a single asymmetric band ν_{as}(P-O_a) in the IR spectrum of the ligand corresponds to a highly symmetric PO_4 unit [2]. This fact suggests the equivalence of molybdenum and tungsten atoms when coordinating the O_a central atoms. The involvement of V(IV) ion in the coordination at polyoxometalate provokes the splitting of the ν_{as}(P-O_a) band in four bands suggesting the lowering of the local symmetry around the phosphorus atom (C_s). The presence of the fourth band is due to the coexistence of unequivalent Keggin units in the sample [2].

The shifts of the deformation and stretching vibration bands of the water molecules are due to the raising of a basic character of the O_d atoms bounded to the vanadium(IV) ion and their involvement in hydrogen bonds [7].

Table 1. Some IR bands (cm^{-1}) of the ligand and V(IV)-POM complex

BAND	LIGAND (CM^{-1})	V(IV)-POM (CM^{-1})
$\nu(H_2O)$	2950÷3700 (s,b)	3150÷3700 (s,b)
δ(H-O-H)	1645 (m,sp)	1650÷1630 (m,b)
$\nu_{as}(P\text{-}O_a)$	1065 (s,sp)	1150 (m,sh) 1117, 1090, 1065 (s,sp)
$\nu_{as}(Mo{=}O_d)+\nu_{as}(W{=}O_d)$	1015 (w,sp) 937 (vs,sp)	980 (vs,sh) 965 (vs,sp)
$\nu_{as}(W\text{-}O_c\text{-}W)$	890, 880 (vs,sp)	890 (m,sp)
$\nu_{as}(W\text{-}O_a)+\nu_{as}(W\text{-}O_b\text{-}W)$	840, 760 (vs,b)	805 (vs,b)
$\nu_{as}(W<^{O}_{O})$	715 (s,b)	685 (w,b)
$\nu_{as}(P\text{-}O\text{-}W)$	625 (w,b) 595 (w,sh)	620 (m,sp) 600 (w,sh)
$\nu_s(P\text{-}O_a)$	535, 503 (w,b)	518, 493 (w,b)

w-weak, m-medium, s-strong, sh-shoulder, b-broad, sp-sharp, vs-very strong

The IR data assignment indicates the coordination of the vanadium atom at O_a, O_b, O_c and O_d oxygen type atoms and the presence of different isomers in the sample.

ESR Spectra

Some ESR parameters of $K_5[PVMo_2W_9O_{40}(H_2O)]\cdot 23H_2O$ complex at room and liquid nitrogen temperatures have been reported by E.Cadot et al in [1]. They have obtained an axial spectrum typical for V(IV) ions, with resolved hyperfine features.

The powder ESR simulated spectrum of the complex at room temperature revealed the presence of a new specie.

The powder ESR spectrum of the complex performed at room temperature (Fig.3) is a superposition of one axial component with resolved V(IV) hyperfine structure and one isotropic and very broad component.

The axial component can be described by the following spin Hamiltonian for a d^1 system with C_{4v} symmetry [8]:

$$H = \beta[g_{\parallel} B_z S_z + g_{\perp}(B_x S_x + B_y S_y)] + A_{\parallel} S_z I_z + A_{\perp}(S_x I_x + S_y I_y)$$

where $g_{\parallel}$, $g_{\perp}$ and $A_{\parallel}$, $A_{\perp}$ are the axial principal values of the gyromagnetic and hyperfine tensors respectively, β is the Bohr magneton, (B_x, B_y, B_z) are

the components of the applied magnetic field lengthways the principal **g** axes, (S_x, S_y, S_z) and (I_x, I_y, I_z) are the components of the electronic and nuclear spin angular momentum operators respectively.

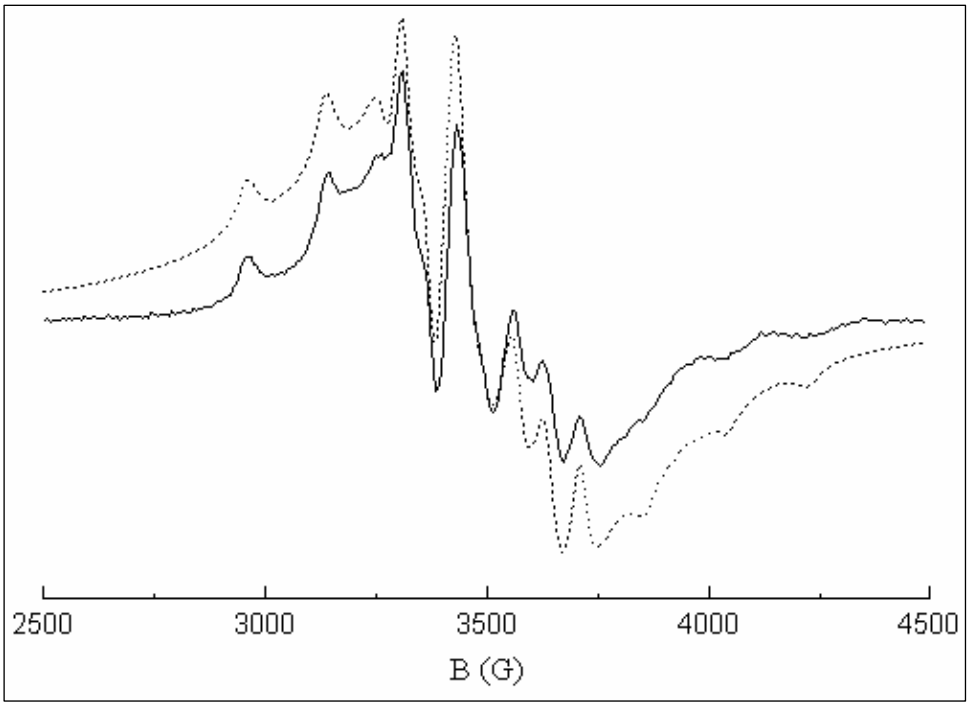

Fig.3 Experimental ESR spectrum of the powder V(IV)-POM complex, at room temperature (normal line) and the simulated spectrum (dashed line)

This component exhibits eight hyperfine components both in the perpendicular and in the parallel bands due to the hyperfine coupling of the unpaired electron with the nuclear spin (I=7/2) of the ^{51}V isotope.

The isotropic broad signal is due to a strong dipolar interaction between the V(IV) and the neighboring Mo(V) ion [9]. This signal can be assigned to a one-electron reduction product with mixed valence Mo(V) and Mo(VI) ions.

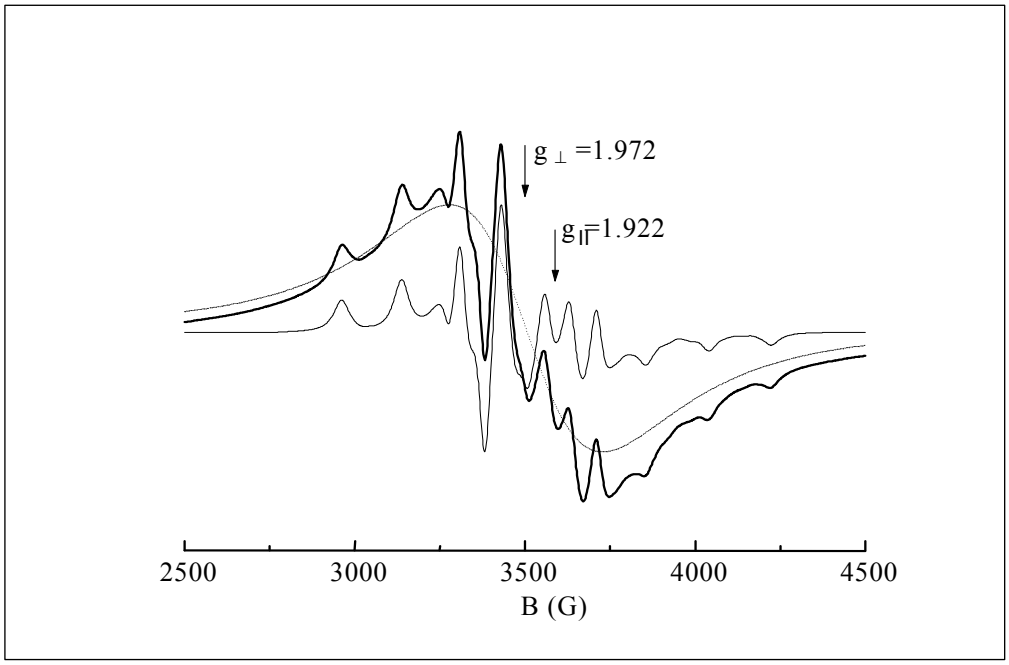

Fig.4 The components of the simulated spectrum of the complex

There is a good agreement between the positions of the hyperfine signals into the simulated and experimental spectra. However the simulated spectrum is wider towards his wings because we have assumed a pure Lorentzian lineshape for the isotropic component of the spectrum. This indicates that the broadening of the quasiisotropic signal is due both to the heterodipolar interaction V(IV)-Mo(V) and to the hyperfine coupling of the unpaired electron with the V(IV) ion. The quasiisotropic signal must be a composition of one Lorentzian and one Gaussian part.

The best fit of ESR spectrum was made (Fig.4) by considering g_{II}=1.922, $g_{\perp}$=1.972, A_{II}=181 G, $A_{\perp}$=63 G, ΔB_{II}(p-p)=30 G, $\Delta B_{\perp}$(p-p)=33 G parameters for the axial specie and g_{iso}=1.972, ΔB_{iso}(p-p)=450 G for the isotropic specie. The two components contribute in the same amount (50%) to the whole spectrum. The principal axes of **g** and **A** tensors were presumed coincident for the axial spectrum, with g_{II} direction parallel to the $V=O_d$ bond.

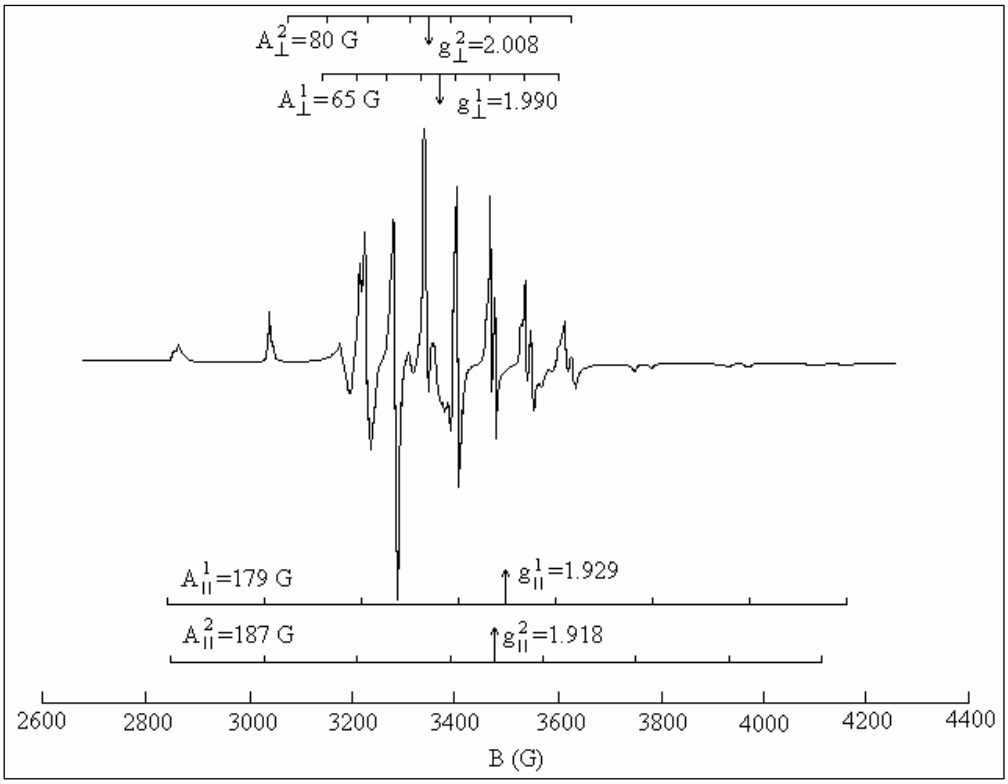

Fig.5 The DMSO-H_2O V(IV)-POM frozen solution ESR spectrum (T=100 K)

The rough approximation of the signals peak-to-peak width, $\Delta B_{pp} \sim M_2/J_0$, where M_2 is the second moment of the Lorentzian line and J_0 is the isotropic exchange parameter [10], leads to a small $J_0 \approx 0.034$ cm^{-1} value. This corresponds to an important lifetime of the electrons between the two V(IV) and Mo(V) ions and presumably to a hopping process which also involves the Mo(VI) ion.

The isotropic spectrum disappears by frozening the DMSO-H_2O solution of the complex at T=100 K (Fig.5). The obtained ESR spectrum is axial with two sets of hyperfine lines corresponding to two magnetically nonequivalent monomeric species. One specie has the ESR parameters close to those of the powder axial specie: g_{II}^{1}=1.929, $g_{\perp}^{1}$=1.990, A_{II}^{1}=179 G, $A_{\perp}^{1}$=65 G, while for the other specie: g_{II}^{2}=1.918, $g_{\perp}^{2}$=2.008, A_{II}^{2}=187 G, $A_{\perp}^{2}$=80 G.

Conclusions

The IR investigations of $K_5[PVMo_2W_9O_{40}(H_2O)]\cdot 23H_2O$ complex indicate the coordination of the vanadyl group at the α-Keggin structure, by the substitution of one $W{=}O_d$ unit.

ESR spectrum of the V(IV)-POM complex obtained at room temperature indicates the presence of two different species, one axial with g_{II}=1.922, $g_{\perp}$=1.972, A_{II}=181 G and $A_{\perp}$=63 G parameters and another reduced mixed valence (Mo(V)-Mo(VI)) specie with g_{iso}=1.972. V(IV) and Mo(V) ions are dipolar coupled with a very weak exchange interaction ($J_0 \approx 0.034$ cm^{-1}). The two isomers detected by IR spectroscopy appear also in frozen DMSO-H_2O solution.

REFERENCES

1. E. Cadot, M. Fournier, A. Tézé, G. Hervé, *Inorg. Chem.*, **35**, 282 (1996).
2. C. J. Gómez-Garcia, C. Giménez-Saiz, S. Triki, E. Coronado, P. Le Magueres, L. Ouahab, L. Ducasse, C. Sourisseau, P. Delhaes, *Inorg. Chem.*, **34**, 4139 (1995).
3. J. Canny, R. Thouvenot, A. Tézé, G. Hervé, M. Leparulo-Loftus, M. T. Pope, *Inorg. Chem.*, **30**, 976 (1991).
4. Y. P. Jeannin, *Chem. Rev.*, **98**, 51 (1998).
5. E. Cadot, R. Thouvenot, A. Tézé, G. Hervé, *Inorg. Chem.*, **31**, 4128 (1992).
6. A. Müller, R. Sessoli, E. Krickemeyer, H. Bögge, J. Meyer, D. Gatteschi, L. Pardi, J. Westphal, K. Hovemeier, R. Rohlfing, J. Döring, F. Hellweg, C. Beugholt, M. Schmidtmann, *Inorg. Chem.*, **36**, 5239 (1995).
7. Chue Wee Lee, Hyusoo So, *Bull. Korean Chem. Soc.*, **9**, 362 (1988).
8. Jeongmin Park, Hyunsoo So, *Bull. Korean Chem. Soc.*, **15**, 752 (1994).
9. S. Gupta, N. Khanijo, A. Mansingh, J. Non-Cryst. Solids, **181**, 58 (1995).
10. K. T. McGregor, Z. G. Soos, *J. Chem. Phys.*, **64 (6)**, 2506 (1976).

STUDIA UNIVERSITATIS BABEŞ-BOLYAI, PHYSICA, XLIV, 1, 1999

THE AIRY OPTICAL SPECTRUM OF A TRANSPARENT COLLOID SUSPENSION USED TO CHARACTERIZE ITS MICROSCOPICALLY STRUCTURE

CONSTANTIN DĂNCIULESCU*

ABSTRACT. This article offers a modality to analyze the dimensions and the concentration of particles in a colloid suspension placed in a Fraunhofer-Fourier optical device.

With such device, it is possible to examine the alteration of the suspension by chemical agents.

A film of the suspension becomes a plane diffraction object in the optic device that produces a Fraunhofer-Fourier diffraction figure useful to analyze the suspension.

First, in the Fraunhofer-Fourier diffraction figure it is measured the dimension of each Airy circular spot to calculate the dimension of the adequate aperture from the object plane, that is the dimension of the adequate particle.

Then, it is measured the interfringe to calculate the concentration of particles from the suspension.

Introduction

The interaction of the radiation was studied on more than one direction. Thus, the monochromatic scattering by solid or fluid media was permitted to obtain important results about some properties of the analyzed substance.

On made measurements about the modification of the absorption coefficient, which depends on the nature of the substance. For spherical [1, 2] and non-spherical particles [3 – 7] one observed a diminution of the relative intensity with the scattering angle. The same diminution was observed on edges and roughness of particles from powders [8, 9] as well.

In the case of inhomogeneous particles the experimental results indicate a dependence of the amplitude on the scattering angle according to the theoretical results [10, 11, 12].

* University of Bucharest, Department of Physics, Carol I Blvd. No. 13, Bucharest, Romania

By quasi-elastic light scattering on aqueous solutions one obtained information about the interaction potential [13 - 16].

The interaction of the radiation with colloid or polymeric solutions required many efforts to establish the dependence of the elastic diffusion coefficient on the concentration of the solution and particles shape [17, 18].

The light scattering on thin, free and liquid films was permitted to measure the power spectrum or the time auto-correlation function of the intensity of scattered light [19] and establish the thermal conductivity, the hydrodynamic velocity gradient [20 – 24].

Another interaction area of the radiation with the substance is to estimate the average dimension, the orientation, the scattering degree and the concentration of particles in a suspension by measuring the dimension of Airy circular spots and the distance between them in the spectral plane.

Theoretical consideration

The theoretical support of this physical analysis method of colloid suspensions is the diffraction in parallel, monochromatic and coherent light, represented by the Fraunhofer approximation [25].

The diffraction object, characterized by a plane distribution function, *f(x, y)*, is alighted up by a coherent, monochromatic and parallel beam obtained from a He-Ne laser. The light field diffracted by the object, *f'(x', y')*, is recorded in the image focal plane of a spherical lens, placed behind the object. This is given by the Fraunhofer diffraction formula [26]

$$f(x',y') = \frac{e^{ikf}}{i\lambda f}.e^{\frac{ik}{2f}\left(x'^2+y'^2\right)}.\int_O f(x,y).e^{-\frac{2\pi i}{\lambda f}(xx'+yy')}\,dx\,dy \qquad (1)$$

where λ represents the wavelength of the radiation, *f* – the focal distance of the lens and the integration is effected on the whole area *O* of the diffraction object.

This relation, (1), excepting the unimportant term placed in front of the integral, represents, in fact, the Fourier transform of the *f(x, y)* function [27]

$$F(u,v) = \int_O f(x,y).e^{-2\pi i(ux+vy)}dx.dy \qquad (2)$$

estimated at the frequencies:

$$u = \frac{x'}{\lambda f} \quad ; \quad v = \frac{y'}{\lambda f} \qquad (3)$$

Therefore, the light spectrum recorded in the image focal plane representes the Fraunhofer-Fourier diffraction spectrum, the spherical lens is the Fourier operator and its image focal plane is the spectral or Fourier plane, (see Fig. 1).

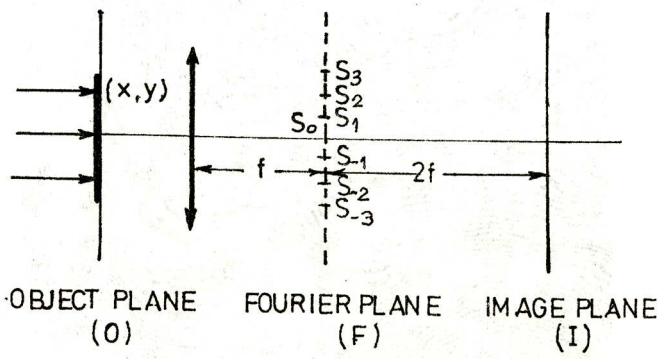

Fig. 1. The optical configuration to obtain the Fraunhofer-Fourier spectrum of a plane diffraction object.

For example, if the diffraction object is a transparency with an amplitude transmittance having a rectangle variation, the diffraction spectrum contains succesive maxima with equal distance between them, named interfinge, *i*,

$$i = \frac{\lambda f}{d} \tag{4}$$

where *d* is the distance between two consecutive slits. Measuring with precision the interfringe *i* and knowing λ and *f* it is possible to calculate the constant *d*.

Usually, maxima of order 2, 3, … are negligible given the central and the first order maximum, specially the transparency has an amplitude transmittance varying cosinusoidally.

If the diffraction object is obtained by the superposition of more rectangular diffraction gratings with different orientations, (see Fig. 2), in the spectral plane is obtained a central maximum surrounded by first order maxima pairs for each diffraction grating, (see Fig. 3).

By analysing of this spectrum it may obtained information about dimensions, orientations in the space of the recatngular diffraction object gratings.

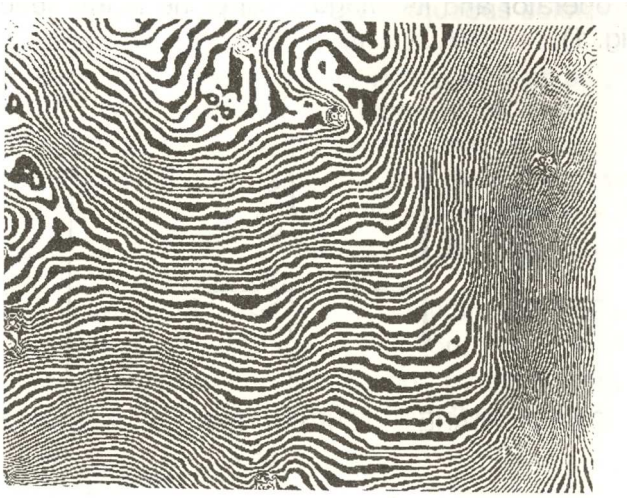

Fig. 2. A plane diffraction of more rectangular diffraction gratings with different orientations.

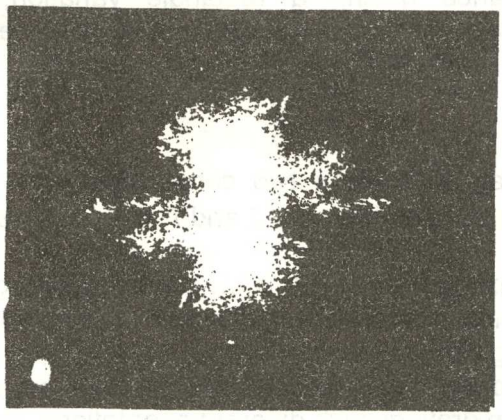

Fig. 3. The Fraunhofer-Fourier diffraction spectrum of more rectangular diffraction gratings with different orientations.

If in the diffraction object the rectangular diffraction gratings are replaced by circular apertures, each aperture produces in the spectrum plane a such intensity of light distribution:

$$I(R') = I_o \left[\frac{2J_1\left(\frac{2\pi R}{\lambda f} R'\right)}{\left(\frac{2\pi R}{\lambda f} R'\right)} \right]^2 \quad (5)$$

where *R* representes the aperture radius from the object plane, *R'* – the radius of Airy diffraction ring from the spectral plane and $J_1(\alpha)/\alpha$ is Bessel I-sinc function [26, 27]. Given the sinc function to this function the principal maximum is much more intense and much more wide than secondary maxima. That in why the entire light field is particularly produced by the Airy principal maxima that correspond to each aperture from the object plane.

The measuring of the intensity in the spectral plane allowed, in the base of the relation (5), the calculating of the particles dimension from a solution and the concentration of these particles in the solution [15, 17].

By analysing of the Bessel I-sinc function it is observed that the width of the principal maximum is:

$$\alpha = 2.1{,}22\,\pi = 2{,}44\,\pi \quad (6)$$

where, in the base of the relation (5):

$$\alpha = \frac{2\pi R}{\lambda f} R' \quad (7)$$

From these two relations it is obtained the relationship between each principal maximum diameter, *D'*, of the Airy diffraction figure and the diameter, *D*, of the adequate circular aperture:

$$D' = \frac{\lambda f}{\pi D}.\alpha = 2{,}44.\frac{\lambda f}{D} \quad (8)$$

Using the relation (8), it is possible to determinate the diameter of a circular aperture from the object plane if is measured the diameter of the adequate Airy circular spot from the spectral plane.

This idee representes the base of the next method what is used to determine the dimensions of particles from a solution as well as the concentration of this solution.

The experimental device

The optical diffraction spectrum is obtained with an experimental device that is based on the optical configuration presented in the Fig. 1.

The beam produced by a laser source is expanded by a circular microslit (1) and made parallel by a condenser (2), (see Fig. 4).

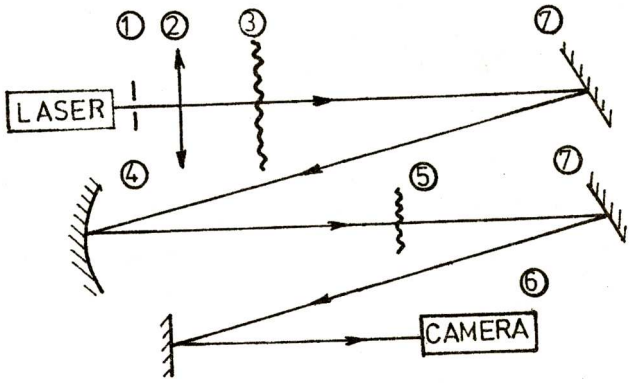

Fig. 4. The experimental device to produce the optical spectrum using a He-Ne laser source (40 mW output power).

In the spectral plane (5) of the convergent lens or a spherical mirror (4) is obtained the optical spectrum of a diffraction object placed in the plane (3). The spectrum may be analysed directly or, by help of a TV Camera on a computer or a Monitor.

The experimental research of colloid suspensions

For analysing the structure of a colloid suspension is necessary the suspension to be characterized by a optical transparency compatible with the optical system and must be stable during the analysis.

On a thin and plane slide of glass, about 1 mm, one lays a thin layer of suspension. The slide with the layer becomes a diffraction object for the experimental device used [28, 29].

If particles that exists in the suspension have the dimensions under the minimum dimension when the diffraction may be, the diffraction figure recorded in the spectral plane does not include elements which may characterize the structure of the suspension. The same situation takes place if the particles in suspension may produce the diffraction but the suspension is very homogeneous, (see Fig. 5).

If the slide that contains a very homogeneous suspension, for example a feromagnetic colloid suspension, is placed in a magnetic or electric field to line up particles, the new diffraction figure contains diffraction elements, (see Fig. 6).

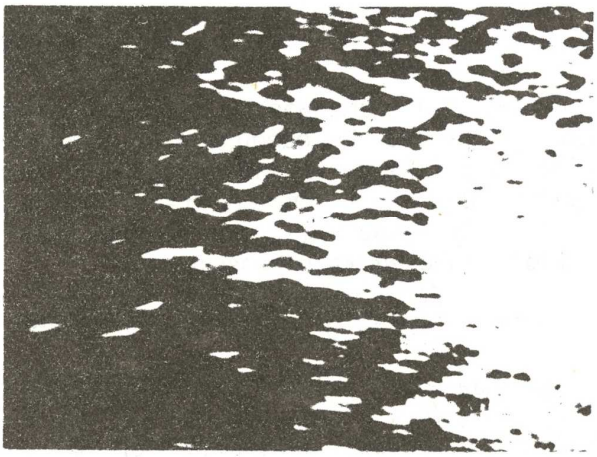

Fig. 5. The Airy diffraction spectrum of colloid suspension whose small particles are under the minimum value when the diffraction is still produced or the suspension is very homogeneous.

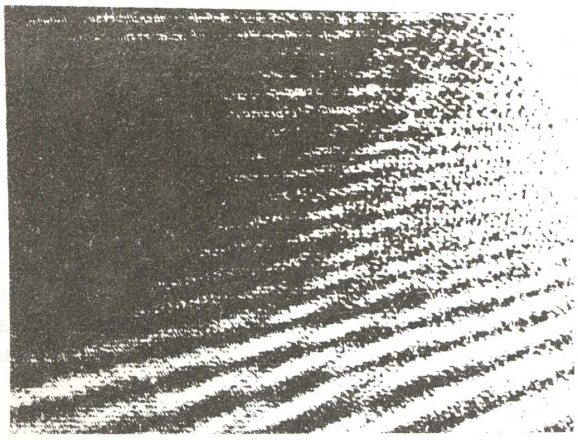

Fig. 6. The Airy diffraction spectrum of a feromagnetic colloid suspension placed in an magnetic field.

The measuring of the interfringe allows to calculate the dimensions of particles, their directions in the suspension. For the feromagnetic colloid suspension spectrum, the measured interfringe is about: $i = 3\ mm$. Because the laser wavelength is $\lambda = 6328\ Å$ and the focal distance of the Fourier

lens is *f = 1 m*, it is obtained, for the distance between two particles, the value: *d = 0,21 mm*, (see Fig. 6).

But, usually, in the feromagnetic colloid suspension the particles have an elliptical shape, then the adequate spots from the spectral plane have elliptical shape, too. Thus, it is measured the axisis of an elliptical spot from the spectral plane, it is obtained: *a'= 10 mm* and *b'= 2 mm*, respectively. Using the relation (8), are calculated the axisis of the adequate particle from the colloid suspension:

$$a = 2{,}44.\frac{\lambda f}{a'} = 2{,}44.\frac{0{,}6328.1000}{10}\ \mu m = 154\ \mu m$$

$$b = 2{,}44.\frac{\lambda f}{b'} = 2{,}44.\frac{0{,}6328.1000}{2}\ \mu m = 772\ \mu m$$

If are known the dimensions of the object plane; $\Delta x \times \Delta y = 24 \times 36 mm^2$, it is possible to calculate the number of apertures from this plane:

$$N = N_x.N_y = \frac{\Delta x}{i_x}.\frac{\Delta y}{i_y} = \frac{\Delta x}{d+a}.\frac{\Delta y}{d+b}$$

where i_x and i_y are the interfringes on the *ox* direction and the *oy* direction, respectively. Replacing the numerical values, it is obtained for *N*:

$$N = \frac{24\ mm}{0{,}21\ mm + 0{,}154\ mm}.\frac{36\ mm}{0{,}21\ mm + 0{,}772\ mm} \cong 2417\ \ particles$$

The superficial concentration, that is the number of particles on the unit of the surface, is:

$$c = \frac{N}{\Delta x.\Delta y} = \frac{1}{i_x}.\frac{1}{i_y} = \frac{1}{0{,}364}.\frac{1}{0{,}982}.\frac{particles}{mm^2} \cong 3\ \frac{particles}{mm^2}$$

These results are in concordance with measurements obtained by other methods [30, 31, 32], the reproductibility of results is around 98%.

Conclusions

This analysis colloid suspension method may be used to establish the dimensions of the particles in a suspension, their concentration, or to establish if the particles in the suspension, after the action of a chemical or physical agent, were modified by splitting or union.

REFERENCES

1. S. Asano, G. Yamamoto – Appl. Opt. **14**, 29, (1975).
2. C. R. Berry – J. O. S. A. **52**, 888 – 895, (1962).
3. J. M. Greenberg – J. Appl. Phys. **31**, 82, (1960).
4. M. Wolf – Appl. Opt. **14**, 1395, (1975).
5. C. Aquista – Appl. Opt. **11**, 2932, (1976).
6. D. R. Huffman – Adv. in Phys. **26**, 129, (1977).
7. R. H. Zernl, R. H. Griese, K. Weiss – Appl. Opt. **16**, 777, (1977).
8. J. R. Aronson, A. G. Emslie – Appl. Opt. **18**, 2622, (1979).
9. H. M. Fijnaut, J. G. H. Josten – J. Chem. Phys. **69**, 1022, (1978).
10. J. L. Anderson, C. C. Reed – J. Chem. Phys. **64**, 3240, (1976).
11. B. J. Ackerson – J. Chem. Phys. **69**, 684, (1978).
12. W. Hess, R. Klein – Physica, **95A**, 208, (1978).
13. R. Tertian – Chim. An. **51**, 525, (1969).
14. R. Tertian – Spectrochim. Acta, **24B**, 447, (1969).
15. B. U. Felderhof – J. Phys. Appl. **11**, 929, (1978).
16. G. A. Aniansson – J. Phys. Chem. **82**, 2805, (1978).
17. J. Cornillault – Appl. Opt. **11**, 256, (1972).
18. C. Dodge, W. L. Anderson – J. O. S. A. **64**, 544, (1974).
19. J. A. Mann Jr., K. Caufield, G. Gulden – J. O. S. A. **61**, 76, (1971).
20. H. Eichler, G. Salje, H. Sthal – J. Appl. Phys. **44**, 5383, (1973).
21. D. W. Pohl, S. E. Scharz, V. Irmiger – Phys. Rev. Lett. **31**, 32, (1973).
22. F. Rondelez, H. Hervet, W. Urbach – Phys. Rev. Lett. **41**, 1058, (1978).
23. J. P. Bonn, C. Allain, P. Lallemand – Phys. Rev. Lett. **43**, 199, (1979).
24. L. Ricard, J. Prost – J. de Phys. **40C**, 3, (1979).
25. N. Born, E. Wolf – *Principles of Optics*, Pergamon Press, London, 1959.
26. M. Francon – *Modern Applications of Physical Optics*, Wiley, New York, 1963.

27. J. W. Goodman – *Introduction to Fourier Optics*, McGraw-Hill Book Company, New York, 1968.

28. O. S. Heavens – *Optical Properties of Thin Solid Films*, Butterworth, London, 1955.

29. A. J. Hole – *The Interference Microscope in Biological Research*, Livingstone, 1958.

30. F. V. Lisovski, F. Mansvetova – Photonics Optoel. **2(3**), 103, (1994).

31. R. P. Garten, H. W. Werner – Anal. Chim. Acta, **297**, (1994).

32. P. Toerek, P. Varga, G. R. Booker – J. O. S. A. **12(10)**, 2136, (1995).

STUDIA UNIVERSITATIS BABEŞ-BOLYAI, PHYSICA, XLIV, 1, 1999

ULTRASONIC STUDY OF VISCOSITIES IN BINARY LIQUID SYSTEMS 1,1,2,2 TETRACHLOROETHANE – BENZENE AND 1,2 DICHLOROETHANE - TOLUENE

ILEANA LENART*, CORINA L. TOMA*

ABSTRACT. The ultrasonic method in the study of liquids' viscosity is based on the measurement of attenuation constant by absorption and the propagation velocity of ultrasonic wave in the medium, as well as the dynamic viscosity and the liquid density. The liquid binary systems of 1,1,2,2 tetrachloroethane – benzene and 1,2 dichloroethane – toluene have been studied. Experimental data made possible the computation of the dynamic viscosity, the relaxation constant at compression, the volumic viscosity and the viscosity relaxation times. The variation of these parameters with temperature and concentration is interpreted on the basis of intermolecular interaction modification within the liquid mixtures.

Theory

The liquid, in which ultrasonic wave propagates, is submitted to shear and compression deformations. The compressibility of the liquid can not be neglected in the case of rapid and strong pressure variations caused by wave propagation. The resistance of the liquid to these deformations is characterized by the dynamic and volumic viscosity coefficients.

The Navier-Stokes' dynamic equations, in vectorial form [1] is:

$$\frac{D\vec{V}}{Dt} = \vec{f} - \frac{1}{\rho}\nabla p + \frac{\eta}{\rho}\Delta\vec{v} + \frac{1}{\rho}\left(\frac{\eta}{3} + \eta_V\right)\nabla\left(\nabla\vec{v}\right) \qquad (1)$$

where: η is the dynamic viscosity coefficient;

η_V is the volumic viscosity coefficient;

$\frac{D\vec{v}}{Dt}$ is the substantial derivative of the velocity;

p is the pressure;

ρ is the density;

f is the force corresponding to the masse unit.

* Faculty of Physics, "Babeş – Bolyai" University, Cluj – Napoca, Romania

While for the measurement of the η coefficient there are many experimental methods, for the determination of the η_V coefficient only the ultrasonic method is available. This method is based on the measurement of the attenuation constant by absorption and the propagation velocity of ultrasonic wave in the liquid.

The Frenkel's visco-elastique theory considers the dynamic and volumic viscosity effects with additional properties upon the acoustical energy, which is carried by ultrasonic wave in the liquid. The theory establishes the following expression for attenuation constant α by absorption:

$$\alpha = \alpha_d + \alpha_V = \frac{8\pi^2 f^2}{3\rho c^3}\eta + \frac{2\pi^2 f^2}{\rho c^3}\eta_V \tag{2}$$

where: α_d is the attenuation constant by dynamic viscosity absorption;

α_V is the attenuation constant by volumic viscosity absorption;

c is the propagation velocity;

f is the frequency of the ultrasound.

The evaluation of relaxation constant at compression (α_V), using relation (2):

$$\alpha_V = \alpha - \alpha_d = \frac{2\pi^2 f^2}{\rho c^3}\eta_V \tag{3}$$

allows the determination of volumic viscosity coefficient (η_V):

$$\eta_V = \frac{\rho c^3}{2\pi^2 f^2}\alpha_V \tag{4}$$

and of the determination of viscosity relaxation time (τ_V):

$$\tau_V = \frac{2\eta + \eta_V}{\rho c^2} \tag{5}$$

In the case of a liquid mixture, the knowledge about the variation of the above mentioned parameters (2 ÷ 5) with the temperature and concentration facilitates a qualitative estimation of the intermolecular interactions in the mixture [2,3,4,5].

Experimental Section

The binary liquid systems 1,1,2,2,tetrachloroethane ($C_2H_2Cl_4$) – benzene (C_6H_6) and 1,2 dichloroethane ($C_2H_4Cl_2$) – toluene (C_7H_8) were studied at different concentrations from molar fraction 0 to 1 and at the temperatures of 274 K, 303 K and 313 K.

We measured by experimental means the attenuation constant by absorption, the ultrasonic propagation velocity, the density and the coefficient of dynamic viscosity of pure components and their mixtures.

The attenuation constant by absorption was measured using the impulse method at fixed distance and at a frequency of 8 MHz.

The propagation velocity was obtained by means of the diffraction method of monochromatic yellow light (5893 Å). This light was perpendicular on an ultrasonic beam of 4 MHz.

Density was measured using a picnometer with an accuracy of ±0.02%.

The coefficient of dynamic viscosity was determined by an Arhhenius viscometer with an accuracy of ±0.1%.

Results

Figures 1a and 1b show the variation with the concentration of α_d / f^2 parameter at 294 K, computed from dynamic viscosity data, and the variation of α / f^2 experimental parameter at three different temperatures: 294 K, 303 K and 313 K.

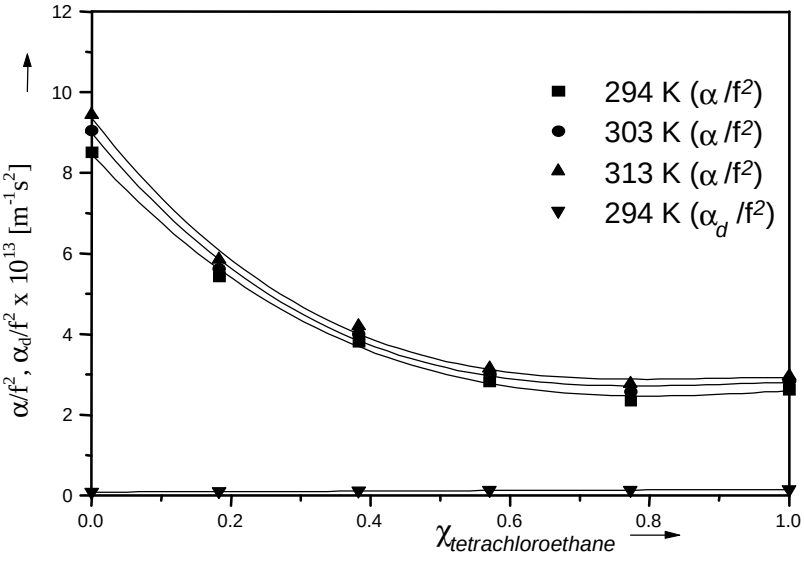

Fig. 1a. Variation of α/f^2 and α_d/f^2 with concentration

The temperature coefficient of the absorption is positive for both variations. Because of the very low value of the coefficient in $\alpha_d / f^2 = f(\chi)$ case, this variation was represented only at 294 K. Experimental values of absorption are higher than calculated values from the dynamic viscosity for both mixtures. Since in toluene the values of absorption are low, fig. 1.b, representing dichloroethane – toluene system, uses a scale for ordinate that is 13 times larger than the one in fig.1.a. Therefore, it is obvious that the comparative analysis of the curves in fig.1 becomes more difficult.

The comparative study of experimental absorption values, at 294 K, in pure components and in both mixtures, can be made observing in fig.2. It has been found that the experimental absorption is higher in benzene than in toluene and also in 1,1,2,2 tetrachloroethane than in 1,2 dichloroethane. In the mixture with benzene, the absorption decreases as 1,1,2,2 tetrachloroethane concentration decreases. In the other mixture, the absorption increases while 1,2 dichloroethane concentration increases.

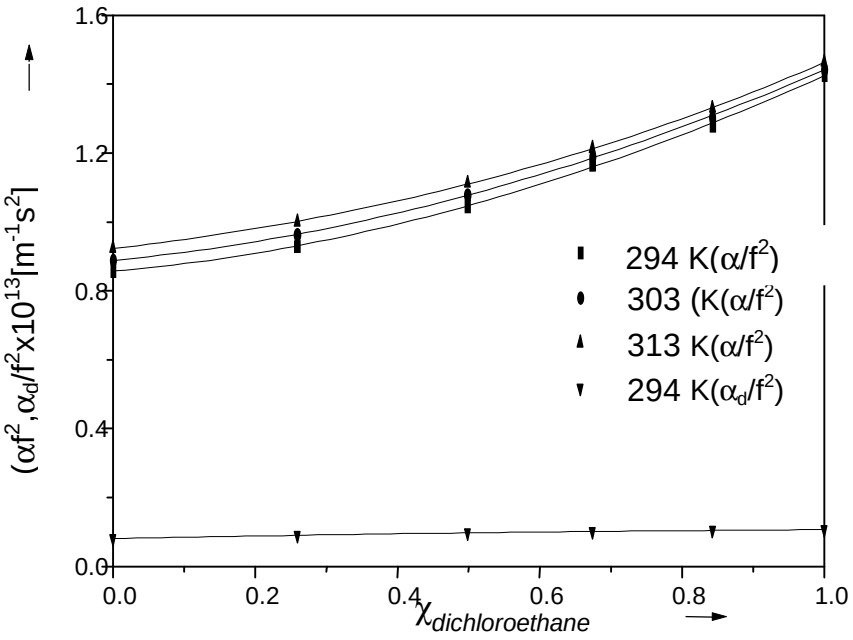

Fig. 1b. Variation of α/f^2 and α_d/f^2 with concentration

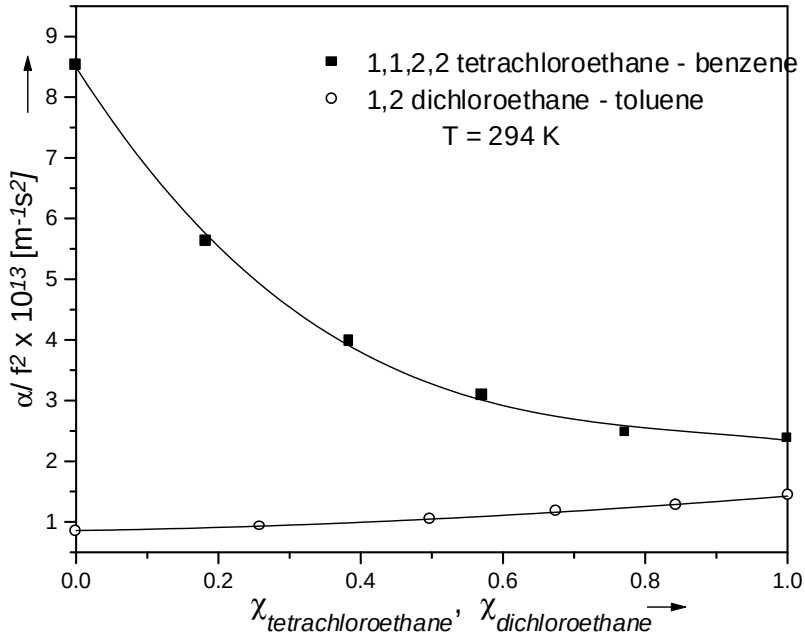

Fig. 2. Variation of α/f^2 with concentration

The absorption due to the molecular processes of relaxation, which occur in compression, is estimated by means of relation (3). For both systems, the relaxation absorption at compression is plotted against the concentration in fig. 3a and 3b.

The curves present a behaviour similar with that of experimental absorption. The temperature coefficient of relaxation absorption at compression is positive.

The experimental values of the absorption, in the studied systems, show negative deviations from the additivity on the entire concentration range. The variation of excess experimental absorption with concentration is represented at three different temperatures in fig. 4a and 4b. Each curve has a minimum. The value and the position of this minimum vary with the temperature in case of a binary system and when the temperature is constant, they depend on the nature of the system.

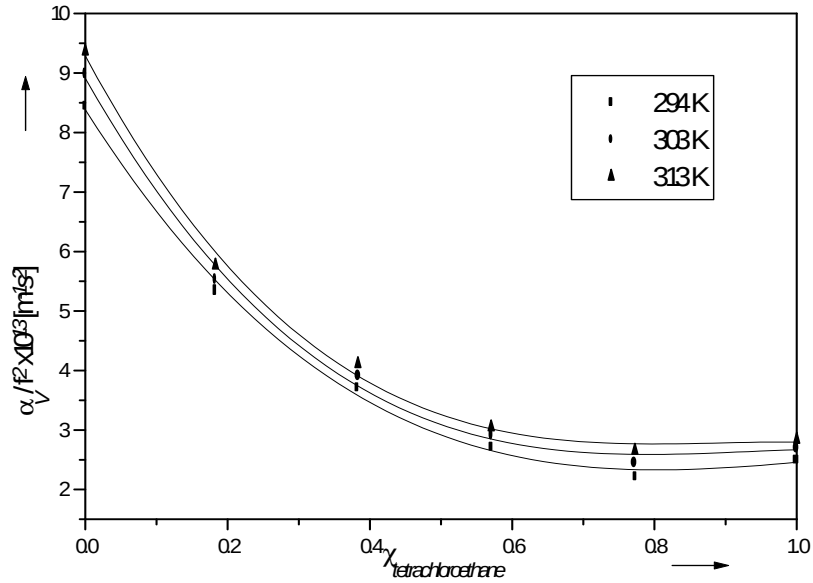

Fig. 3a. Variation of α_v/f^2 with concentration

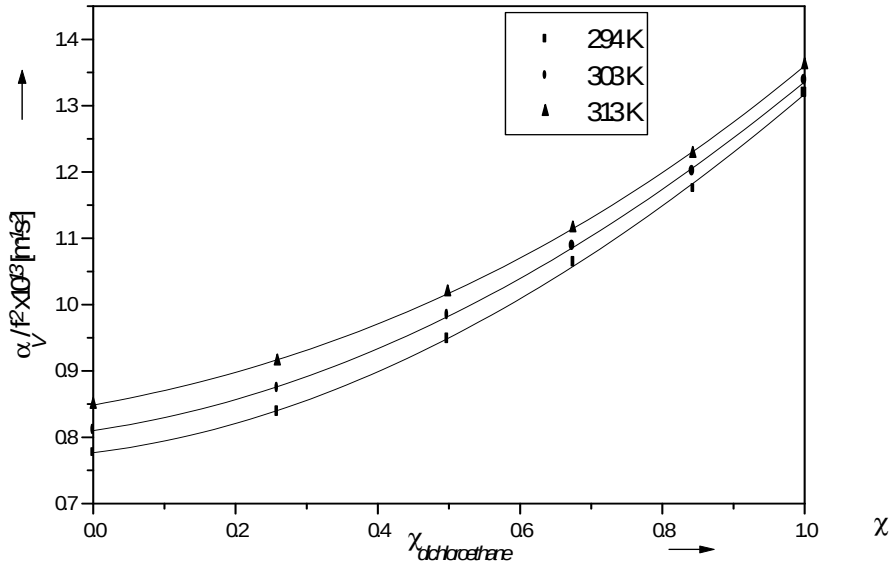

Fig. 3b. Variation of α_v/f^2 with concentration

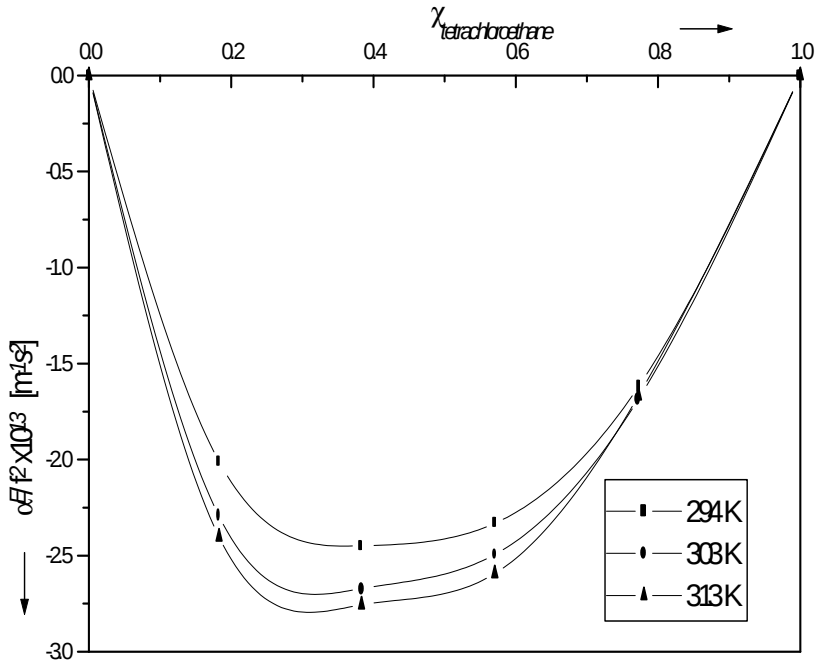

Fig. 4a. Variation of α^E/f^2 with concentration

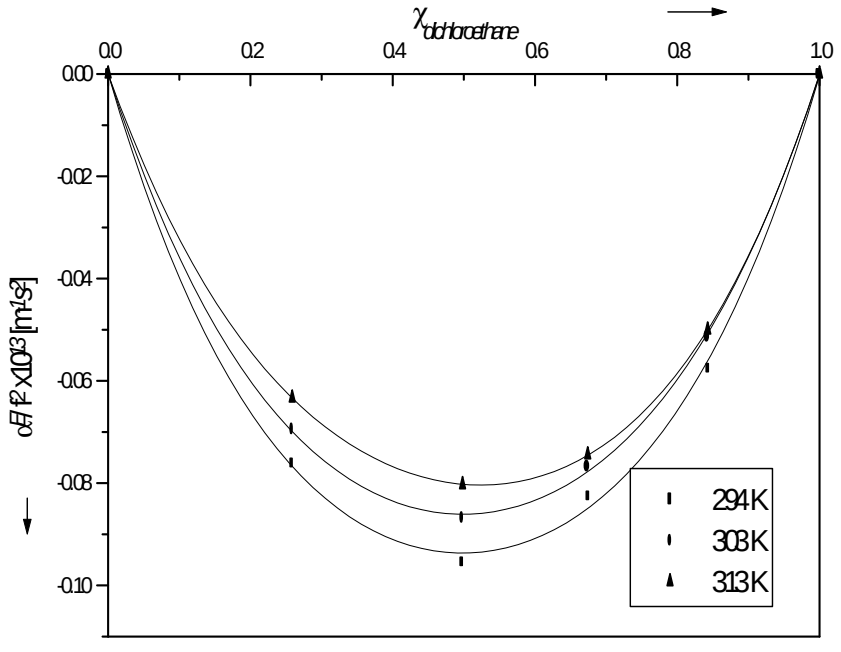

Fig. 4b. Variation of α^E/f^2 with concentration

The Table 1 summarizes the values of dynamic viscosity coefficient, experimentally determined, the values of volumic viscosity, calculated from ultrasonic data using relation (4), and the values viscosity relaxation times, estimated through relation (5).

In the case of pure components and mixtures, the values of the dynamic viscosity coefficient are lower in comparison with those of volumic viscosities. The ratio is about 150 for benzene and varies between 25 and 23 in the case of 1,1,2,2,tetrachloroethane, toluene and 1,2 dichloroethane. The viscosity relaxation time is in the range of 10^{-11}s.

DISCUSSIONS

The interpretation of the presented results is based on the correlation of the nature and intensity of the intermolecular interactions in the liquids with the relaxation processes of viscosity. These processes accompany the reequilibration of the system, which is disturbed by the ultrasonic wave. The intermolecular interactions limit the relaxation possibility.

Table 1. Values of η, η_V and τ in the two studied systems

$C_2H_2Cl_4 - C_6H_6$	T	$\chi_{tetrachloroethane}$					
	[K]	0.000	0.183	0.383	0.571	0.773	1.000
$\eta \times 10^3$ [Nsm^{-2}]	294	0.65	0.780	0.93	1.08	1.24	1.43
	303	0.57	0.669	0.79	0.91	1.06	1.24
	313	0.49	0.572	0.66	0.76	0.89	1.04
$\eta_V \times 10^3$ [Nsm^{-2}]	294	85.20	55.45	42.29	36.72	30.08	35.43
	303	80.62	51.77	40.13	31.25	25.48	31.18
	313	77.46	47.70	37.62	25.89	20.87	26.08
$\tau \times 10^{11}$ [s]	294	5.67	3.47	2.51	2.09	1.63	1.77
	303	5.79	3.48	2.54	1.89	1.47	1.65
	313	6.07	3.48	2.57	1.69	1.30	1.49
$C_2H_4Cl_2 - C_7H_8$	T	$\chi_{dichloroethane}$					
	[K]	0.000	0.259	0.498	0.674	0.843	1.000
$\eta \times 10^3$ [Nsm^{-2}]	294	0.60	0.68	0.75	0.80	0.85	0.89
	303	0.53	0.60	0.65	0.71	0.76	0.80
	313	0.45	0.51	0.57	0.62	0.66	0.70
$\eta_V \times 10^3$ [Nsm^{-2}]	294	7.79	8.43	9.73	11.21	12.77	14.78
	303	7.35	7.93	9.10	10.36	11.80	13.63
	313	6.86	7.37	8.38	9.43	10.75	12.45
$\tau \times 10^{11}$ [s]	294	0.60	0.63	0.70	0.76	0.82	0.91
	303	0.60	0.64	0.69	0.75	0.81	0.89
	313	0.60	0.63	0.69	0.74	0.80	0.87

The studied binary systems consist of components with different structural properties. Benzene has symmetrical molecules with a plane hexagonal configuration and dipole moment about 0 D. Only van der Waals dispersion forces act between these molecules. The a_y parameter [6], which is a measure of intermolecular interaction intensity, has the value a_y = 998 $kg^{-1}m^5s^{-2}$ for benzene. This parameter is calculated with the relation:

$$a_y = \frac{c^2}{2\rho}.$$

Toluene is a substitute of benzene with a single methyl group. Its molecules have a dipole moment μ = 0.39 D [6] because of their non-symmetrical structure. In toluene besides the Van der Waals dispersion forces, orientation forces act too as a result of the dipole moment. The increase intermolecular interaction intensity is illustrated by the higher value of a_y parameter, a_y = 1014 $kg^{-1}m^5s^{-2}$, than that in benzene. Concerning the contribution of orientation, dispersion and induction components to the van der Waals forces, it depends on the two properties of molecules: the polarity, characterized by the dipole moment μ and deformability, characterized by the polarizability α_e. When their values are known, the calculation of interaction potential energy and van der Waals forces respectively are possible [7].

The higher values of experimental and volumic absorption, compression viscosity and viscosity relaxation time in benzene in comparison with toluene, values which are correlated with intermolecular interactions intensity, are in agreement with the sense of the modification of: a_y parameter from 998 $kg^{-1}m^5s^{-2}$ in benzene to 1014 $kg^{-1}m^5s^{-2}$ in toluene, dipole moment μ from 0.08 D in benzene to 0.39 D in toluene and polarizability from 1.05 x 10^{-29} m^3 in benzene to 1.25 x 10^{-29} m^3 in toluene.

The other components of the studied systems, the 1,1,2,2 tetrachloroethane and 1,2 dichloroethane are derivates of ethane with four and two chlorine atoms respectively. Their molecules are polar with permanent dipole moment, which increases from $\mu_{tetrachloroethane}$ = 1.97 D to $\mu_{dichloroethane}$ =2.60 D. This increase is accompanied by a decrease of polarizability from $\alpha_{e\ tetrachloroethane}$ = 1.19 x 10^{-29} m^3 to $\alpha_{e\ dichloroethane}$ =0.84 x 10^{-29} m^3. Between the molecules of 1,1,2,2 tetrachloroethane and 1,2 dichloroethane dispersion and orientation Van der Waals forces act. Their intensity increases from 1,1,2,2 tetrachloroethane to 1,2 dichloroethane in agreement with the a_y parameter ($a_{y\ tetrachloroethane}$ = 419 $kg^{-1}m^5s^{-2}$, $a_{y\ dichloroethane}$ = 584 $kg^{-1}m^5s^{-2}$) and with values of α, α_V, η and τ_V, which are higher in 1,1,2,2 tetrachloroethane (see Table 1).

The experimental absorption (α) includes the effect of dynamic and volumic viscosity, meanwhile, the calculated absorption (α_d) includes only the

effect of dynamic viscosity. In the case of pure studied components benzene, toluene, 1,1,2,2 tetrachloroethane and 1,2 dichloroethane, the ratio α/α_d has the values: 100, 20, 19.7 and 17. In agreement with Pinkerton's classification scheme of liquids, based on the value of the previous ratio, all these four components of the studied systems belong to the group of unassociated liquids, which present a positive temperature coefficient.

In binary mixtures, between the molecules of the first component, the second one and also between the molecules of the two mixture components occur interactions. The preponderance of one or another of these interactions varies with the concentration. These structural considerations regarding the binary mixtures explain the deviation of experimental absorption from additional rule. The negative deviation of the studied systems, correlated with the intermolecular interactions intensity suggest that, over the entire range of concentration, the interactions are stronger in mixtures than in pure components.

REFERENCES

1. Constantinescu I.V.N., Dinamica fluidelor vascoase in regim laminar, Ed. Tehnica, Bucuresti, 1987.
2. Narasimham A. V., Seshadri A. T., Indian J. Phys., 66B (1), (1992), 41.
3. Venkatesulu D., Venkatesulu P., Prabhakara Rao M.V., Chem. Eng. Data, 42 (2), (1997), 365.
4. Srinivasa Rao, Subha M.C.S., Narayana Swami G., Acustica, 75, (1991), 86.
5. Ravichandran G, Adilakshmi S., Srinivasa Rao A., Nambinarayanan T. K., Acustica, 75, (1991), 224.
6. Melkonean L. G., Scorost' ultrasvuka i mejmolecularnoe pritiajenie v binarnih jidkih smesiah obrazninscih himicescoe soedinenie- in the volume -Primenie ultrazvuk k issledovanie vescestvo, red. V.F. Nozdrev, B.B. Kudriavțev, Mopi, Moscow,1956.
7. Zsako I., Chimie fizica – Structura atomilor si moleculelor, Ed. Didactica si Pedagogica, Bucuresti, 1973.
8. Murgulescu I. G., Sahini V. E., Introducere in chimia fizica, vol. I,2, Ed. Academiei R.S.R., Bucuresti, 1978.

MOLECULAR DYNAMICS SIMULATION OF SELF-DIFFUSION IN BINARY SOFT SPHERE MIXTURES

MIRCEA ANDRECUT*

ABSTRACT. The self-diffusion coefficients in supercooled binary mixtures of soft-spheres are calculated using the constant temperature molecular dynamics technique. The temperature dependence of the self-diffusion coefficients shows a smooth diffusive to non-diffusive transition predicted by the stochastic trapping model for the glass transition proposed by Odagaki and Hiwatary (Phys. Rev. A 43 (1991) 1103).

Introduction

The system of binary mixtures of soft-spheres with differe ameters and masses can be regarded as a simple model of glass-formin loys. Usually, such a mixture is build up from N_1 atoms of mass m_1 ar ameter σ_1 and N_2 atoms of mass m_2 and diameter σ_2 in a volume V teracting through the repulsive soft sphere potential:

$$V_{\alpha\beta} = \varepsilon\left(\frac{\sigma_{\alpha\beta}}{r}\right)^{12}, \qquad (1$$

here

$$\sigma_{\alpha\beta} = \frac{\sigma_\alpha + \sigma_\beta}{2}, \qquad (2$$

nd $\alpha, \beta = 1, 2$ denote species indices.

The advantage of this simple model consists in its scalin roperties, namely the model can be described using only one effecti oupling parameter, assuming that $x_1 = N_1/N$ $(N = N_1 + N_2)$ and σ_2/σ

enotes the reduced number density, and

$$T^* = k_B T/\varepsilon \qquad (5$$

the reduced temperature.

According to the conformal solution theory [2], it results that th operties of the mixture can be reproduced by those of an equivalent one mponent system made up of spheres with an effective diameter define

$$\sigma_{eff}^3 = \sum_\alpha \sum_\beta x_\alpha x_\beta \sigma_{\alpha\beta}^3 \,. \qquad (6$$

ne corresponding effective coupling parameter is in this case given by

$$\Gamma_{eff} = \Gamma\left(\sigma_{eff}/\sigma_1\right)^3. \qquad (7$$

his approximation makes it possible to define any thermodynamic quilibrium state as a function of the single coupling constant Γ_{eff}.

Many molecular dynamics simulations of binary mixtures of sof pheres have been reported on this model [3, 4, 5]. The obtained resul ave shown that the liquid-glass transition is sharp and occurs arour $_{eff} \approx 1.5$. Almost all reported results have been obtained using th onstant-energy simulations using the Gear algorithm in 7th order forc presentation [6] and Kubo relations for the self-diffusion coefficients [2 ere, we describe a molecular-dynamics algorithm which gives simil sults. The algorithm is based on a simple quenching method, after whic e system is coupled to a Nosé-Hoover thermostat [7, 8] in order to b quilibrated at a desired temperature. The self-diffusion coefficients a en determined using the Einstein method [2] at constant temperatu onstant kinetic energy).

Description of the algorithm

Our molecular dynamics simulations are performed in a box olume $V = L^3$, using periodic boundary conditions [9]. The initial partic oordinates are chosen from a cubic crystal lattice to prevent excessiv olecule overlap, and therefore catastrophically large forces. Also, in ord

following

$$V_{\alpha\beta} = \varepsilon\left(\frac{\sigma_{\alpha\beta}}{r+\delta r_0}\right)^{12}, \tag{8}$$

here $\delta r_0/\sigma_1 = 0.001 << 1$ is a small positive constant. This modification is uivalent with the consideration of a very small hard core in the soft here.

The initial velocities are chosen from a Gaussian distributed random mber generator giving a Maxwell-Boltzmann distribution of velocities. e Gaussian distributed random number generator is constructed using e Box-Muller method [10]. We give here a short description of the aussian distributed random number generator. Consider the nsformation between two uniform distributed variables (ξ_1, ξ_2) on the erval $(0, 1)$, and two quantities (η_1, η_2),

$$\eta_1 = \sqrt{-2\ln\xi_1}\cos(2\pi\xi_2),$$

$$\eta_2 = \sqrt{-2\ln\xi_1}\sin(2\pi\xi_2), \tag{9}$$

equivalently

$$\xi_1 = \exp\left[-\frac{1}{2}\left(\eta_1^2+\eta_2^2\right)\right],$$

$$\xi_2 = \frac{1}{2\pi}\arctan\left(\frac{\eta_2}{\eta_1}\right). \tag{10}$$

e Jacobian of the transformation is

$$\frac{\partial(\xi_1,\xi_2)}{\partial(\eta_1,\eta_2)} = -\left[\frac{1}{\sqrt{2\pi}}\exp\left(-\frac{\eta_1^2}{2}\right)\right]\left[\frac{1}{\sqrt{2\pi}}\exp\left(-\frac{\eta_2^2}{2}\right)\right] \tag{11}$$

results that the variables (η_1, η_2) are independently distributed according the normal distribution

generate three uniform distributed variables (ξ_1, ξ_2, ξ_3) on the int
$(0, 1)$;
make the transformations:

$$\eta_1 = \sqrt{-2\ln\xi_1}\cos(2\pi\xi_2),$$

$$\eta_2 = \sqrt{-2\ln\xi_1}\sin(2\pi\xi_2),$$

$$\eta_3 = \sqrt{-2\ln\xi_1}\sin(2\pi\xi_3).$$

To prevent the translation of the system, which can give ris
spurious results, the net momentum of the system is set to zero a
beginning of the simulation. This procedure is implemented as follow

the beginning of the simulation the velocities $\{\vec{v}_i, i = 1, ..., N\}$
generated using the algorithm described by eqs. (13). The total mome
of the system is evaluated, $\vec{P} = \sum_i m_i \vec{v}_i$, and then for each molecul
velocity is calculated using the following transformation:

$$\vec{v}_i \to \vec{v}_i - \frac{1}{Nm_1}\vec{P}.$$

The transformation (14) gives a zero initial momentum and do not ch
the Maxwell-Boltzamann distribution of the system. Finally, the velociti
the spheres are scaled using the transformation $\vec{v}_i \to \alpha\vec{v}_i$, in such way
the dynamics of the system start at the desired temperature (k
energy).

Equilibrium liquid configurations are obtained by melting the
crystal configuration. The equilibrium is rapidly established by mole
collisions within (typically) 100 time steps. The microscopic time sca
chosen to be

$$\sqrt{m_1\sigma_1^2}$$

$$\frac{d\vec{v}_i}{dt} = m_i^{-1}\vec{F}_i - \eta\vec{v}_i,$$

$$\frac{d\eta}{dt} = \frac{1}{gk_BT\tau^2}\left(\sum_{i=1}^{N}\frac{m_i v_i^2}{2} - \frac{gk_BT}{2}\right). \quad (1$$

ere, $\eta(t)$ is the thermostat factor, $g = 3N$ is the number of degrees eedom, and T is the desired temperature. The time parameter, τ, is th aracteristic thermostat relaxation time. In order to minimize th ermostating mechanism this parameter was set to the value $\tau = 0.5$.

The Nosé-Hoover equations (16) are solved using the centere fference Stoermer algorithm [9]. This algorithm scans the phase spac rrectly, leading to the correct equilibrium properties with respect nergy conservation. Details on the discretisation of the Nosé-Hoov quations using the centered-difference Stoermer algorithm are given 1, 12]. The centered-difference equations for the system can be writte following:

$$\vec{v}_i(t+\Delta t/2) = \vec{v}_i(t-\Delta t/2)\frac{1-\eta(t)\Delta t/2}{1+\eta(t)\Delta t/2} + \frac{\vec{F}_i\Delta t}{m_i[1+\eta(t)\Delta t/2]},$$

$$\vec{r}_i(t+\Delta t) = \vec{r}_i(t) + \vec{v}_i(t+\Delta t/2)\Delta t,$$

$$\eta(t+\Delta t) = \eta(t) + \frac{\Delta t}{\tau^2}\left(\frac{1}{gk_BT}\sum_i m_i v_i^2(t+\Delta t/2) - 1\right). \quad (1$$

ere, $\Delta t \approx 0.05\tau$ is the time integration step and $\vec{F}_i = \sum_{j,\, j\neq i}\vec{F}_{ij}$ is the for cting on the sphere i. Following (8) it results that

$$\vec{}$$

The calculations have been carried out for the following values o
e parameters: $\sigma_2/\sigma_1 = 1.2$, $m_2/m_1 = 2$ and $x_1 = 0.5$ (the equimola
ase). The number of spheres and the reduced number density were fixed
$N = 500$ and $\rho^* = 0.733$.

Equilibrium liquid configurations are "prepared" by melting the initia
rystal configuration at a higher temperature $T^* = 1$. The equilibrium is
stablished after typically 100 time steps by integrating the Nosé-Hoove
quations.

Supercooled and glassy states are obtained by a quenchin
rocess, during which the velocities of all spheres are scaled down
ccording to the transformation $\vec{v}_i \to \alpha \vec{v}_i$, where $0 < \alpha << 1$. The
esulting change in the temperature of the system is simply obtained by the
ansformation: $T \to T' = T\alpha^2 << T$. The system is then stabilized at the
ew desired temperature T' using the Nosé-Hoover dynamics.

The self-diffusion coefficients are estimated directly from the
instein relation

$$\lim_{t\to\infty}\left\langle \left\| \vec{r}_{i\alpha}(t) - \vec{r}_{i\alpha}(0) \right\|^2 \right\rangle = \lim_{t\to\infty} \gamma_\alpha(t) = 6D_\alpha t . \qquad (19$$

he slope of the mean-square displacement $\gamma_\alpha(t)$, averaged over al
pheres of a given type, allows an accurate estimate of D_α.

The time dependence of the mean-square displacement $\gamma_\alpha(t)$ is
iven in Fig. 1, for three typical situations: (a) high temperature; (b
emperature in the vicinity of glass transition; (b) temperature
orresponding to a glassy state.

At high temperatures the behavior of $\gamma_\alpha(t)$ reaches the linea
egime rapidly. In the vicinity of glass transition, $\gamma_\alpha(t)$ exhibits a non-linea
ehavior, reaching the linear regime after a much longer time. In the glassy
tate, the self-diffusion coefficients are very small and becomes
omparable with the "noise" generated in calculations.

In Fig. 2 we give the temperature dependence of the self-diffusion
oefficients. One can see that the diffusive to non-diffusive transition is
mooth and it is located around $T^* \approx 0.16$, the corresponding effective
oupling parameter being $\Gamma_{eff} \approx 1.55$.

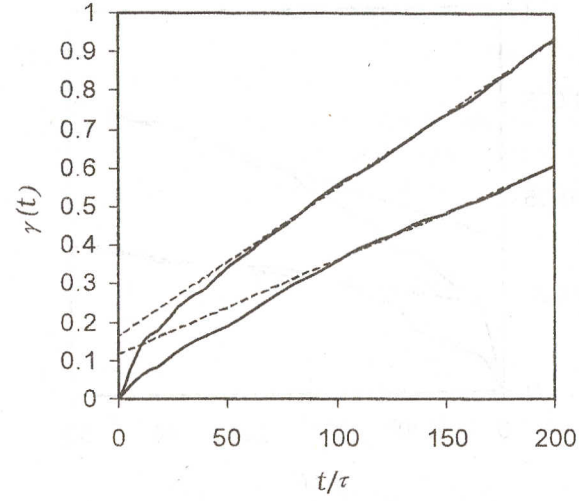

a)

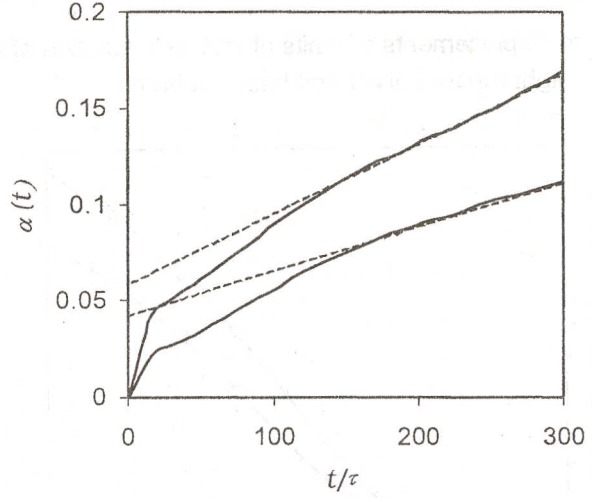

b)

Fig. 1. Mean-square displacements (in units of σ_1) as a function of time for the

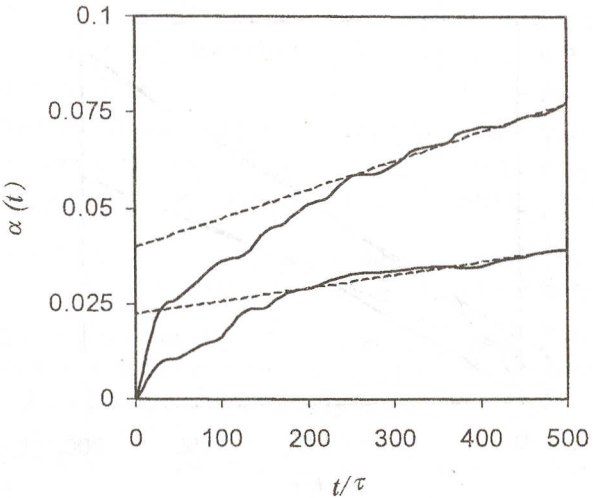

Fig. 1. Mean-square displacements (in units of σ_1) as a function of time f
light (upper curve) and heavy spheres:

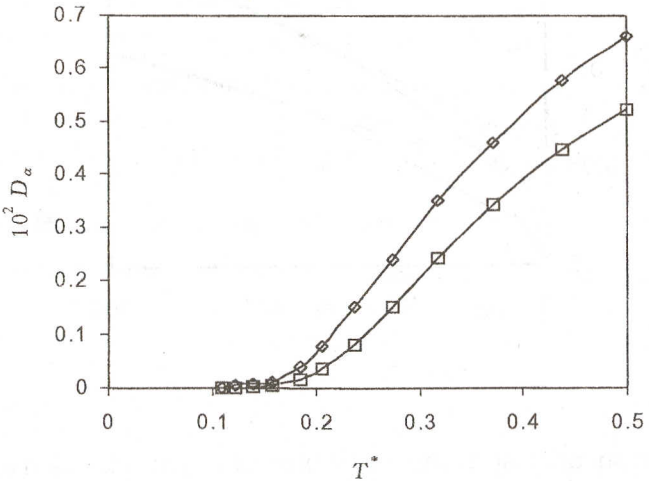

Conclusions

The obtained results are compatible with the stochastic trappin
odel for the glass transition proposed by Odagaki and Hiwatary [13, 14
5]. The model is based on a jump diffusion model with a stochasti
quation for the tracer atom and with the power-law form of the jump-rat
stribution function. The model predicts an anomalous diffusion followe
y a transition from the diffusive to the non-diffusive regime.

REFERENCES

S. Nosé, F. Yonezawa, *Solid State Commun.* **56** (1985) 1005.

J. P. Hansen, I. R. McDonald, *Theory of Simple Liquids* (Academic Pres
London 1986).

B. Bernu, Y. Hiwatari, J. P. Hansen, *J. Phys. C: Solid State Phys.* 1
(1985) L371.

B. Bernu, J. P. Hansen, Y. Hiwatary, G. Pastore, *Phys. Rev. A* **36** (198
4891.

Y. Hiwatari, H. Miyagawa, *J. Non-Cryst. Solids* **117/118** (1990) 862.

B. Bernu, *Physica A* **122** (1983) 129.

S. Nosé, *J. Chem. Phys.* **81** (1984) 511.

W. G. Hoover, *Phys. Rev. A* **31** (1984) 1695.

D. M. Heyes, *The Liquid State, Applications of Molecular Simulations* (Wile
1998).

W. H. Press, S. Teukolsky, W. Vetterling, B. Flannery, *Numeric
Recipes in C* (Cambridge Univ. Press, 1992).

S. Toxvaerd, *Molec. Phys.* **72** (1991) 159.

M. Andrecut, *Mod. Phys. Lett. B* **12** (1998) 393.

T. Odagaki, Y. Hiwatari, *Phys. Rev. A* **41** (1990) 929.

STUDIA UNIVERSITATIS BABEŞ-BOLYAI, PHYSICA, XLIV, 1, 1999

ASPECTS CONCERNING THE DEPENDENCE OF ALTERNATIVE COMPONENTS OF THE VOLTAGE DUE TO THE LATHING PROCESS, ON THE LATHING PARAMETRES.

T. R. REDAC*

ABSTRACT. The paper deals with analysing the behaviour of the alternative com-pounds of voltage, which appear during the lathing process, depending on the pro-cess parameters and the type of material.

Introduction

The voltage appearing between the part to be lathed and the cutting tool was studied in order to be taken a reference parametre in the adaptive command of machine tools.

Depending on the lathing temperature, the voltage was defined as the thermoelectromotive voltage. In this respect, the continous constituent of the voltage was sufficiently studied in detail.

This paper is meant to bean approach to describe the alternative components of voltage, when three kinds of materials have been lathed (OLC15;OLC45;40C10 steel)

Measurements and results.

The experimentals were performed on a SN710 lathe and using as lathing matherial the OLC15;OLC45 and 40C10 steel. The cutting tool was electrically isola-ted from the tool-bearer using an isolated platte and plastic, as show in fig. 1

* Technical University Arad, Romania

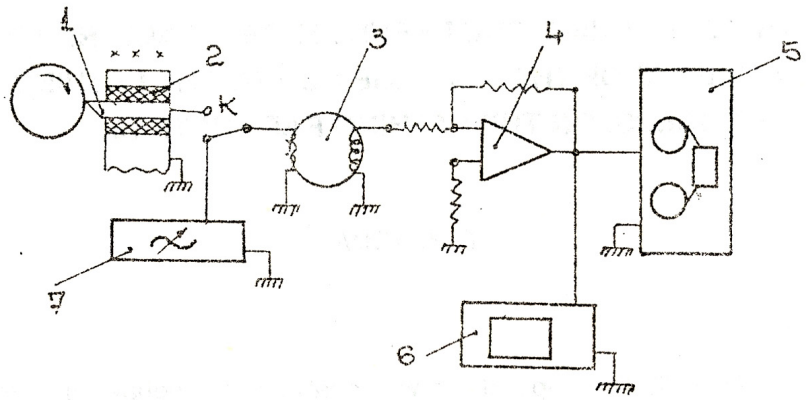

Fig. 1. The scheme of isolating the cutting tool

The electric signal was taken from between the cutting-tool and the lathe body. The connecting wires supplied a transformer 3 made on a ferreites core of high permeability. The latter is to separate the continuous constituent of the voltage. The signal was amplified using the amplifier tape an recorded 5 and visualised on an osciloscope 6. A generator 7 allowed us to compare (during the measurement) the signal to be measured to a standard signal, both of them being recorded by the tape recorder 5.

The signal previously recorded was spectrale analysed using an equipment made by Bruel & Kjaer. The measurements were performed using a spectrum analyser with an octave wide band, the central frequencies ranging to 215 and 1000Hz, respectively.

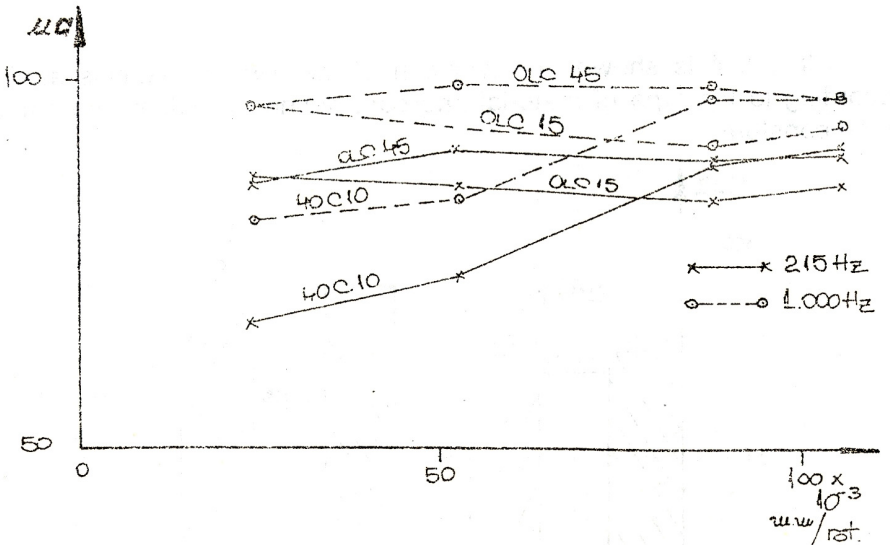

Fig. 2. The evolution of the voltage having 215 and 1000Hz frequencies, depending on the lathing advance.

In fig. 2 are shown the evolution of voltage values for 215 Hz and 1000Hz, respectively, depending on the lathing advance and fig. 3 shows the same evolution depending on the lathing depth.

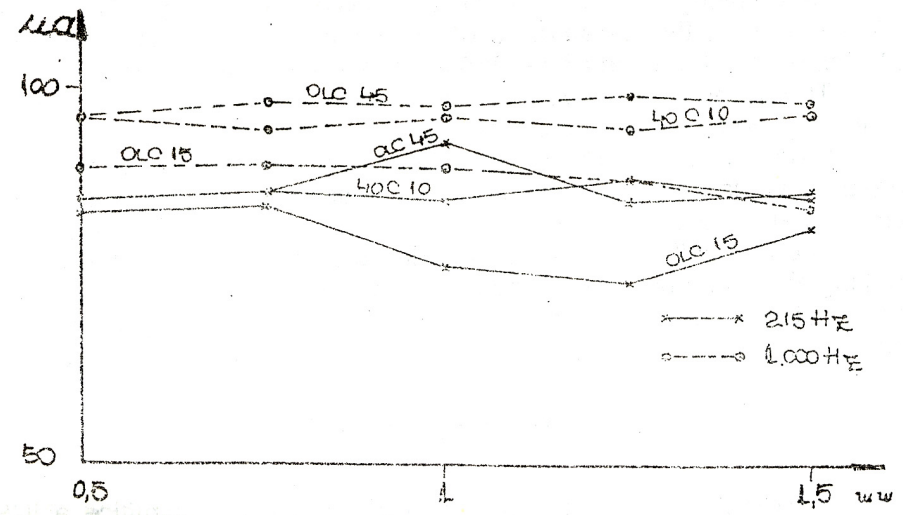

Fig. 3. The dependence of voltage on the lathing depth

In fig. 4 is shown the evolution of the two frequencies analized according to the type of material and considering the lathing parameters being constant.

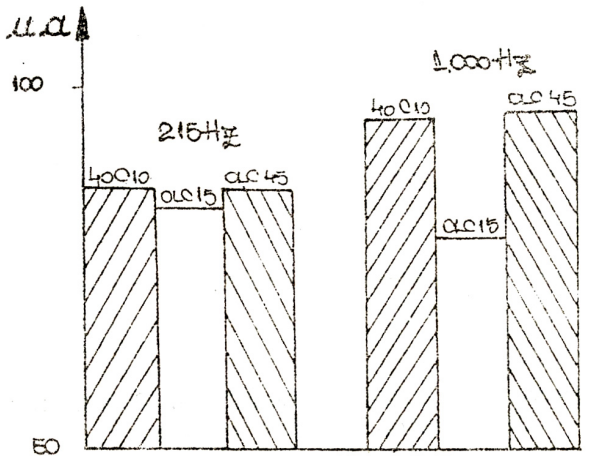

Fig. 4. The dependence of voltage on the type of material

Conclusions

As resulting from the graphic proccesing of the signal, the voltage is dependent on the parameters of the lathing process and the kind of material, both in the case of the 215 Hz and 1000 Hz frequency.

The measured values increase as the advance does for both frequencies and they remain almost constant when the chip width alters.

Whether at a 215 Hz frequency the differencies between the measured values are relatively shall but noticeable, the same differencie increases at 1000Hz.

These results may lead to the idea that this voltage is the result of breaking the ma-terial /metal crystals and not fluctuation of the thermo-electromotive voltage between the part and the cutting-tool, especially as in the spectrum we could also identify frequencies higher than 1000 Hz.

REFERENCES

1. T. R. Redac, C. Belei - Sesiunea de comunicări ştiinţifice a ICSIT "TITAN" Bucureşti - oct. 1986.
2. V. Dițu - Buletinul Ştiinţific al IP Iaşi Tom XLIV (XLVIII) supliment I 1998, p. 283.

STUDIA UNIVERSITATIS BABEŞ-BOLYAI, PHYSICA, XLIV, 1, 1999

THERMAL FLUCTUATIONS OF DOMAIN INTERFACES IN THE 2D KINETIC ISING MODEL

Z. NÉDA[*], Y. BRECHET[**]

ABSTRACT. The diffusive motion of the center of mass for an initially straight domain interface is studied in the framework of the 2D kinetic Ising model. As a function of the length of the interface and temperature the diffusion constant is computed. Simulation results are compared with simple theoretical considerations.

PACS numbers: 75.10.H, 82.65.D, 02.50.N

Keywords: Ising model, Glauber dynamics, interface, random-walk, diffusion constant, Monte-Carlo method

Introduction

Interfaces in 2D and 3D Ising systems were considered by several authors, thus many aspects of the problem are clarified. Static properties are usually well understood. The spatial fluctuations of the interface at low temperatures are described by capillary-wave theory [1]. The magnetization profile for a 2D Ising strip in the direction perpendicular to the interface was determined by the transfer-matrix method [2]. The surface tension which is of great importance in understanding interface profiles and dynamics was studied both analytically [3] and by MC simulations [4]. The roughness of the interface and connections to the well-known solid-on-solid models, were discussed in [5], and their instantaneous shape from the viewpoint of fractal geometry was studied in [6].

[*] Babes-Bolyai University, Department of Physics, str. Kogalniceanu, nr.1, RO-3400, Cluj-Napoca, Romania

[**] Laboratoire de Thermodynamique et Physico-Chimie Metallurgique, ENSEEG/INPG Domaine Universitaire de Grenoble-B.P. 75, 38402 Saint Martin d'Heres Cedex, France

Kinetic aspects were also investigated. Starting from an initially sharp interface, the increase of its width up to the time-independent value was considered theoretically in [7], and studied by MC simulations in [8]. In the presence of a nonzero magnetic field the width of the moving Ising interface was studied by MC methods [9]. Phenomenological dynamics of Ising interfaces were derived in [10], and dynamics of field-driven and tilted Ising interfaces were considered in [11]. In the framework of Glauber dynamics [12], the kinetics of an initially circular and strip-shaped domain was investigated in [13] and [14] respectively. These two studies revealed the importance of understanding the diffusive motion of interfaces and their roughening due to thermal fluctuations.

Our present paper intends to contribute in this sense by investigating the diffusive motion of an initially flat interface in the 2D Ising model driven by Glauber dynamics (kinetic Ising model).

The questions we want to address more specifically are: the temperature dependence of the characteristic mobility; the finite size scaling effects for the problem; the influence of boundary conditions; and the microscopic mechanisms governing this motion.

We will address these problems from two aspects: MC computer simulations and simple analytical approach relying on the identification of elementary mechanisms.

The computer simulation method

The 2D kinetic Ising model with nearest neighbor interactions was considered on square lattices with sizes $N_x \times N_y$, N_x and N_y chosen sufficiently large $N_y=100$ and $N_x>50$, so that the critical temperature, T_c, of the system is well approximated by the $T_c = 2J/(k\ ln(1+2^{1/2})) \cong 2.2692\ J/k$ relation. The initial state of the system was such as that all the spins with the y coordinate between 0 and $N_y/2$ were set to $+1$ whereas the spins with the y coordinate between $N_y/2$ and N_y are set to -1, thus a sharp straight interface is positioned at $y=N_y/2$. We considered both free boundary conditions and periodic conditions in the x direction together with anti-periodic conditions in the y direction. By definition the time unit is *1 MC* step, which is equivalent with $N_x \times N_y$ trials of randomly chosen spin flips. The interface was detected by a special subroutine at equally distant time moments (usually *10* time units).

The interface is defined as follows: the spins forming the interface must be connected by nearest neighbors to a chain of alike spins percolating through the system in the x direction and moreover each of them must have at least one unlike nearest-neighbor. Computing the center of mass (CM) of the interface, y_l, we followed it's time evolution $y_l(t)$ during $t_{max}=200$ *MC* step time interval. We considered usually *5000* different runs

(each of them from the same initial condition and for the same time interval), and we calculated the quantity

$$<(y_l(t)-N_y/2)^2>, \qquad (1)$$

where the averaging is performed on the different realizations. For a diffusive motion one might expect

$$<(y_l(t)-N_y/2)^{1/2}>=2\,d\,D\,t, \qquad (2)$$

with d=1 (the dimensionality of the walk) and D the characteristic diffusion coefficient. When the dynamics was proven to be diffusive, the time and size dependence of the diffusion coefficient was systematically investigated.

Simulation results

On Fig.1 we plotted the results of our computer simulations for the quantity $<(y_l(t)-N_y/2)^2>$ versus the time, considering N_x=100, free boundary conditions and several values of the $T_r=T/T_c$ reduced temperature. The results drawn on the upper graph are for T_r<0.2, and the ones below for $T_r \geq 0.3$. One can observe here that for very low temperatures the linear regime (2), is not yet reached and thus the motion of the CM is not a diffusive one. For reduced temperatures larger than T_r=0.3 the motion of the center of mass is very accurately diffusive.

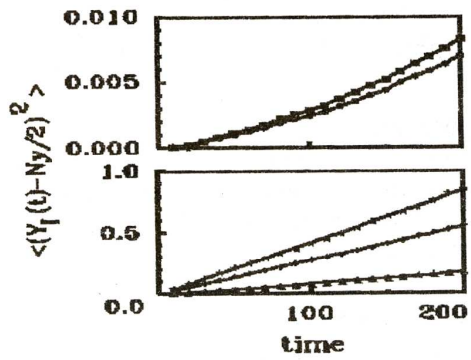
0.010
0.005
0.000
1.0
0.5
0.0
100
200
time
<(Y_l(t)-Ny/2)^2>

Fig. 1. Variation of the mean square displacement versus time for N_x=100, T_r=0. 1 (dots), T_r=0. 15 (squares), T_r=0. 3 (triangles), T_r=0. 45 (romboid), T_r=0. 5 (stars)

When the movement of the CM was proved to be diffusive, we studied the dependence of the diffusion coefficient (2) as a function of N_x and T_r. On Fig.2, considering T_r=0.4 and free boundary conditions the results concerning the N_x dependence are shown. The data indicate clearly that the diffusion coefficient is inversely proportional to the size of the system in the *x* direction. Similar results hold for higher temperatures.

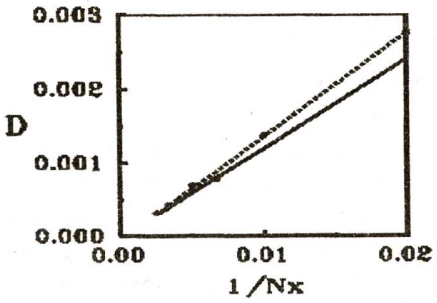

Fig. 2. Variation of the diffusive coefficient, D, as a function of the inverse of the lattice size in the direction of the interface, $1/N_x$, for T_r=0. 4. The dashed curve is the best-fit plot, and the continuous curve is our prediction (20) (free boundary conditions)

The temperature dependence of *D* was studied for N_x=100 considering both free and periodic-type boundary conditions. Fig.3 shows that for this interface the influence of boundary conditions is neglectable in the $0.3T_c<T<0.7T_c$ temperature interval. In the neighbourhood of T_c the diffusion coefficient increases rapidly.

Theoretical approach

In order to understand these macroscopic results, we need first to identify the microscopic mechanisms responsible for the motion of the interface. From simulation we have learned that at relatively small temperatures and long interfaces there are no important differences between free and periodic boundary conditions. This is why here we will consider the more simple free boundary case.

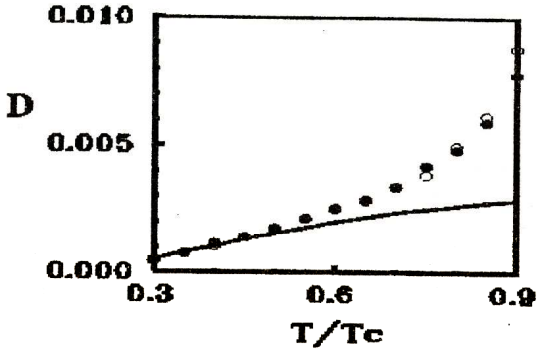

Fig. 3. Results for the diffusion coefficient, D, versus the reduced temperature, T/T_c, for N_x=100. The empty circles are for periodic and the filled ones for free boundary conditions (they overlap at low temperatures).
The continuous curve show our theoretical prediction (20) for low temperatures.

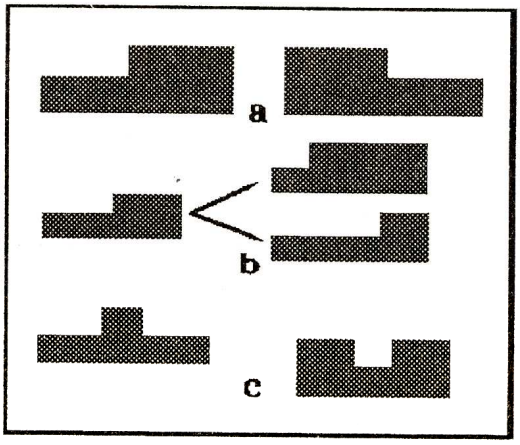

Fig. 4. The important mechanism of moving the CM of the interface at low temperatures. Fig. 4a and Fig. 4b presents the steps and their possible evolutions, respectively. Fig. 4c presents the kinks

Let us consider a lattice of sizes N_x N_y at temperature T, and create the straight line interface at $y=N_y/2$.

At zero thermodynamic temperature the interface would remain a straight line, but for $0<T<T_c$ temperatures a number n of *steps* (Fig.4a) will appear. The presence of a step will increase the energy of the system by:

$$\Delta E_1=2J \qquad (3)$$

Considering the system in canonical ensemble at temperature T, the average number of steps, $<n>$, present on the interface will be given by:

$$<n>(N_x,T)=\sum_{n=0}^{Nx-1} nC^n_{Nx}2^n e^{-2Jn/kT} / \sum_{n=0}^{Nx-1} C^n_{Nx} 2^n e^{-2Jn/kT} \qquad (4)$$

The factor 2^n in the above formula appears due to the two possible orientations of the steps (Fig.4a). By extending the sums in (4) up to N_x (approximation acceptable in the large N_x limit due to the exponential terms which decay rapidly) by elementary combinatorics one can show that:

$$<n>=N_x [2e^{-2J/kT}]/[1+ 2e^{-2J/kT}] \qquad (5)$$

The total average length of the interface will be

$$<L>=N_x+ <n>=N_x(1+\{[2e^{-2J/kT}]/[1+2e^{-2J/kT}]\}) \qquad (6)$$

During the time evolution of the system the easiest way (with no energy cost) of moving the CM in the y direction is by shifting the position of the steps in the x spatial direction (Fig.4b). By adding (or subtracting) a site at a step we move in fact the CM in the y direction with the quantity:

$$a_1= 1/<L> \qquad (7)$$

The diffusion coefficient D_1 characteristic for this mechanism is

$$D_1=f_1 a_1^2 \qquad (8)$$

where f_1 is the frequency of these jumps in one direction of the y axis, which is equal to the product of the number of sites where these jumps can occur (i.e. the average number of steps) by the frequency of jumps in one direction during a unit time interval (1/2). Thus f_1 is given by:

$$f_1=<n>/2 \qquad (9)$$

One might expect that at very low temperatures this effect would be the dominant one for the motion of the CM, and would lead to a simple random walk in the y direction. A second contribution which could be important at low temperatures comes from the formation of *kinks* (Fig.4c) with an energy cost of:

$$\Delta E_2=4J \qquad (10)$$

The kinks can appear with equal probabilities on both side of the interface, on (N_x -<n>) sites, leading also to a random walk of the CM. The characteristic diffusion coefficient associated to this mechanism is

$$D_2=f_2a_2^2 \,, \qquad (11)$$

with:

$$f_2=(N_x-<n>)[e^{-4J/kT}]/[1+e^{-4J/kT}] \qquad (12)$$

Depending on which side of the interface is detected we have

$$a_2=3/<L> \;\; or \;\; a_2=1/<L> \,, \qquad (13)$$

which leads on average to:

$$<a_2^2>=5/<L>^2 \qquad (14)$$

For temperatures closer to T_c many other mechanisms of moving the CM in the y direction become possible, but for relatively small temperatures the above two contributions are dominant. As both of this two mechanisms occur in parallel the total diffusion coefficient in the low temperature regime is given by:

$$D = D_1 + D_2 \qquad (15)$$

We mention here, that for very low temperatures where the first mechanism is the leading one, in order to reach the linear regime (2) one might require

$$t_{max}\, f_1 \geq (\approx 100) \qquad (16)$$

to have at least 100 random steps in one direction. Although the above condition is a very phenomenological one, we can derive a condition on temperature in order to reach this linear regime. For N_x=100 and t_{max}=200 we get

$$T_r > 0.17, \qquad (17)$$

which is in reasonable agreement with our computer simulations.
The N_x dependence follows directly from the model

$$D \sim 1/N_x \qquad (18)$$

in agreement with the results shown in Fig.2.

The low temperature dependence of the diffusion coefficient can also be derived from this model with no adjustable parameter. It is shown on Fig.3 that the agreement between numerical results and theoretical calculations is very good for reduced temperatures between 0.3 and 0.5.

For higher temperatures many other mechanisms occurs leading to an acceleration of the diffusion.

Conclusions

Studying the diffusive motion of the CM for a domain interface in the 2D ferromagnetic kinetic Ising model we obtained the following results:

- The linear regime is reached if condition:

$$t_{max}>100(1+e^{-2J/kT})/N_x e^{-2J/kT} \qquad (19)$$

is satisfied.

- For temperatures not too close to T_c $(0.3T_c<T<0.5T_c)$ the diffusion coefficient characteristic for the random walk can be reasonably well approximated, (15), by

$$D=p(1+2p)[1+5p/(1+p^2)]/N_x(1+4p^2) \qquad (20)$$

with $p=e^{-2J/kT}$.

- In the neighborhood of T_c the diffusion coefficient increases strongly due to many other mechanisms which can modify the shape of the interface.

The p/N_x dependence (20) of the diffusion coefficient makes this movement neglectable for large interfaces and low temperatures. The knowledge of the diffusion coefficient (20) is important also for describing the movement of the interface in magnetic fields.

REFERENCES

1. F.P. Buff, R.A. Lovett and F.H. Stillinger, *Phys. Rev. Lett* **15** (1965) 621.
2. J. Stecki, A. Maciolek and K. Olaussen, *Phys. Rev. B* **49** (1994) 1092.
3. K. Binder, *in Phase Transition and Critical Phenomena* edited by C. Domb and J.L. Lebowitz (Academic, New York 1983) Vol. 10; P. Kleban, *Phys. Rev. Lett.* **67** (1991) 2799; D.B. Abraham and N.M. Svrakic, *J. Stat.Phys.* **63** (1991) 1077; N.M. Svrakic, V. Privman and D.B. Abraham, *J. Stat. Phys.* **53** (1988) 1041; H.L. Richards, M.A. Novotny and P.A. Rikvold, *Phys. Rev. B* **48** (1993) 14584.

4. U. Hansmann, B.A. Berg and T. Neuhaus, *Int. J. Mod. Phys. C* **3**(1992)1155; B.A. Berg, U. Hansmann and T. Neuhaus, *Z. Phys. B* **90** (1993) 229.
5. K.K. Mon, D.P. Landau and D. Stauffer, *Phys. Rev. B* **42** (1990) 545.
6. Z. Neda and G. Lipi*, J. Magn. Magn. Mat.* **125** (1993) L263.
7. R. Lipowsky, *J. Phys. A* **18** (1985) L585.
8. D. Stauffer and D.P. Landau, *Phys. Rev. B* **39** (1989) 9650.
9. P. Devillard, J. Stat. Phys. **62** (1991) 443.
10. H. Spohn, J. Stat. Phys. **71** (1993) 1081.
11. M. Barma, *J. Phys. A* **25** (1992) L693.
12. R.J. Glauber, *J. Math. Phys.* **4** (1963) 294.
13. P.S. Sahni, G.S. Grest and S.A. Safran, *Phys. Rev. Lett.* **50** (1983) 60.
14. S.A. Safran, P.S. Sahni and G.S. Grest, *Phys. Rev. B* **26** (1982) 466.